4-27-2019

Spatial Control of Gold-Silica-Quantum Dot Nanostructures and Single Particle Optical Study of Plasmon-Exciton Strong Coupling Effect

Yi Luo
University of Connecticut - Storrs, yi.2.luo@uconn.edu

Spatial Control of Gold-Silica-Quantum Dot Nanostructures and Single Particle Optical Study of Plasmon-Exciton Strong Coupling Effect

Yi Luo, Ph.D.

University of Connecticut, 2019

Metallic nanoparticles can generate collective oscillation of conduction electrons when excited by incident light. This unique light-matter interaction is termed as localized surface plasmon resonance (LSPR) and offers the possibility of manipulating light well below the diffraction limit. This extreme concentration of light also greatly influences the absorption and decay processes of the nearby Quantum Dots (QD). When plasmon-exciton interaction enters strong coupling regime, the energy coherently oscillates between the QD and the plasmonic cavity. Optical studies at the single particle level of hybrid Au-QD structures with strong-coupling can help us understand the origin of this phenomena as well as open up the possibility of designing new optoelectronic devices. The ultimate goal of this thesis is to colloidally assemble the Au-QD structure with controlled coupling strength. Along the journey, we firstly studied how to synthesize the Au nanoparticle with desired plasmonic properties. Next, we developed a method to create Au-silica nanostructures of varying morphology and studied the mechanism how these morphologies were formed. The Au-silica nanostructures then served as building blocks for QDs to attach on. The strong plasmon-exciton coupling was finally achieved with an Au-QD-Au sandwich structure. In this structure, the plasmon-exciton coupling strength was controlled by the size of QDs, which determines the size of the gap in the Au dimer. Our results offer guidance of synthesizing hybrid materials and shed light on the design principle of new optoelectronic devices.

Spatial Control of Gold-Silica-Quantum Dot Nanostructures and Single Particle Optical Study of Plasmon-Exciton Strong Coupling Effect

Yi Luo

B.S., University of Science and Technology of China, 2013

A Dissertation

Submitted in Partial Fulfillment of the

Requirements for the Degree of

Doctor of Philosophy

at the

University of Connecticut

2019

APPROVAL PAGE

Doctor of Philosophy Dissertation

Spatial Control of Gold-Silica-Quantum Dot Nanostructures and Single Particle Optical Study of Plasmon-Exciton Strong Coupling Effect

Presented by
Yi Luo, B.S.

Major Advisor

_____

Dr. Jing Zhao

Associate Advisor

_____

Dr. Jie He

Associate Advisor

_____

Dr. Xudong Yao

University of Connecticut

2019

Dedicated To

My parents, Yongbin Luo and Xiangqin Shen
My sister, Yanze Luo

Acknowledgements

The past 6 yeas have been an extremely challenging but also rewarding journey. I wouldn't have been able to complete this challenge without the help and support from many people. First of all, I want to thank my advisor Dr. Jing Zhao, who has shown the greatest patience and care to me whenever I needed her. She's the one who told me it's OK when my experiments seemed not to work and always had time for a discussion. She guided me through the tough moments in research and also generously shared with me her life experiences. Thank you, Dr. Zhao, for never giving up on me and always showing your biggest support. I also want to convey my gratitude to my committee members: Dr. Jie He, Dr. Xudong Yao, Dr. Tomoyasu Mani and Dr. Rebecca Quardokus for their priceless input and suggestions for my research. My special thanks go to the two postdocs who taught me synthesis and more importantly, how to do be an independent researcher. Xiangdong Tian, the first postdoc joined the group, is an extremely hard-working person. I always saw him reading papers while waiting for centrifugation to complete. He's the person who taught me hard work would always pay off. The second postdoc, Shutang Chen, always encouraged me to never give up on my research. I want to express my sincerest thanks to him for his suggests on both research and life. I also want to convey my thanks to the former and current lab members, Julie Jenkins, Swayandipta Dey, Sravan Thota, Terianna Wax, Xudong Wang, Yonglei Sun, Yongchen Wang and Ann Mureithi for their help with my research, life and general exam.

A special thanks to all my friends at UConn, specially Zhu Luo, Ran Miao, Chengsheng Chen, Yikun Huang, Weiyu Zhang, Lei Jin and Lang group, the list can go on and on, for all the hot pots and milk teas we had together.

I want to thank my family for their unconditional love and support: my Dad Yongbin Luo, Mom Xiangqin Shen and little sister Yanze Luo. Thank you, Mom and Dad, for supporting me to follow my dream to become a chemistry researcher. Thank you for never complaining about me leaving home to live at the other side of the earth. Thank you for telling me that you care more about my happiness than my achievement. Thank you Yanze for being my little sister. You are the smartest and the most loving little girl I've ever met in my life. Thank you for accompanying mom and dad during all the years that I'm away from home. I'm very proud of you.

Table of Contents

List of Figures

List of Schemes

Chapter One : Introduction

1.1 **Localized Surface Plasmon Resonance**

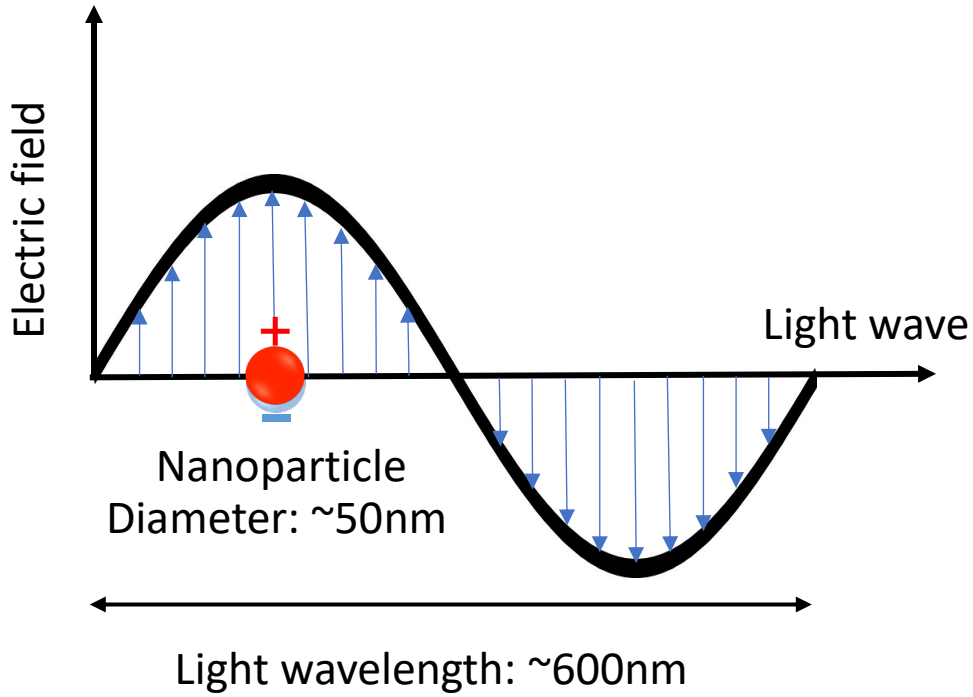

Scheme 1.1. Schematic illustration of Localized Surface Plasmon Resonance in a metal nanoparticle

Nobel metal nanoparticles, specifically gold and silver, has a plasmon resonance frequency that magically matches the frequency of the visible light, enabling collective oscillation of the conduction electrons with the incident light of matching frequency. This oscillation happens as the electric field of light caused displacement of conduction electrons with respect to the positive ionic

lattice background, creating electrostatic force as the restoring force and generate oscillation of the electrons. (Scheme 1.1) This unique light-matter interaction is termed as Localized Surface Plasmon resonance (LSPR). LSPR enables tight confinement of the energy of photons within a few nanometers above the nanoparticle surface. As the energy of the photon is stored as coherent oscillation of the conduction electrons, thus the form of energy is converted from constant exchange between electric and magnetic field to that between kinetic and potential energy of oscillating electrons. LSPR enables metal nanoparticles to be strong light absorbers and scatters, giving metal nanoparticles bright, distinct colors.

Mie first solved equation of extinction cross-section by the treating the spherical nanoparticle as a dipole.[1] Nanoparticles with diameter below 20 nm can have the extinction cross section expressed as below:

$$\sigma_{ext} = \frac{18\pi\varepsilon_m^{3/2}V}{\lambda}\frac{\varepsilon_2(\lambda)}{[\varepsilon_1(\lambda)+2\varepsilon_m]^2+\varepsilon_2(\lambda)^2}$$

Equation 1.1

Here ε_m is the dielectric constant of the medium, ε_1 and ε_2 are the real and imaginary part of the dielectric function of the metal. To get the maximum value of σ_{ext}, ε_1 should be equal to -$2\varepsilon_m$, which, leads to the solution of the plasmon resonance frequency. However, since the average travel distance of electrons in metal is about 40 nm.[2] When the nanoparticles are below 20 nm the electron-surface scattering becomes significant and the dielectric function needs to be modified to be size dependent. As the size of the nanoparticle becomes bigger, multipole mode oscillation come into play and the extinction peak changes with size. These two factors account for the size dependence of LSPR in spherical nanoparticles but it would be a different case for anisotropic nanoparticles.[3] The gold nanorod has two distinct peaks from the oscillations along the two axes.

The resonance at the shorter axis is defined at the transverse mode and the one from the longer axis is defined at the longitudinal mode. These two modes can be solved with Gans Theory, which yields the longitudinal mode much red-shifted than the transverse mode.[4]

With the advancement of colloidal and lithography method, nanoparticles with various shapes can be easily achieved.[5, 6] With Au nanoparticle as an example, people can tune plasmon peak from 500 nm to even above 1000 nm simply by tuning the morphology.[7] However, even with the desired wavelength easily achieved, the intrinsic loss in metallic nanoparticles at optical frequency is largely limiting the application of LSPR. Therefore, it is of essential importance to evaluate the dephasing process of LSPR and how can it be changed by tuning the composition, morphology or higher-ordered structures.

While the peak wavelength is mostly determined by the real part of the dielectric function of the metal nanoparticle and the dielectric constant of the local medium, the loss is dependent on the imaginary part with the decay rate $\gamma \propto \varepsilon_2(\omega)$. After the LSPR is excited by light, the energy is decayed either radiatively or non-radiatively. In a 20 nm particle, due to the large non-radiative loss, the percentage of radiative decay is only 1.5%.[8] The large part of LSPR is converted to inter-band or intra-band transition to generate electron-hole pairs. Then due to electron-phonon scattering, the energy is transferred to the lattice and finally disappeared as heat. Silver has a much smaller imaginary part compared with gold and is known as a better plasmonic material. Due to the large non-radiative loss plasmonic nanostructures are not efficient in enhancing fluoresce process. The plasmon is well known for being capable to enhance the absorption process, and then due to the Purcell effect, the energy of the exciton is transferred to plasmon and is then most probably dissipated into heat. That's why plasmon is only able to efficiently enhance very weak processes with low quantum efficiency such as Raman scattering.

1.2 **Plasmon-Exciton coupling**

1.2.1 Introduction

Localized surface plasmons and excitons are two physical states of nanoscale metal and quantum emitter (QE) systems, which govern their optical properties. Specifically, localized surface plasmons are collective oscillations of electrons of metal nanoparticles, which can be tuned by their size, geometry, and composition. While an exciton is a bound electron-hole pair in an inorganic or molecular semiconductor. Its generation and relaxation determine the light emitting property of the semiconductors. Their emitting wavelength, quantum yield and lifetime vary with their size, material and also surface states. When nanoscale metal and semiconductors are conjugated together, the highly tunable plasmon-exciton coupling effect can modulate the light-matter interaction in hybrid plasmonic-excitonic systems, enabling implementation of desired functionality at nanoscale. Various applications based on the hybrid plasmon-exciton system have been developed, ranging from bio-imaging, sensing, non-linear optics to nano-lasing.[9-16] However, the design principle for different applications vary greatly as they may reside in different plasmon-exciton coupling regimes.[17]

Single atoms, fluorescent molecules and quantum dots are known to be quantum emitters (radiative quantum systems), which could emit single photons under the right excitation conditions. When QEs are in close vicinity to plasmonic nanoparticles, both their absorption and emission rates are greatly enhanced.[18, 19] This enhancement is due to the unique localized surface plasmon resonance confined on the surface of metallic nanostructures, which offers nanoscale manipulation of light well below the diffraction limit.[20, 21] Upon light excitation, the energy of the photons is converted to the kinetic energy of the conduction electrons of metal nanoparticles in the form of coherent oscillations. And thus the displacement of conduction electrons with respect to

the positive lattice background creates a strong electrical local field within a few nanometers of the surface, which is also known as a plasmonic nanocavity.[22] This extreme light concentration on the metal nanoparticle surface increases the absorption rate of the nearby QEs.[23] In the weak coupling regime, the plasmon resonance also increases the density of states, which results in a faster emission rate of excitons due to Purcell effect.[24, 25] With the presence of plasmonic nanoparticles, the exciton can recombine and decay into plasmon resonance instead of simply radiate into the far field. However, since the plasmonic metal nanoparticle is very lossy, the energy from the exciton is most likely converted to heat, adding an additional non-radiative channel. Therefore, the plasmon induced fluorescence enhancement/quenching of the QE is a joint effect of the three processes.

When plasmon-exciton coupling enters strong coupling regime, the energy exchange rate between these two exceeds that of any other decay processes in the system. In this strong coupling regime, plasmon and exciton are no more distinct individuals but a hybrid plexciton state, which is half plasmon, half exciton. In this new plexciton system, two new normal modes are generated, which is also known as Rabi-splitting or anti-crossing. This phenomenon leads to peak splitting in both the single particle dark-field scattering and the fluorescence spectra. A strongly coupled plexciton state holds promise for realizing Bose-Einstein condensation, thresholdless polariton lasing, solar cells and single photon non-linear optics.[26-31]

With the recent advancement in Nano synthesis and fabrication techniques, various hybrid plasmonic-excitonic structures have been achieved. Constructing the hybrid structures can be realized by simply drop-casting the QEs onto the substrates with plasmonic nanoparticles,[32] utilizing AFM tip to place the plasmonic nanostructure close to the QEs,[33] using optical tweezers,[34] or linking them with linkers in colloidal solutions[35]. Among these methods, colloidal methods are

the most powerful ones because of their capability to construct 3-D geometry with precise control and to produce the structures in large scale. For instance, with DNA, polymers or small molecules as linkers, colloidal methods have achieved nanometer precision in distance control between the plasmonic nanoparticles and the QEs in addition to processing the assembly procedure in large scale.[36, 37] In this Review, we focus on the advancements in hybrid plasmon-exciton structures produced with colloidal methods. We first look into the theoretical work which serves as the guideline to design plasmon-exciton structures. Then we discuss the optical properties of plasmon-exciton structures that have been synthesized/assembled through colloidal methods, to summarize the progress made in terms of either fundamental studies or real applications with these structures. Lastly, we comment on the progress and limitation of current work and suggest possible future directions.

1.2.2 Defining the Plasmon-Exciton Coupling Regimes

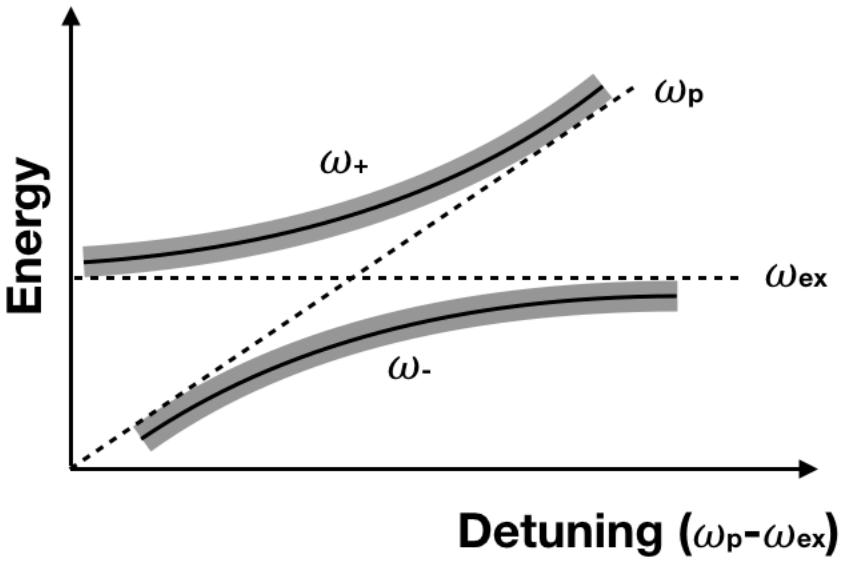

Figure 1.1 Anti-crossing behavior: dashed lines show that the exciton and plasmon frequencies remain undisterbed in the weak coupling regime and the solid lines show anti-crossing behavior at the cross point in the strong coupling regime.

Plasmon-exciton coupling arises from the energy exchange between QEs and plasmonic nanoparticles. In the quantum mechanical approach, the coupled system is diagonalized by a Hamiltonian yielding a solution of two eigenstates. If we only consider the resonant case (plasmon frequency ω_p equals exciton frequency ω_{ex}), the energies are[38]:

$$E_{\pm} = \omega_p - \frac{i}{2}(\gamma_{QE} + \gamma_{cav}) \pm \sqrt{g^2 - \frac{1}{4}(\gamma_{QE} - \gamma_{cav})^2}$$

Equation 1.2

Where γ_{QE} and γ_{cav} are the decay rates of the QE and cavity respectively, and g is the coupling strength.

The splitting term $\Omega = \sqrt{4g^2 - (\gamma_{QE} - \gamma_{cav})^2}$ only has valid solutions when the following criteria is reached[39]:

$$g > \frac{1}{2}|\gamma_{QE} - \gamma_{cav}|$$

Equation 1.3

This condition is defined as the strong coupling regime, which leads to Rabi-splitting.

As illustrated in Figure 1.1, we fix the exciton frequency (ω_{ex}) but tune the plasmon resonance frequency(ω_p), the two constituents would preserve their entity in the weak coupling regime (dashed lines). As the system enters strong coupling regime, the plasmon and exciton hybridize to form a plexitonic state, leading to avoided crossing at the cross point, which is also known as anti-crossing behavior (solid lines, the grey shadow represents damping). The strong coupling effect generates two new modes denoted as upper plexcitonic mode ω_+ and lower plexcitonic mode ω_-, as shown in Figure 1.1. However, the splitting of the two modes can only be spectrally resolved when the energy difference exceeds the two half peak widths at half maximum of the two plexciton branches added together (the damping of the two new modes do not overlap):

$\Omega > \gamma_{QE} + \gamma_{cav}$

Equation 1.4

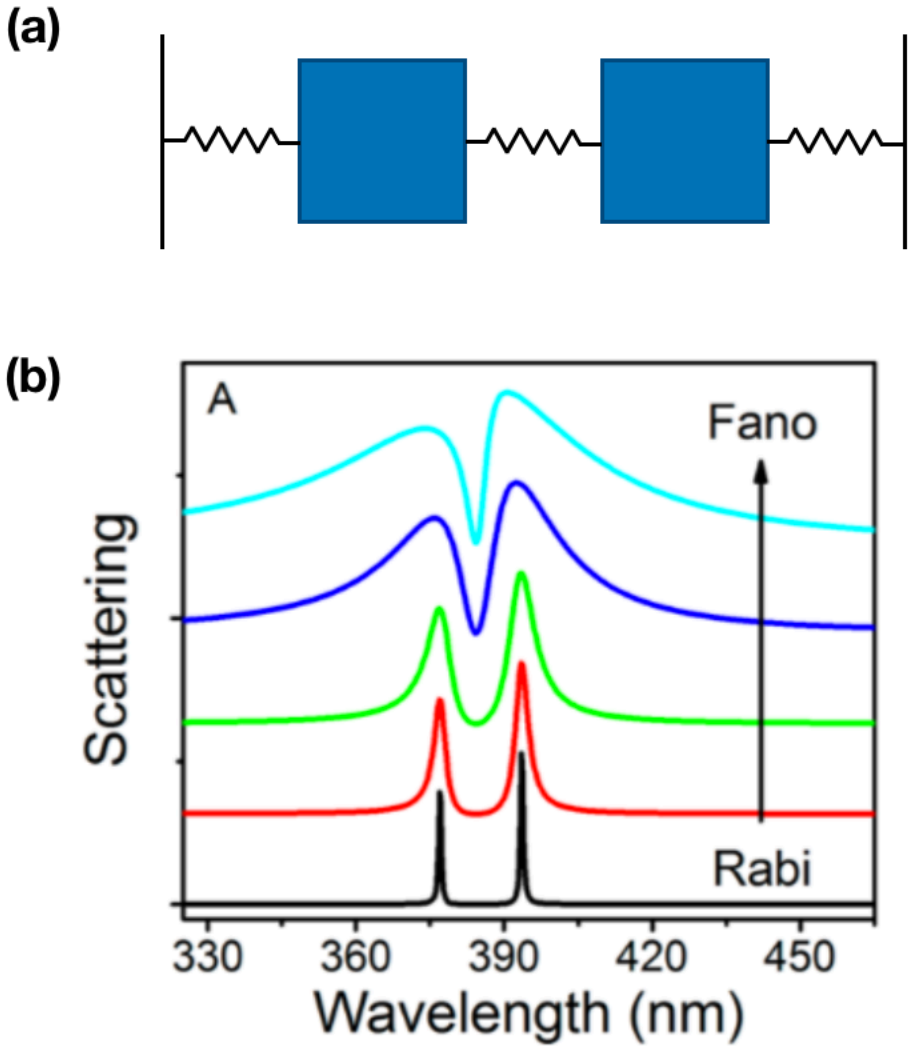

Figure 1.2 (a) A schematic illustration of two coupled oscillators. (b) Transition of spectral line shape from Rabi splitting to Fano resonance as the Plasmon damping increases. Reproduced with permission from Ref. [42], © 2014, American Chemical Society.

When both criteria (Equation 1.3 and Equation 1.4) are reached, the plasmon-exciton strong coupling can be spectrally observed with peak splitting in the single particle dark field scattering and the fluorescence spectra of individual hybrid QE-plasmonic nanoparticle structures (Figure 1.2, black, red and green spectra). Another phenomenon, Fano dip that happens in the intermediate coupling regime, can easily be mixed up with Rabi-splitting as their spectral line shapes are very similar (Figure 1.2, blue and cyan spectra). However, these two are caused by two different physical processes as the Fano dip is a result of constructive and destructive interference in the far-field.[40, 41] Therefore, observation of peak splitting solely in the dark-field scattering spectrum does not guarantee strong coupling. In the classical approach, plasmon-exciton coupling is treated as two oscillators coupled together (Figure 1.2a). The transition from Rabi to Fano can be achieved by increasing the plasmon damping term when solving for scattering cross-section of the hybrid structure.[42, 43] As discussed in Faucheaux's work[42], when the plasmon damping rate is slow, the scattering cross section takes the form of:

$$C_{sca} = \frac{k^4}{6\pi} \cdot \frac{((\omega_0^2-\omega^2)(1+F)+2F\kappa)^2}{((\omega_0^2-\omega^2)^2-\kappa^2F)^2}$$

Equation 1.5

Where k is the wave-vector, ω_0 is the frequency of both plasmon and exciton oscillators when they are in resonance, and F is the magnitude of the plasmon oscillator strength.

In this case, the expression yields two maxima representing two resonant modes:

$$\omega = \sqrt{\omega_0^2 \pm \kappa\sqrt{F}}$$

Equation 1.6

When the damping rate (Γ) is large and non-negligible, the cross section takes the form of:

$$C_{sca} = \frac{k^4}{6\pi} \cdot \left(\frac{1}{(\omega_0^2 - \omega^2)^2 + (\frac{\kappa^2 F}{\omega\Gamma})^2} + (\frac{1+F}{\omega\Gamma})^2 \frac{(\omega_0^2 - \omega^2 + (\frac{2F}{1+F})\kappa)^2}{(\omega_0^2 - \omega^2)^2 + (\frac{\kappa^2 F}{\omega\Gamma})^2}\right)$$

Equation 1.7

The first term (blue) represents the solution of a Lorentzian peak at the frequency of ω_0. The second term (red) induces Fano interference by creating a dip or asymmetrical line shape in the scattering spectrum. Therefore, in the intermediate coupling regime where plasmon damping is significant, there are still two peaks present in the single particle dark field scattering spectrum, but the coherence is quickly lost due to the fast plasmon damping.

The correct criteria to define strong coupling from experimental observables should be splitting in both the dark-field scattering and the fluorescence spectra, while the splitting in dark-field scattering should exceed the plasmon damping (This is a more strict criterion used in published works compared with Equation 1.3 and Equation 1.4).[44] Splitting in the fluorescence spectra can rule out the possibility of Fano dip since Fano interference does not happen to fluorescence process due to its incoherence.[45] Splitting in the absorption spectra is also sufficient in defining strong coupling, despite the fact that it is more challenging to measure. So here we categorize the plasmon-exciton interaction into three regimes:

Weak coupling regime: The wave functions of the exciton and electromagnetic modes of the plasmon are unperturbed. Only the emission rate of exciton is modified due to Purcell effect.

Intermediate coupling regime: Constructive and destructive interference occurs in the far-field. Fano dip appears in the dark-field scattering spectra of the hybrid structures.

Strong coupling regime: Two new normal modes are generated. Rabi-splitting happens, and both the scattering and fluorescence spectra show peak splitting. The splitting in the dark-field scattering exceeds the plasmon decay rate.

In this Review, we will particularly focus on the advancements of colloidally fabricated plasmon-exciton hybrid structures in the weak and strong coupling regimes. Discussions of hybrid plasmon-exciton structures fabricated using other methods and the intermediate coupling regime are available in these papers.[38, 46]

1.2.3 Plasmon-Exciton Interaction in Colloidally Assembled Metal-QE Nanostructures

1.2.3.1 Weak Coupling regime

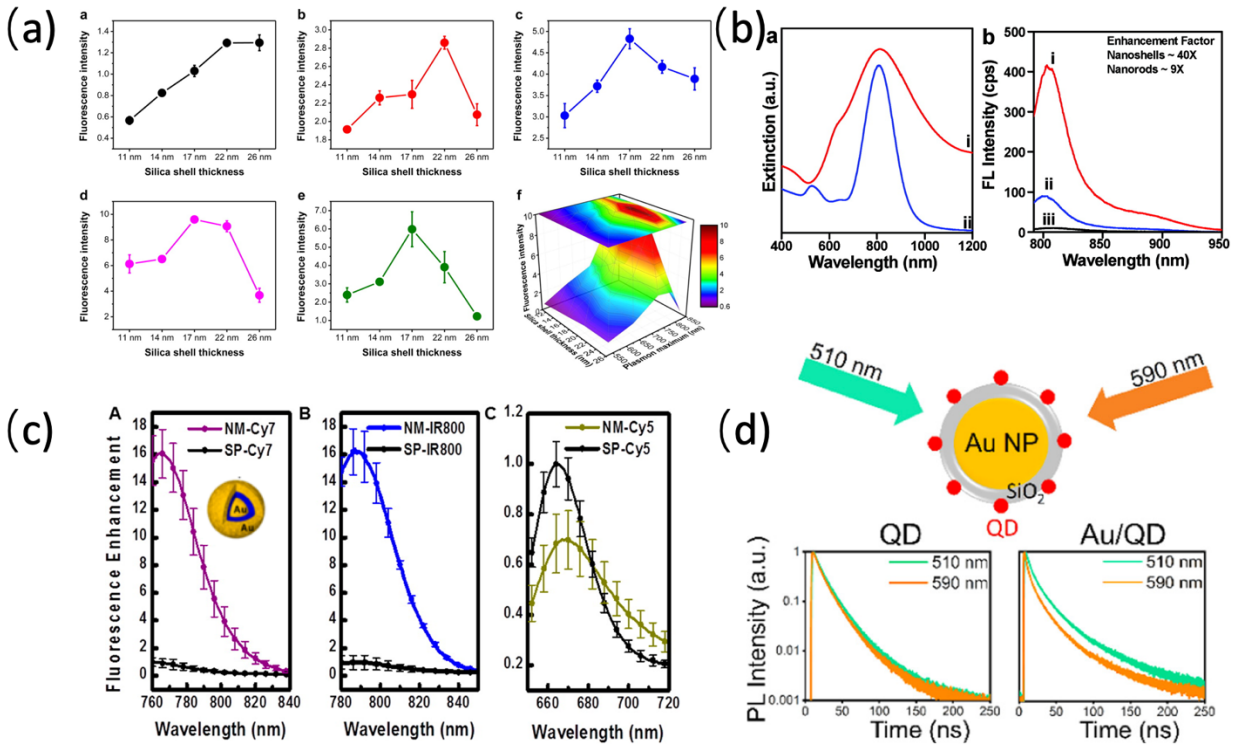

Figure 1.3(a) Distance dependent fluorescence intensity of IRDye on gold nanorod with different lasmon resonance wavelength: black-525 nm, red-650 nm, blue-720 nm, purple-776 nm, green-823 nm and two-tier contour plot showing the distance and plasmon wavelength dependent fluorescence (lower right). Reproduced with permission from Ref. [52], © 2014, American Chemical Society. (b) Extinction spectra of Au nanoshell/nanorod-human serum albumin hybrid structures (left) an fluorescence intensity enhancement caused by nanoshell and nanorods respectively (right). Reproduced with permission from Ref. [53], © 2009, American Chemical Society (c) Fluorescence enhancement factor of Cy7, IR800 and Cy5 dye molecules inside a nanomatryoshka (colored) or seeded precursor (black). Reproduced with permission from Ref. [54], © 2014, American Chemical Society. (d) Schematic illustration of excitation of Au/silica/QD structure with different laser wavelength. Photoluminescence decay curve of bare QD (lower left) and Au/QD hybrid structure (lower right) taken with excitation wavelength of 510 and 590 nm. Reproduced with permission from Ref. [56], © 2018, American Chemical Society.

A good number of research works have been performed in the weak plasmon-exciton coupling regime aiming to investigate the complex plasmon enhanced/quenched fluorescence effect. In this weak coupling regime, previous studies diverge into two areas: 1. building a principle to help develop an optimum hybrid structure with highest possible fluorescence enhancement effect; 2. building a nanoscale sensor/ruler depending on the fluorescence quenching effect. The plasmon enhanced/quenched fluorescence is jointly affected by three processes: 1. local field enhanced absorption rate; 2. enhanced emission rate through Purcell effect; 3. sequential radiative/non-radiative decay of plasmon.

Generally speaking, fluorescence intensity of an emitter can be expressed as:

$$I = \Gamma_{ex} \cdot QY$$

Equation 1.8

where Γ_{ex} is the excitation rate and QY is the quantum yield. For free QEs, the quantum yield can be simply expressed as:

$$QY = \frac{\Gamma_r}{\Gamma_r + \Gamma_{nr}}$$

Equation 1.9

where Γ_r is the radiative decay rate and Γ_{nr} is the nonradiative rate of the QE. When a QE is brought close to a plasmonic nanoparticle, the modified QY is:

$$QY' = \frac{\Gamma_r'}{\Gamma_{total}} + \frac{\Gamma_{Pur}}{\Gamma_{total}} \cdot \frac{\Gamma_r^{pl}}{\Gamma_r^{pl} + \Gamma_{nr}^{pl}}$$

Equation 1.10

Where Γ_{total} is the new total emission rate, Γ_r' is the new rate of emission into the far field, Γ_{Pur} is the rate of emission into plasmon, Γ_r^{pl} is the radiative emission rate of the plasmon and Γ_{nr}^{pl} is the non-radiative rate of plasmon. According to equation 9, the modified QY depends on the characteristics of the QE itself, the efficiency of energy transfer from the QE to the plasmon, and also the radiative efficiency of the plasmonic nanoparticle. Once the energy is transferred from the QE to the plasmonic nanoparticle, the lossy nature of the metal nanoparticle makes it highly possible to dissipate the energy in the form of heat, which means the radiative decay efficiency of the plasmon is very low. This property makes plasmonic nanostructures not very efficient in

enhancing the fluorescence intensity of highly emissive QEs, but rather effective in enhancing the weak processes such as Raman scattering and the emission of the QEs with low QY.

$\ddot{F}oster$ resonance energy transfer (FRET) gives a quantitative estimation of the efficiency of energy transferred to the plasmonic mode, even though it is not the ideal model to describe Purcell effect. Since the plasmonic nanoparticles cannot be treated as a simple dipole in the FRET-like process, the energy transfer is better described as a nanometal surface energy transfer (NSER) process.[47, 48] The rate of energy transfer from the QE to the plasmonic mode is reversely dependent on 2 to 4-th orders of the distance between the QE and plasmonic nanoparticle, instead of the 6-th order in a classical FRET model:

$$\Gamma_{FRET} \propto (\frac{r_0}{r})^{2\sim4}$$

Equation 1.11

Where r_0 depends on various factors such as the QY of the QE, spectral overlap, relative orientation of the exciton with respect to the plasmon resonance and the size of the plasmonic nanoparticle.[49, 50] And r represents the spatial separation between QE and plasmonic nanoparticle.

In order to get the optimum emission enhancement, a series of conditions can be carefully tuned, including changing the composition or structure of the plasmonic nanoparticle, the distance and spatial arrangement between the QE and the nanoparticle, as well as the excitation wavelength. Among all the factors, spectral overlap is the first parameter to be considered since it ensures sufficient energy transfer between plasmon and QE. For example, Murphy's group employed gold nanorods as the plasmonic nanostructure to study the influence of plasmon wavelength on the fluorescence of dye molecules, taking advatage of the widely tunable plasmon wavelength of the nanorods determined by their aspect ratios .[51] They discovered that when the plasmon wavelength

was most close to the absorption peak of the dye molecule, the gold nanorod exhibited the strongest enhancing effect.[52] Figure 1.3a shows that the pink curve (observed in gold nanorod with 776 nm plasmon wavelength that has the best overlap with the 779 nm absorption wavelength of the dye molecules) gives the highest enhancement effect compared with the others. Furthermore, the distance dependent fluorescence enhancement effect was explored by employing silica as the spacing layer between the gold nanorod and the dye molecules. Under the condition of the best spectral overlap, they discovered that a distance of 17 nm yields the strongest enhancement (Figure 1.3a, pink curve). Note that changing the distance between the dyes and the nanorods changes the enhancement of both the absorption and emission rates at the same time. The smaller the distance is, the higher the absorption rate. But the rate of emission into plasmon also increases, resulting in greater non-radiative decay rate of the system due to ohmic loss. Therefore, the optimum enhancing condition is achieved by balancing the desired enhancement of absorption and the unwanted additional non-radiative decay due to ohmic loss.

As indicated in equation 9, the limiting factor that restricts the enhancing performance of plasmonic nanostructures is the competition between ohmic loss and scattering efficiency. An effective way to improve fluorescence enhancement is to increase the scattering cross-section of the hybrid system. The Halas's group reported that at similar plasmon resonance wavelength, the nanoshell has a greater scattering cross-section compared to nanorod due to its bigger physical size. As a result, the enhancement factor of a nanoshell was 4 times greater than that of a nanorod when these two has the same plasmon resonance frequency (Figure 1.3b).[53] Another strategy of increasing the fluorescence enhancement is to induce excited subradiant mode. In a different study by the Halas's group, they demonstrated that the excited subradiant mode in a nanomatryoshka

(i.e. gold core/dye/gold shell) effectively enhance the fluorescence intensity of the dye molecules due to the very strong local field enhancement (Figure 1.3c).[54]

In addition to the nanostructures themselves, external factors can also affect the plasmon-exciton interaction. In the work by Zhao's group, a system composed of colloidal quantum dots attached to Au nanoparticles was investigated. They demonstrated that the fluorescence decay rate can be altered by changing the excitation wavelength, which is very counter-intuitive (Figure 1.3d).[55, 56] They observed that the closer the excitation is to the plasmon resonance, the faster the fluorescence decay of the system is. The observation violates the well-known Kasha's rule, suggesting the "on" or "off" excitation of plasmon resonance could affect plasmon-exciton interaction.

1.2.3.2 Strong coupling regime

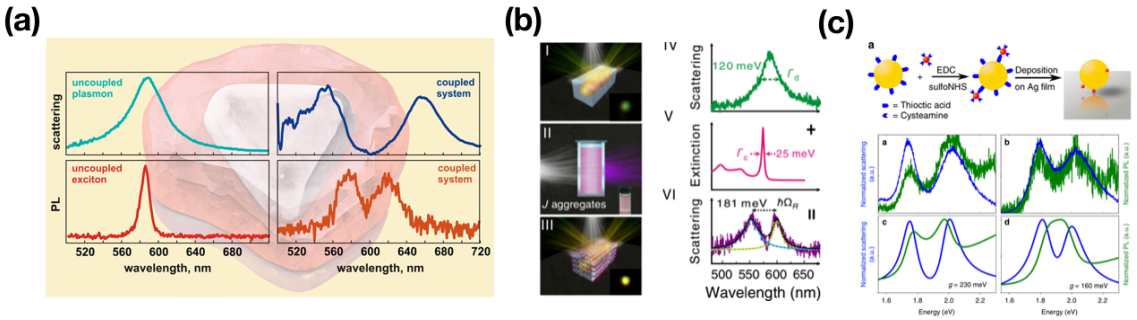

Figure 1.4 (a) Strong coupling in silver prism@J-aggregate core@shell structure. Free silver nanoprism and J-aggregate show single peaks in their single particle dark-field scattering and fluorescence spectra, while the strongly coupled silver prism@J-aggregate core@shell structure showed peak splitting. Reproduced with permission from Ref. [61], © 2017, American Chemical Society. (b) Schematic illustration of single particle dark-field scattering spectra measurement of J-aggregate coated Ag@Au nanorod cuboid structure with the inset of the dark field image of a single structure. The single particle dark-field scattering spectrum show peak splitting. Reproduced with permission from Ref. [62], © 2017, American Physical Society. (c) Schematic illustration of the Au quasi-sphere-QD-silver film fabrication process. Strong coupling of a single quantum dot with the gap mode created by a gold nanoparticle and silver film. Reproduced with permission from Ref. [45], © 2018, Springer Nature

While weak coupling can take place when the plasmonic nanoparticle-QE distance is above the quantum tunneling limit,[23] the strong coupling effect usually requires closer distance as the coupling strength increases with increased distance.[43, 57] The threshold distance between the strong and weak coupling regimes is very difficult to determine, and it highly depends on the specific systems of interest. Fundamentally, to ensure strong coupling and visibility of peak splitting in the

spectra, the coupling strength should be maximized and the decay rate should be minimized, according to Equation 1.3 and Equation 1.4.

The coupling strength is defined as:

$$g = \sqrt{N}\mu_{ex}|E_{vac}|$$

Equation 1.12

where N is the number of excitons, μ_{ex} is the trasnsition dipole moment of the exciton, and E_{vac} is the vacuum electric field. Here E_{vac} scales with $\sqrt{1/V}$, where V is the plasmon mode volume. Therefore, in the simplest scheme, entering strong coupling regime comes down to manipulating four parameters: number of excitons, transition dipole moment of the exciton, plasmon mode volume, and decay rates of both plasmon and exciton.

The first step of constructing the plexcitonic structure is the selection of QEs and plasmonic nanoparticles. J-aggregates outstands most of their peers due to its large transition dipole moment and narrow spectral linewidth.[38, 58] In terms of the selection of plasmonic cavities, silver is usually better than gold due to its low loss and high quality factor(Q).[17, 59] So far, a big number of achieved plexcitonic structures fabricated with colloidal methods are a combination of J-aggregates and silver nanoparticles in a simple core-shell geometry.[44, 60-63] However, even though plasmonic nanostructure surpasses optical cavities with their small mode volume, it still suffers from its low Q. Therefore, a stronger coupling strength g is required to build plexcitonic structure at ambient conditions. To increase g, most researchers chose to further decrease the mode volume V. Silver nanoprism is one option that offers stronger localization of the electromagnetic modes on its tips. Wers$\ddot{a}$ll et.al demonstrated strong coupling effect in J-aggregate coated silver prisms (Figure 1.4a).[61] Splitting in both the dark field scattering and fluorescence spectra were observed. Since

the electron-phonon interaction contributes to the broadening of the fluorescence peak, performing the experiment at cryogenic temperature effectively narrows the linewidth and helps meeting the strong coupling requirement. It was confirmed in Wersäll's work that cooling the system to cryogenic temperature led to a more profound splitting effect in fluorescence. Strong coupling with a single QE is of great interest as it realizes single photon nonlinearity. Liu et.al showed that in their J-aggregate coated Ag@Au nanorod cuboid structure, strong coupling between single exciton and plasmonic cavity was observed.[62] They were able to assemble a monolayer of J-aggregates on the Ag@Au nanorod cuboid surface simply by decreasing the dye concentration. By fitting the experimental spectra to theoretical model, they calculated the coupling strength of the system and confirmed that strong coupling happened between a single emitter and the Ag@Au nanorod cuboid structure (Figure 1.4b).[62]

In addition to J-aggregates, colloidal quantum dots (QDs) have also been applied in the hybrid structures to achieve strong plasmon-exciton coupling, even at the single QD level. When a single QD is chosen as the QE, placing it right at a specific location on a plasmonic nanoparticle is very tricky. An strategy to achieve strong localization of plasmon for a small mode volume is to employ gap mode plasmon.[33, 45, 57, 64] Leng et.al developed a semi-colloidal method to place a single QD in between a quasi-spherical gold nanoparticle and a silver film (Figure 1.4c)[45]. This method created gaps with random orientation and uncertain geometry, because the gaps can be created in between the flat side or a sharp edge/apex of the quasi-spherical Au nanoparticle and the silver film. Taking advantage of the randomness of the system, plasmon-exciton coupling has been observed in weak (QD not incorporated into the gap), intermediate (QD incorporated into the gap created by a flat facet and the silver film), and also strong coupling regimes (QD incorporated into the gap created by edge/apex and the silver film). However, electron microscopy imaging of

the optically studied nanostructures is still needed to provide direct evidence of all these hypotheses.

All these exciting achievements in single emitter induced strong plasmon-exciton coupling showed the power of colloidal methods in fabricating well defined structure with strong coupling effect.

1.2.3.3 Spatial control of the hybrid structures and the corresponding optical properties

Many hybrid QE-plasmonic nanoparticle nanostructures have been fabricated in the past.[16] While colloidal method has demonstrated its capability of successfully linking QEs to plasmonic nanoparticles with controlled separation distance and high uniformity, it is more advantageous in its potential to achieve precise control of the spatial arrangement and the number of the two constituents incorporated. Precise structural control of the plasmon-exciton hybrid structure is of ultimate importance to reveal the underlying structure-correlated physical processes, especially in anisotropic nanostructures[65]. This section focuses on hybrid nanostructures composed of Au nanoparticles and CdSe-based colloidal QDs, which are the two mostly studied and characterized nanocrystals.

Since the plasmon-exciton coupling depends on the spatial arrangement of the metal nanoparticles and QDs, it is critical to control their relative position in a hybrid structure. Nepal et.al took advantage of the different ligand binding affinity on different Au nanorod facets to control the selective binding of QDs (Figure 1.5a).[66] Briefly, the Au nanorod can be specifically functionalized with aminoalkylthiols on the ends/whole surface at high/low cetryltrimethylammonium chloride (CTAC) concentrations. The QDs capped with-amine terminated polyethylene glycol (PEG) can therefore be linked to the thiol group on the rod surface with the assistance of Traut's reagent to form a disulfide bridge. The binding of QD can be simply

tuned from end only to the whole surface or even multiple layers by controlling the amount of aminoalkylthiols on the surface and QD stoichiometric ratio. Moreover, the distance between the QD and Au nanorod surface can be varied by changing the alkyl chain length of the aminoakkylthiols ligand.

QDs can also be incorporated into gaps between Au nanoparticles to access the "hot spots" to realize strong fluorescence enhancement. Cohen-Hoshen et.al used DNA as linker molecules to fabricate one or multiple QDs to Au or even Au-QD-Au sandwich structures (Figure 1.5b). [67] These structures were further separated through electrophoresis separation for optical studies. When they varied the polarization of laser excitation to tune the local field around the Au nanoparticles, they extracted the absorption enhancement of the QDs, resulted from the local field of plasmon resonance. An absorption enhancement of 7 was calculated by dividing the fluorescence enhancement factor acquired with laser polarization aligned to the Au-QD axis by that obtained when the polarization was aligned perpendicular to Au-QD axis. Using the same method, an absorption enhancement factor of 100 was determined for the Au-QD-Au structure.

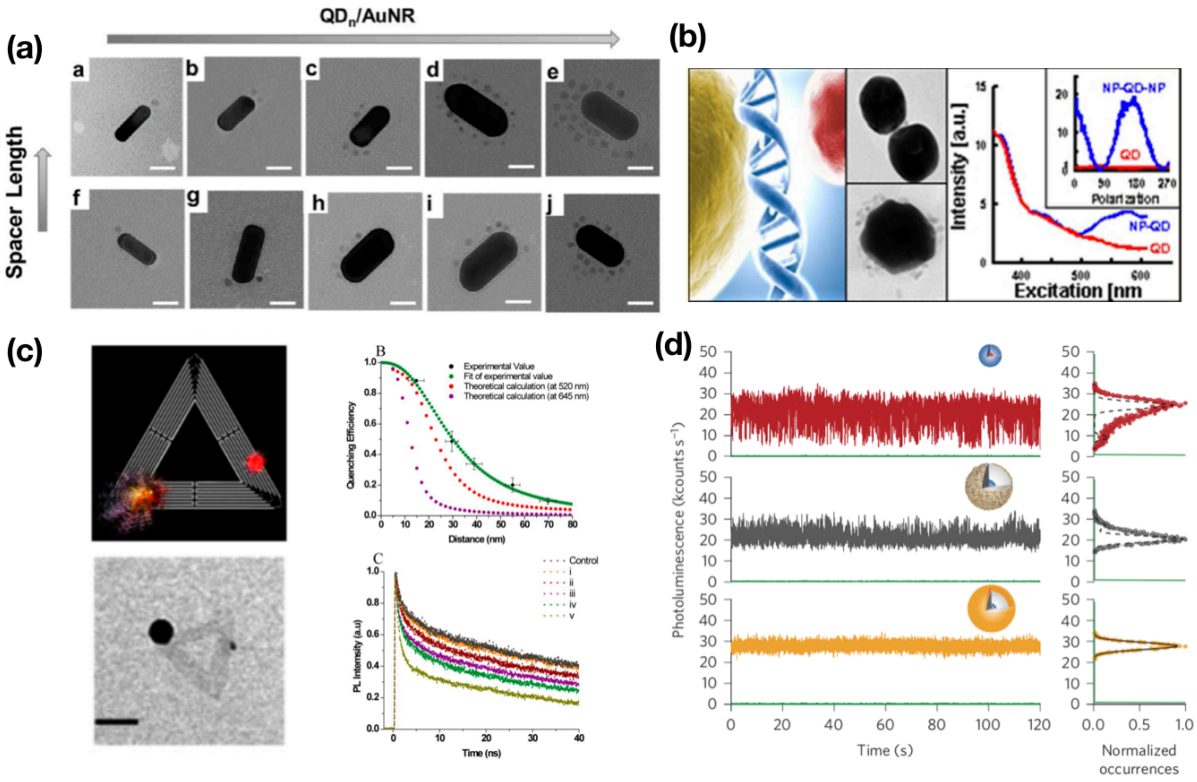

Figure 1.5 a) Controlling the QD distribution on a gold nanorod by changing the amount of QD and spacer material. Reproduced with permission from Ref. [66], © 2013, American Chemical Society (b) Assembling Au-QD structure with DNA as linker. The plasmon enhanced fluorescence showed excitation polarization dependence. Reproduced with permission from Ref. [67], © American Chemical Society 2012. (c) Using DNA origami to precisely control the distance between gold nanoparticle and QD, demonstrating the distance dependent quenching effect. Reproduced with permission from Ref. [68], © American Chemical Society 2014. (d) Fluorescence intensity of bare CdSe/CdS QD (top), QD-silica-Au seeds (middle) and QD-silica-Au shell(bottom) as a function of time. QD-silica-Au shell exhibit reduced blinking effect. Reproduced with permission from Ref. [72], © Springer Nature 2015.

In addition to using simple DNA strands to link QDs and plasmonic nanoparticles together, DNA origami, a sophisticated nanoscale architecture full of possibilities, can do much more in terms of constructing a well-organized structure. Samantha et.al used DNA origami to construct a one to one Au-QD structure with precisely controlled distance between the Au nanoparticle and QD (Figure 1.5c).[68] This one to one geometry and precise distance control from 15 to 70 nm allows precise profiling of distance dependent fluorescence quenching through a FRET-like process. Zhang et.al used DNA origami to fabricate Au nanorod dimer structure to investigate the impact of gap distance on fluorescence enhancement effect.[69] It was discovered that the highest enhancement was achieved with the smallest gap size. The DNA origami was also applied to assemble Au nanoparticle dimers with the J-aggregates placed in the gap to demonstrate strong coupling effect.[70]

Not only fluorescence enhancement/quenching, coupling QDs to Au nanoparticles also alters the fluorescence "blinking" behavior of single QDs. It is discovered that coupling QD to plasmonic nanostructures can effectively reduce blinking.[71] Ji et.al reported that the golden QD (QD/silica/Au shell) structure exhibits non-blinking effect due to Purcell effect (Figure 1.5d).[72] The Au shell also effectively promotes the stability of fluorescence against photobleaching.[73] However, coating the QDs with a Au shell is a challenge because the gold ions easily diffuses through the spacing layer to deposit on the QD surface[74], and thus quenches the fluorescence of the QDs.

Hybrid nanostructures have also been fabricated via many non-colloidal methods, which is beyond the scope of this Review.[32-34] With all the hybrid plasmonic nanoparticle-QE structures enumerated in this section, colloidal method has proved its capability of achieving precise spatial and quantity control to achieve exciting functionalities.

1.2.4 Conclusions and Outlook

In this Review, we looked into both quantum mechanical and classical models to understand how the hybrid plasmon-exciton system behave at different coupling strength. The plasmon-exciton interaction is therefore classified into weak, intermediate and strong coupling regimes, each of which needs different theoretical evaluation. In the weak coupling regime, the plasmon-exciton coupling effect is manifested as the enhanced absorption and spontaneous emission of the excitons. In the strong coupling regime, the fast energy exchange between plasmon and exciton leads to peak splitting in the scattering and fluorescence spectra.

Colloidal methods have demonstrated their flexibility of incorporating different types of plasmonic nanoparticles and QEs into one defined hybrid system with controlled geometry. With such capability, colloidal methods allow researchers to fully examine how the key factors such as spectral overlap, plasmon-exciton distance, the intrinsic properties of the plasmonic nanoparticle (loss, scattering cross-section) and also excitation wavelength would affect the performance of the hybrid structure. These findings serve as guidelines to design hybrid plasmon-exciton nanosystems. Some of the hybrid nanostructures have been successfully applied in bio-imaging and sensing.[75-77]

To produce nanostructures in the strong coupling regime, rigorous requirements to reach high coupling strength make the fabrication of these structures more challenging. With the careful selection of QE and plasmonic nanoparticles, the strong-coupling effect has been shown under ambient conditions. However, challenges still hold for fabricating a strongly coupled system with a single emitter, which is highly desired for single photon sources. Such systems require precise control of the ratio between QEs and plasmonic nanoparticles. Moreover, the two components have to be carefully placed in specific locations relative to each other in order to obtain strong

plasmon-exciton coupling. Even with the rapidly developing nanofabrication techniques, it is not an easy task.

With the capability of colloidal method discussed in this Review, we believe colloidal methods can contribute to the future development of strongly coupled plasmon-exciton nanostructures. Successful fabrication of such nanostructures will make it possible to produce exciting nano photonic devices including solar cells, single photon non-linear optics and nano-lasers.

1.3 **Acknowledgements**

We acknowledge the financial supported by NSF CAREER Grant (CHE 1554800).

1.4 **Reference**

1. G. Mie, *Annalen der physik*, 1908, **330**, 377-445.
2. N. Ashcroft and N. Mermin, *Google Scholar*, 1976, 404.
3. S. Link and M. A. El-Sayed, *Annual review of physical chemistry*, 2003, **54**, 331-366.
4. R. v. Gans, *Annalen der Physik*, 1912, **342**, 881-900.
5. M. Grzelczak, J. Pérez-Juste, P. Mulvaney and L. M. Liz-Marzán, *Chemical Society Reviews*, 2008, **37**, 1783-1791.
6. P. Zhao, N. Li and D. Astruc, *Coordination Chemistry Reviews*, 2013, **257**, 638-665.
7. L. Scarabelli, A. Sánchez-Iglesias, J. Pérez-Juste and L. M. Liz-Marzán, *Journal*, 2015.
8. U. Kreibig and M. Vollmer, in *Optical properties of metal clusters*, Springer, 1995, pp. 13-201.
9. O. S. Wolfbeis, *Chemical Society Reviews*, 2015, **44**, 4743-4768.
10. M. Li, S. K. Cushing and N. Wu, *Analyst*, 2015, **140**, 386-406.
11. J. L. West and N. J. Halas, *Annual Review of Biomedical Engineering*, 2003, **5**, 285-292.
12. A. Yang and T. W. Odom, *IEEE Photonics Journal*, 2015, **7**, 1-6.
13. H. Nabika, M. Takase, F. Nagasawa and K. Murakoshi, *The Journal of Physical Chemistry Letters*, 2010, **1**, 2470-2487.
14. V. Giannini, A. I. Fernández-Domínguez, S. C. Heck and S. A. Maier, *Chemical reviews*, 2011, **111**, 3888-3912.
15. P. Zhang, I. Protsenko, V. Sandoghdar and X.-W. Chen, *ACS Photonics*, 2017, **4**, 2738-2744.
16. T. Ming, H. Chen, R. Jiang, Q. Li and J. Wang, *The Journal of Physical Chemistry Letters*, 2012, **3**, 191-202.
17. M. Achermann, *The Journal of Physical Chemistry Letters*, 2010, **1**, 2837-2843.

18. P. Anger, P. Bharadwaj and L. Novotny, *Physical review letters*, 2006, **96**, 113002.
19. F. Tam, G. P. Goodrich, B. R. Johnson and N. J. Halas, *Nano letters*, 2007, **7**, 496-501.
20. V. Amendola, R. Pilot, M. Frasconi, O. M. Marago and M. A. Iati, *Journal of Physics: Condensed Matter*, 2017, **29**, 203002.
21. M. S. Tame, K. McEnery, Ş. Özdemir, J. Lee, S. Maier and M. Kim, *Nature Physics*, 2013, **9**, 329.
22. J. B. Khurgin, *Nature nanotechnology*, 2015, **10**, 2.
23. O. Kulakovich, N. Strekal, A. Yaroshevich, S. Maskevich, S. Gaponenko, I. Nabiev, U. Woggon and M. Artemyev, *Nano Letters*, 2002, **2**, 1449-1452.
24. E. M. Purcell, H. C. Torrey and R. V. Pound, *Physical review*, 1946, **69**, 37.
25. M. Pelton, *Nature Photonics*, 2015, **9**, 427.
26. S. Rodriguez, J. Feist, M. Verschuuren, F. G. Vidal and J. G. Rivas, *Physical review letters*, 2013, **111**, 166802.
27. F. Nan, S.-J. Ding, L. Ma, Z.-Q. Cheng, Y.-T. Zhong, Y.-F. Zhang, Y.-H. Qiu, X. Li, L. Zhou and Q.-Q. Wang, *Nanoscale*, 2016, **8**, 15071-15078.
28. S. E. Harris, J. Field and A. Imamoğlu, *Physical Review Letters*, 1990, **64**, 1107.
29. G. Khitrova, H. Gibbs, M. Kira, S. W. Koch and A. Scherer, *Nature Physics*, 2006, **2**, 81.
30. S. Christopoulos, G. B. H. Von Högersthal, A. Grundy, P. Lagoudakis, A. Kavokin, J. Baumberg, G. Christmann, R. Butté, E. Feltin and J.-F. Carlin, *Physical review letters*, 2007, **98**, 126405.
31. B. Kolaric, B. Maes, K. Clays, T. Durt and Y. Caudano, *arXiv preprint arXiv:1802.06029*, 2018.
32. T. B. Hoang, G. M. Akselrod and M. H. Mikkelsen, *Nano letters*, 2015, **16**, 270-275.
33. H. Groß, J. M. Hamm, T. Tufarelli, O. Hess and B. Hecht, *Science advances*, 2018, **4**, eaar4906.
34. H. Mundoor, G. H. Sheetah, S. Park, P. J. Ackerman, I. I. Smalyukh and J. van de Lagemaat, *ACS nano*, 2018, **12**, 2580-2590.
35. N. Liu, B. S. Prall and V. I. Klimov, *Journal of the American Chemical Society*, 2006, **128**, 15362-15363.
36. M. R. Jones, K. D. Osberg, R. J. Macfarlane, M. R. Langille and C. A. Mirkin, *Chemical reviews*, 2011, **111**, 3736-3827.
37. Y. Wang, G. Chen, M. Yang, G. Silber, S. Xing, L. H. Tan, F. Wang, Y. Feng, X. Liu and S. Li, *Nature communications*, 2010, **1**, 87.
38. D. G. Baranov, M. Wersäll, J. Cuadra, T. J. Antosiewicz and T. Shegai, *Acs Photonics*, 2017, **5**, 24-42.
39. T. Hümmer, F. García-Vidal, L. Martín-Moreno and D. Zueco, *Physical Review B*, 2013, **87**, 115419.
40. T. Hartsfield, W.-S. Chang, S.-C. Yang, T. Ma, J. Shi, L. Sun, G. Shvets, S. Link and X. Li, *Proceedings of the National Academy of Sciences*, 2015, **112**, 12288-12292.
41. B. Luk'yanchuk, N. I. Zheludev, S. A. Maier, N. J. Halas, P. Nordlander, H. Giessen and C. T. Chong, *Nature materials*, 2010, **9**, 707.
42. J. A. Faucheaux, J. Fu and P. K. Jain, *The Journal of Physical Chemistry C*, 2014, **118**, 2710-2717.
43. Z.-J. Yang, T. J. Antosiewicz and T. Shegai, *Optics express*, 2016, **24**, 20373-20381.
44. G. Zengin, M. Wersäll, S. Nilsson, T. J. Antosiewicz, M. Käll and T. Shegai, *Physical review letters*, 2015, **114**, 157401.

45. H. Leng, B. Szychowski, M.-C. Daniel and M. Pelton, *Nature communications*, 2018, **9**, 4012.
46. X. Li, L. Zhou, Z. Hao and Q. Q. Wang, *Advanced Optical Materials*, 2018, **6**, 1800275.
47. T. Jennings, M. Singh and G. Strouse, *Journal of the American Chemical Society*, 2006, **128**, 5462-5467.
48. C. J. Breshike, R. A. Riskowski and G. F. Strouse, *The Journal of Physical Chemistry C*, 2013, **117**, 23942-23949.
49. T. Sen and A. Patra, *The Journal of Physical Chemistry C*, 2012, **116**, 17307-17317.
50. M. Li, S. K. Cushing, Q. Wang, X. Shi, L. A. Hornak, Z. Hong and N. Wu, *The Journal of Physical Chemistry Letters*, 2011, **2**, 2125-2129.
51. J. Pérez-Juste, I. Pastoriza-Santos, L. M. Liz-Marzán and P. Mulvaney, *Coordination chemistry reviews*, 2005, **249**, 1870-1901.
52. N. S. Abadeer, M. R. Brennan, W. L. Wilson and C. J. Murphy, *ACS nano*, 2014, **8**, 8392-8406.
53. R. Bardhan, N. K. Grady, J. R. Cole, A. Joshi and N. J. Halas, *ACS nano*, 2009, **3**, 744-752.
54. C. Ayala-Orozco, J. G. Liu, M. W. Knight, Y. Wang, J. K. Day, P. Nordlander and N. J. Halas, *Nano letters*, 2014, **14**, 2926-2933.
55. S. Dey, Y. Zhou, Y. Sun, J. A. Jenkins, D. Kriz, S. L. Suib, O. Chen, S. Zou and J. Zhao, *Nanoscale*, 2018, **10**, 1038-1046.
56. T. J. Wax, S. Dey, S. Chen, Y. Luo, S. Zou and J. Zhao, *ACS Omega*, 2018, **3**, 14151-14156.
57. K. Santhosh, O. Bitton, L. Chuntonov and G. Haran, *Nature communications*, 2016, **7**, ncomms11823.
58. F. Würthner, T. E. Kaiser and C. R. Saha-Möller, *Angewandte Chemie International Edition*, 2011, **50**, 3376-3410.
59. M. I. Stockman, *Optics express*, 2011, **19**, 22029-22106.
60. S. Balci, B. Kucukoz, O. Balci, A. Karatay, C. Kocabas and G. Yaglioglu, *Acs Photonics*, 2016, **3**, 2010-2016.
61. M. Wersäll, J. Cuadra, T. J. Antosiewicz, S. Balci and T. Shegai, *Nano letters*, 2016, **17**, 551-558.
62. R. Liu, Z.-K. Zhou, Y.-C. Yu, T. Zhang, H. Wang, G. Liu, Y. Wei, H. Chen and X.-H. Wang, *Physical review letters*, 2017, **118**, 237401.
63. G. Zengin, G. Johansson, P. Johansson, T. J. Antosiewicz, M. Käll and T. Shegai, *Scientific reports*, 2013, **3**, 3074.
64. A. E. Schlather, N. Large, A. S. Urban, P. Nordlander and N. J. Halas, *Nano letters*, 2013, **13**, 3281-3286.
65. T. Ming, L. Zhao, Z. Yang, H. Chen, L. Sun, J. Wang and C. Yan, *Nano letters*, 2009, **9**, 3896-3903.
66. D. Nepal, L. F. Drummy, S. Biswas, K. Park and R. A. Vaia, *ACS nano*, 2013, **7**, 9064-9074.
67. E. Cohen-Hoshen, G. W. Bryant, I. Pinkas, J. Sperling and I. Bar-Joseph, *Nano letters*, 2012, **12**, 4260-4264.
68. A. Samanta, Y. Zhou, S. Zou, H. Yan and Y. Liu, *Nano letters*, 2014, **14**, 5052-5057.
69. T. Zhang, N. Gao, S. Li, M. J. Lang and Q.-H. Xu, *The journal of physical chemistry letters*, 2015, **6**, 2043-2049.

70. E.-M. Roller, C. Argyropoulos, A. Högele, T. Liedl and M. Pilo-Pais, *Nano letters*, 2016, **16**, 5962-5966.
71. X. Ma, H. Tan, T. Kipp and A. Mews, *Nano letters*, 2010, **10**, 4166-4174.
72. B. Ji, E. Giovanelli, B. Habert, P. Spinicelli, M. Nasilowski, X. Xu, N. Lequeux, J.-P. Hugonin, F. Marquier and J.-J. Greffet, *Nature nanotechnology*, 2015, **10**, 170.
73. Y. Jin and X. Gao, *Nature nanotechnology*, 2009, **4**, 571.
74. N. S. Karan, A. M. Keller, S. Sampat, O. Roslyak, A. Arefin, C. J. Hanson, J. L. Casson, A. Desireddy, Y. Ghosh and A. Piryatinski, *Chemical science*, 2015, **6**, 2224-2236.
75. J. R. Lakowicz, *Plasmonics*, 2006, **1**, 5-33.
76. C. D. Geddes, H. Cao, I. Gryczynski, Z. Gryczynski, J. Fang and J. R. Lakowicz, *The Journal of Physical Chemistry A*, 2003, **107**, 3443-3449.
77. M. Bauch, K. Toma, M. Toma, Q. Zhang and J. Dostalek, *Plasmonics*, 2014, **9**, 781-799.

Chapter Two : Plasmonic Coupling in Single Flower-like Gold Nanoparticle Assemblies

2.1 Abstract

Localized surface plasmon resonance (LSPR) arises when light interacts with metallic nanoparticles (NPs). When nanoparticles (NPs) assemble together, the plasmon coupling effect between the NPs often leads to new features in the assembled structure. Understanding the plasmon coupling in the complex assemblies will greatly benefit the development of new plasmonic devices. Here we demonstrate the fabrication of a 3D structure using two different sized Au NPs as building blocks. This 3D structure is achieved by manipulating the binding efficiency of ligands linking the NPs, and proper choice of the NP size. The assembled structure is flower-like structure, with one 130 nm Au NP in the center, and several 40 nm Au NPs attaching as “petals”. Single particle dark-field scattering spectrum of the individual assemblies were carried out, together with electrodynamics simulations. The experimental and theoretical studies show that, the plasmonic coupling lead to broadening of the LSPR and additional peaks, depending on the number and 3D arrangement of the 40 nm NPs around the center 130 nm NP.

2.2 Introduction

When metal materials are minimized to nanoscale, quantum confinement starts to take effect and the properties of the materials become very different from those of the bulk. Driven by

the electromagnetic field of the incident light, the free electrons on the surface of metal nanoparticles (MNPs) can oscillate coherently at certain frequencies. This phenomenon is known as localized surface plasmon resonance (LSPR).[1-4] LSPR generates an enhanced electromagnetic field adjacent to the surface of the NP. [5-7] This near field effect can be applied to enhance fluorescence or Raman scattering of the molecules close to the surface.[8-14] When two or more NPs are brought close together, the interaction between the plasmons of each particle gives rise to highly enhanced electromagnetic field at the "hot spots", much stronger than the field around single particles. [15-19] Therefore, the NP clusters are more favorable for surface enhanced spectroscopies.

Assembly of NPs into a higher-order structure can artificially create many hot spots in the structure. By modifying the NP surface with molecular linkers such as DNA, polymer, or small organic molecules, Au NPs have been successfully linked together to form assembled structures.[20-25] Here we demonstrate an assembly method using 3-mercaptopropionate(3-MTP) as the linking ligand. 40 nm Au NP and 130 nm Au NP are chosen as the building blocks to achieve the flower-like nanostructure.

To better utilize the assembled nanostructures and design the structures with desired functionality, it is critical to understand the coupling effect at the single particle level. [26-31] Single particle dark field study reveals plasmonic features in single particles/assemblies that are not resolvable in ensemble ultraviolet-visible (UV-vis) spectrum. Our single particle dark-field scattering results show that the assembled structure has two scattering peaks due to the plasmon coupling effect between the center and satellite Au NPs. Electrodynamics simulations reveal that the scattering spectra of the assemblies highly depend on the number and how the satellite particles

are arranged around the center. This flower-like model provides a new system to study plasmonic coupling in a 3D structure consisted of different sized components.

2.3 Experimental Methods

2.3.1 Chemicals and Materials

Gold (III) chloride trihydrate ($HAuCl_4$), hydroxylamine hydrochloride ($NH_2OH{\cdot}HCl$), were purchased from Sigma-Aldrich. Sodium citrate, ethanol, were purchased from Fisher Scientific.

2.3.2 Methods

2.3.2.1 Synthesis of Au Nanoparticles

Frens' method was adopted to synthesize the 40nm Au NPs. [32] To prepare the 40 nm AuNP: 1.06 mL of $HAuCl_4$ solution (0.0254 M) and 99 mL of distilled water were loaded into a 250 mL flask and heated to boil, followed by addition of 1.0 mL of the sodium citrate solution (0.0388 M). After stirring and heating for 15 mins, the heating was turned off and the reaction solution was allowed to cool to room temperature with stirring.

A previously reported seed mediated method was used to prepare 130 nm gold colloids. [33] Briefly, 4 mL of the as-made NP solution synthesized in step one, 52 mL of DI water, and 900 μL of sodium citrate solution (0.0388 M) were loaded into the flask, respectively. After stirring for 5 mins, 0.88 mL of $HAuCl_4$ (0.0254 M) was injected into the above solution and the mixed solution was kept stirring for another 5 mins. Finally, 700 μL of hydroxylamine hydrochloride solution (0.0101 M) was injected into the flask containing the Au NP solution twice and the reaction solution was allowed to incubate for 2 hrs.

2.3.2.2 Synthesis of 130@40 nm Au NP assembly

A previously reported method was adapted to synthesize the assembled structure (see Scheme 1). [34] The first step is to ligand exchange the citrate capped 130 nm gold nanoparticle with a 4-thiol ligand-3-mercaptopropionate(3-MTP). 3 mL of DMF and 18 μL of 3-MTP were loaded into the flask, and 0.5 mL of 130 nm Au solution (in DMF) was injected into the above solution drop by drop. After incubating the reaction solution for 2 hrs, the products were purified by the centrifugation and washed with DMF once and with ethanol for three times. The second step is to attach 40 nm Au NPs on the surface of 130 nm 3-MTP modified Au NPs. 40 nm Au NPs were dispersed in 2 mL of a 12 mM NaCl salt solution and 130 nm 3-MTP modified Au NPs were redispersed in 2 mL of ethanol, respectively. After 130 nm Au NPs solution was added into 40 nm Au solution drop by drop, the mixed Au NPs solution was allowed to incubate for a couple of mins to assemble into flower-like structures.

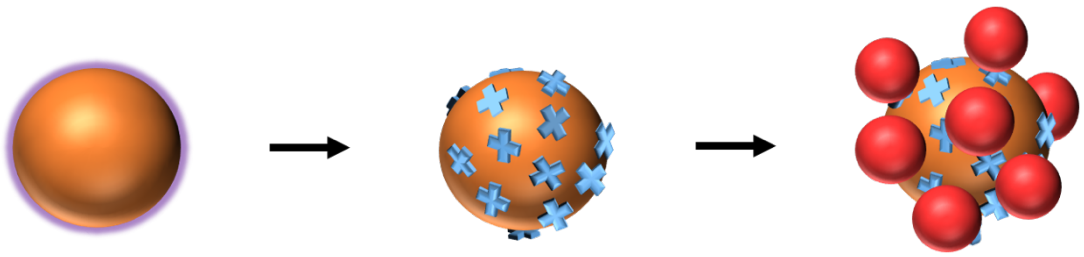

Scheme 2.1. Assembly scheme of the 130 nm Au NP@40 nm Au NP structure.

2.3.2.3 Dark-field scattering

The assembled sample was diluted with water by 1600 times with DI water and then 3μL of the solution was dropped onto the cleaned glass slide. The glass slide was dried under air for 2 hrs.

Then the sample was examined under Nikon Ti-u microscope with an unpolarized halogen lamp. The dark field condenser (NA 0.85) was adjusted to focus at the specimen plane. The signal was collected by a 100× NA 0.8 objective (variable NA 0.8–1.3) and then passed thought a manually controlled slit to the spectrograph (Isoplane SCT 320, Princeton Instruments) equipped with a CCD camera (PIXIS 1024 BR, Princeton Instruments). Single particle signal was acquired from areas with very low density of particles. Single particle spectra were collected by narrowing the slit and selecting proper area of interest. The spectrum correction was carried out by subtracting and then dividing the background signal collected from nearby area with no particles.

2.3.2.4 Characterization of flower-like Au NP assemblies

A UV−Vis spectrometer (Cary 60, Agilent Technologies) was used to measure the extinction spectrum of the 40 nm and 130 nm Au NPs in solution. FEI Tecnai G2 Spirit BioTWIN

is used to acquire the transmission electron microscopy (TEM) images and FEI Nova NanoSEM 450 is used to acquire scanning electron microscopy (SEM) images.

To prepare SEM sample, the solution is diluted by 1600 times with DI water and 3μL of the solution was dropped onto the glass slide. The glass slide is left in air for 2 hrs to dry completely. The as-prepared sample is then coated with gold for 40 s to increase conductivity.

2.3.2.5 Theory

The discrete dipole approximation (DDA) method was used to model the scattering spectra of the assemblies prepared in the experiments. [35] The detailed discussion of the DDA method can be found in the reference by Draine. Briefly, the target structure is represented with an array of polarizable cubes and the interactions between the excited dipoles and incident light are solved using electrodynamics theory. The scattering spectra of the target structures can be obtained consequently. In our calculations, the dielectric constants of Au are obtained from the Palik Handbook. [36]

2.4 Results and Discussion

2.4.1 Single Particle Dark-field Scattering of Assembled Structures

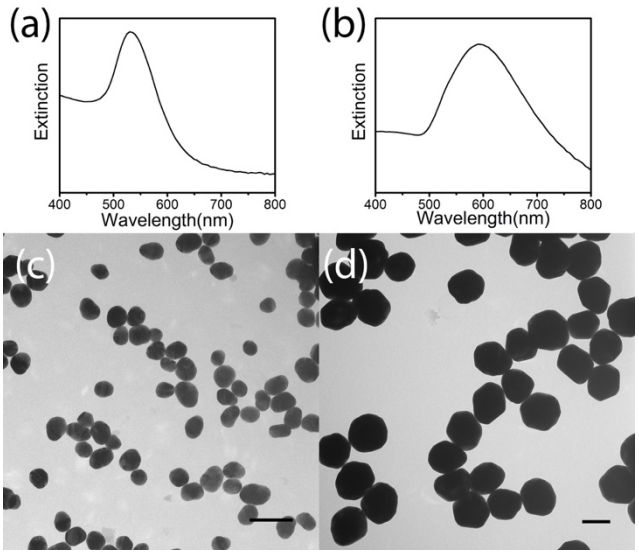

Figure 2.1. UV-vis spectra and TEM images of (a) and (c) 40 nm Au NP, (b) and (d) 130 nm Au NP. Scale bar = 100 nm.

Figure 2.1 shows the UV-vis spectra and TEM images of the Au NP building blocks. The extinction peaks of the NPs are at 532 nm and 594 nm, respectively. The average size of the satellite Au NPs is 40 nm and the average size of the center Au NP is 130 nm. To link the 40 nm Au NPs with the 130 nm Au NPs, the surface of the 130 nm Au NPs is functionalized with 4-thiol ligands through ligand exchange. The 130 nm Au NPs were originally capped with citrate molecules. Once they were added into the 4-thiol solution, the 4-thiol molecules would replace the citrate ligands because the binding ability of thiol to Au is stronger than carboxyl to Au.[37] When an excess amount of the 4- thiol ligands was present in the solution, the 130 nm Au NPs underwent a complete ligand exchange process and the full layer of 4-thiol ligand would prevent the

aggregation of 130 nm Au NPs. It is believed that not all the thiols in the 4-thiol ligands are bound to Au. Therefore, there are some free thiols available for binding.[34] Thus, after mixing the functionalized 130 nm Au NPs with the citrate capped 40 nm Au NPs, the additional thiol groups on the surface of 130 nm Au NPs would replace the citrate group on the 40 nm Au NPs and link them together.

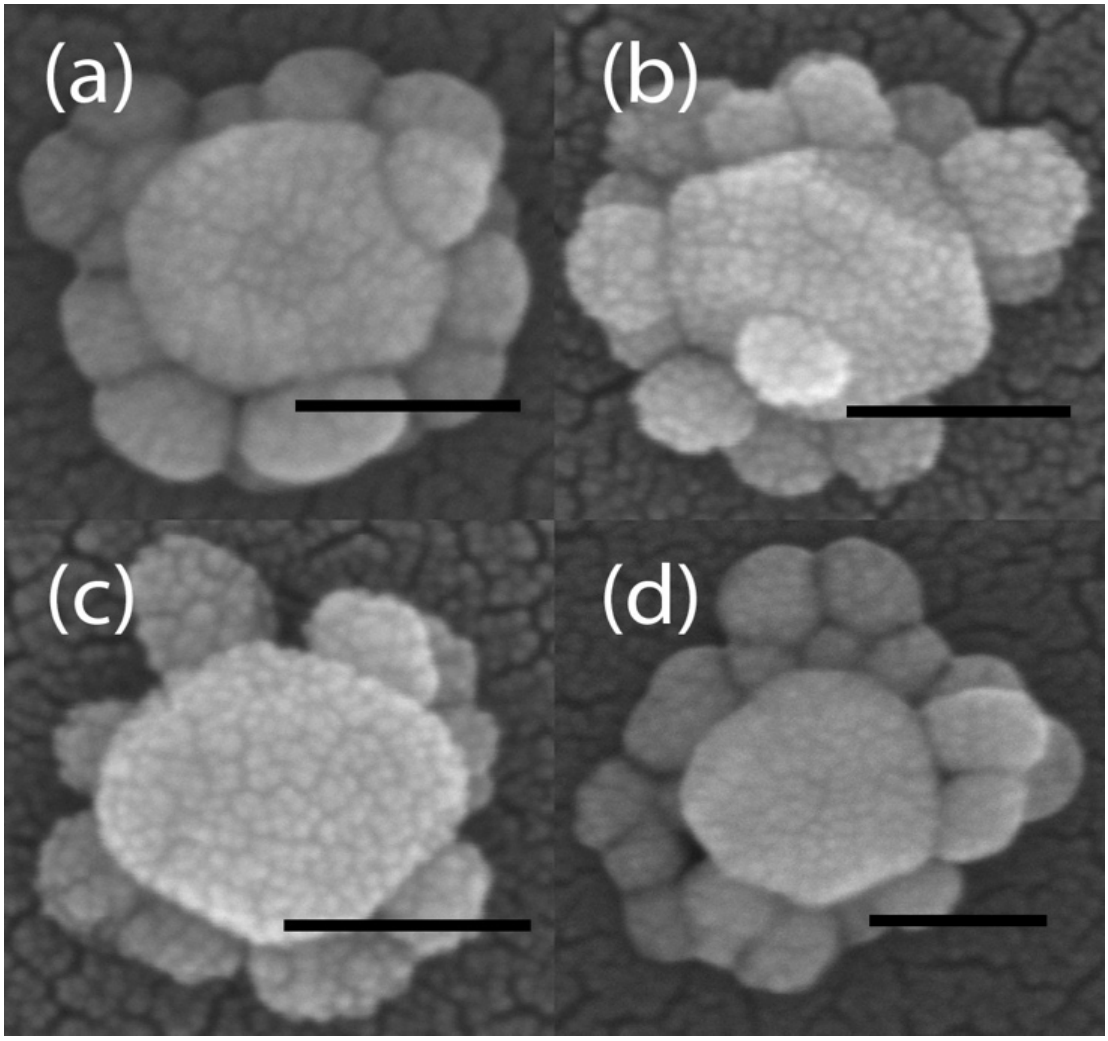

Figure 2.2. SEM images of four assembled structures. Scale bar = 100 nm.

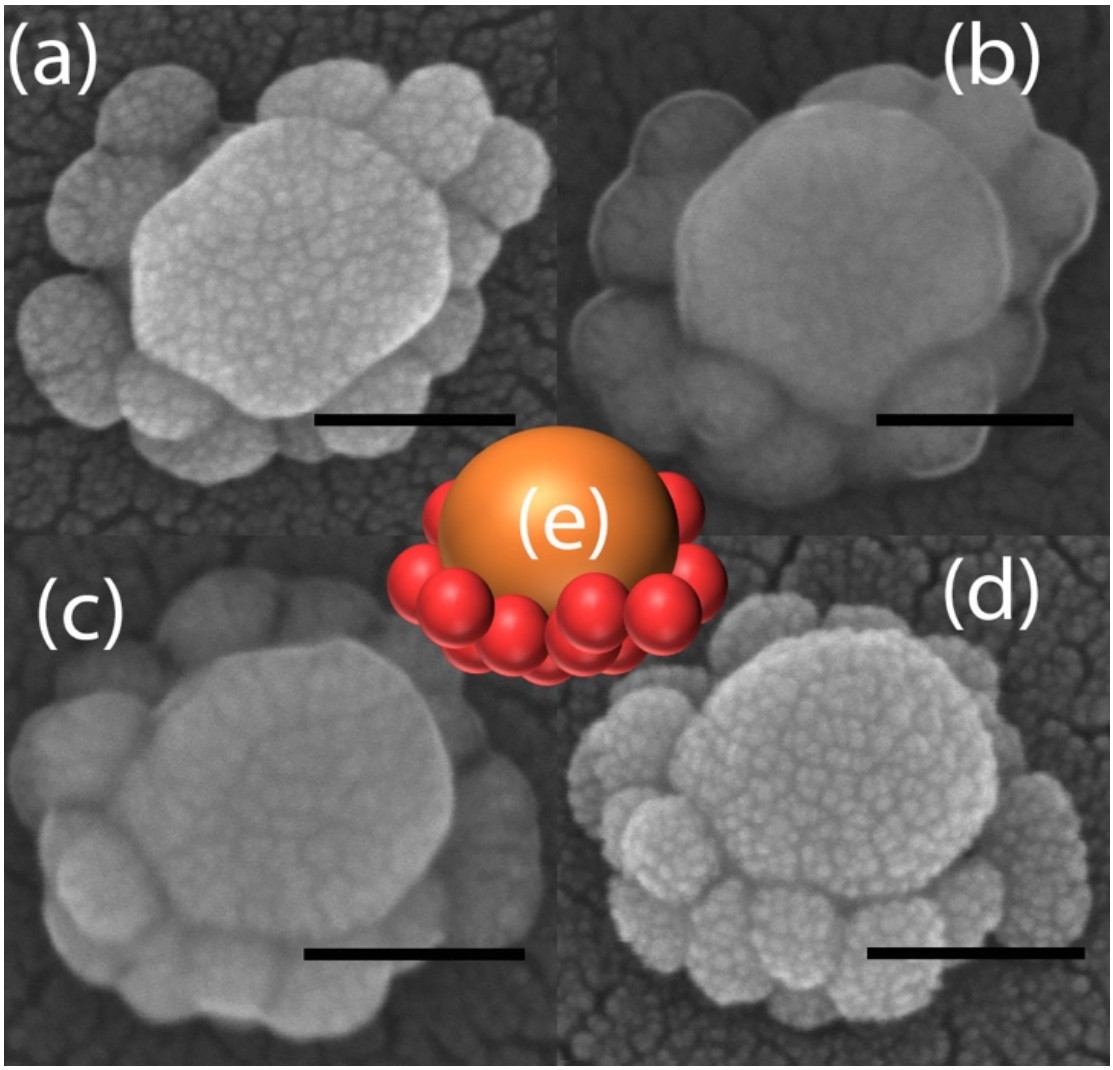

Figure 2.3. SEM images of the assembled structures taken at 0 degrees tilt angle (a, c) and 20 degrees tilt angle (b, d). Scale bar=100 nm.

As the 4 thiol ligand should not just specifically attach to one side of the gold, we expect the assembled structure should have a sub-monolayer of 40 nm Au NPs randomly attached to the surface of the 130 nm Au NP. However, The SEM image tells a different story. Figure 2.2 shows that almost all the 40 nm Au NPs sit at the bottom the 130 nm Au NP, suggesting once the assembled structure dries on the substrate, the 40 nm Au NPs fall off the top of the 130 nm Au NP. It is possibly due to the inefficient linking effect of the thiol ligands. As the Au NPs becomes too

big, the force between the thiol ligand and the gold surface is not strong enough to resist the surface tension of the solution dries on the substrate, the 40 nm Au NPs fall off the top of the 130 nm Au NP. It is possibly due to the inefficient linking effect of the thiol ligands. As the Au NPs become too big, the force between the thiol ligand and the gold surface is not strong enough to resist the surface tension of the solution and hold the 40 nm Au NPs on top of the 130 nm Au NPs during the drying process. Figure 2.3 shows the SEM images of the same structure before and after the sample stage is tilted under the microscope. The images prove that the 40 nm Au are actually attaching to the 130 nm Au instead of randomly sitting around.

To ensure efficient assembly into the flower-like structure, there needs to be a large excess of 40 nm Au NPs. In addition, it is also critical to control the ionic strength of solution. [38] The 40 nm Au NPs form a denser layer on the 130 nm Au NP with a greater ionic strength. However, high ionic strength can also induce aggregation of the assemblies.[39, 40] To achieve the optimal conditions, a series of ionic strength controls were carried out by redispersing 40 nm Au NPs in NaCl solutions with different concentrations. The 12 mM NaCl is proved to offer the best ionic strength that would be favorable to form a dense layer of 40 nm Au NPs. NaCl solution with higher concentration would introduce aggregation and lower concentration would lead to low binding efficiency of 40 nm Au NPs to the center particle.

Once we obtained the flower-like assemblies, single particle scattering studies were carried out to investigate the plasmonic coupling in the assemblies. As a control, single particle scattering measurements of a 40 nm Au NP and a 130 nm Au NP were conducted and the spectra were shown in Figure 2.4. The LSPR speaks of the 40 nm and 130 nm Au NPs are at 520 nm and 592 nm, respectively, corresponding well with previous studies.[41] It is worth noting that the signal to noise

ratio of the scattering spectrum of 40 nm Au NP is lower than that for the 130 nm Au NP, due to the small size of the NP.

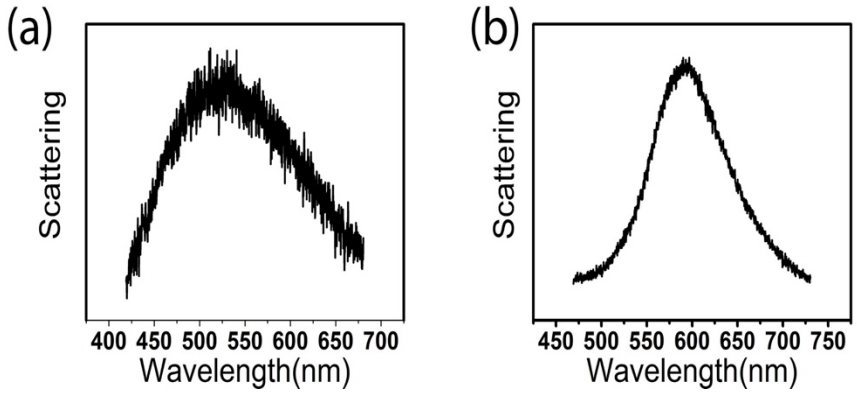

Figure 2.4. Single particle scattering spectra of (a) 40 nm Au NP and (b) 130 nm Au NP.

Similar measurements were performed on the flower-like assemblies. Figure 2.5(a) shows the representative single particle scattering spectra from six individual assemblies, respectively. From the assembled structures, instead of one well-resolved peak as for the single NPs, we observed two peaks, or sometimes a shoulder in addition to the main peak (black and pink curves in Figure 2.5(a). The wavelength of the main peaks or shoulders and the peak shape vary, likely due to the difference in the geometry of different assembled structures, as evident from the SEM images in Figure 2.2. In most cases, one peak (shoulder) is around 570 nm, and the other one is around 660 nm. Clearly, the new plasmon features arise due to the coupling between the NPs in assemblies.

2.4.2 Theoretical Modeling of Assembled Flower-like Nanostructures

To further understand the origin of the plasmon peaks of the assemblies, we carried out electrodynamic simulations using the discrete dipole approximation (DDA) method. From the

SEM images, we notice that the assembled flowered-like structures have different numbers of 40 nm Au NPs attaching to the 130 nm Au NP. On average, there are eight 40 nm Au NPs attached to one 130 nm Au NP. In addition, the 40 nm Au NPs were randomly distributed at the bottom of the 130 nm Au NP. To examine the different scenarios, in the calculations, we modeled the structure with one 130 nm Au sphere in the center, and 6, 8 or 10 of 40 nm Au NPs attached randomly around the center. The calculated spectra are plotted in Figure 2.5(b)-(d). The theory results agree well with the experimental observations, where two peaks are observed in the spectra. We notice a dramatic variation in the spectral shape of the spectra in Figure 2.5(b). And this variation become smaller in the spectra in Figure 2.5(c), and almost disappeared in the spectra in in Figure 2.5(d). Even though all of them have two peaks, in some spectra, the two peaks are clearly resolved; whereas in others, a shoulder appears in addition to the main peak. Same phenomenon was found in the experimental results. When the number of 40 nm Au NPs is increased to 10, there is less variation in the spectra as seen in Figure 2.5(d). This is because most of the space around the center 130 nm Au NP has been occupied by the 40 nm Au NPs. There is no much difference between the structures even though the 40 nm Au NPs were allowed to randomly move. One significant difference between Figure 2.5(b) and 5d is the consistent high intensity peak at the wavelength of 660 nm in Figure 2.5(d) and random alternation of the relative intensity between the peaks at wavelengths of 570 and 660 nm. This difference indicates that the peak at the wavelength of 660 nm is due to the strong coupling between the 130 and 40 nm particles while the peak at 570 nm is due to the weak coupling between the two sized particles. More

specifically, the peak at the wavelength of 660 nm is due to the coupling between two sized particles when they are arranged relatively

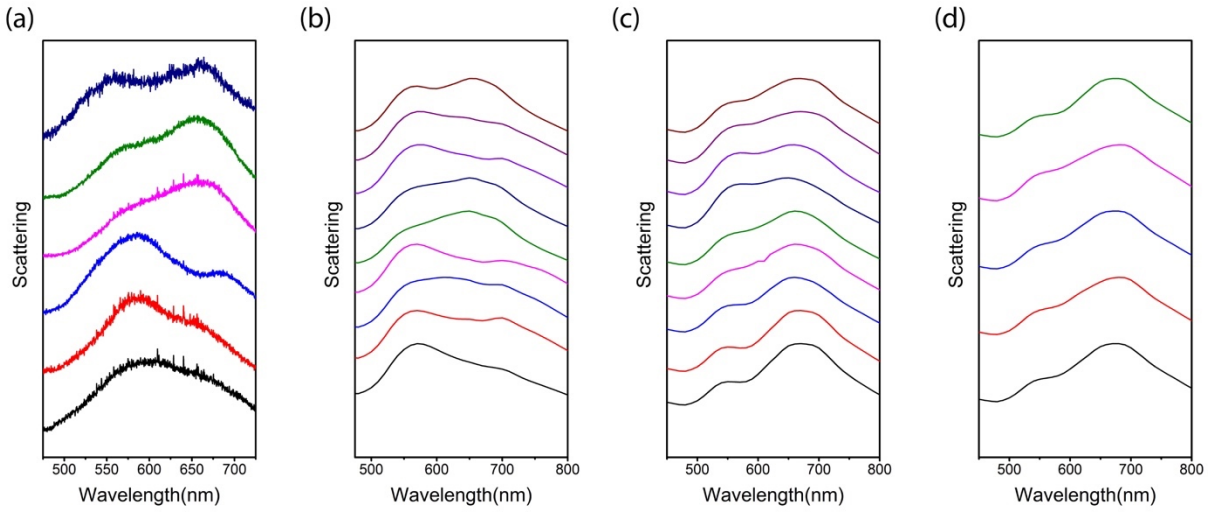

Figure 2.5. (a) Representative single particle scattering spectra of individual assembled structures. Simulated scattering spectra of assembled structures consisted of one 130 nm Au sphere in the center, with varying number of 40 nm Au spheres randomly attached to the center sphere: (b) six, (c) eight, and (d) ten.

parallel to the incident polarization direction, which is strong and red shifted from the single particle peak. The peak at the wavelength of 570 nm is the consequence of coupling when the two sized particles are arranged relatively perpendicular to the incident polarization direction. When more 40 nm particles are included in the structures, the strong coupling is dominant since the satellite particles occupy all different directions. When only 6 of the 40 nm particles are included, this strong coupling can only be observed at given conditions and the obtained spectra show a larger variation among different structures.

2.5 Conclusions

In this work, flower-like nanostructures were fabricated by self-assembly of 130 nm and 40 nm Au NPs. The structure has a 130 nm Au NP in the center, and varying number of 40 nm Au NPs attached to it. The LSPR of individual Au assemblies show two peaks, due to the plasmonic coupling between the NPs. Experimental and theoretical studies demonstrate that the coupling is dependent upon the number and arrangement of the 40 nm Au NPs around the center NP.

2.6 Acknowledgements

This work is supported by the National Science Foundation CAREER award (CHE 1554800). The electron microscopy imaging work was performed at the Biosciences Electron Microscopy Facility of the University of Connecticut.

2.7 References

1. K. L. Kelly, E. Coronado, L. L. Zhao and G. C. Schatz, *ChemInform*, 2003, **34**, 668-677.
2. U. Kreibig and M. Vollmer, *Optical properties of metal clusters*, Springer Science & Business Media, 2013.
3. S. Link and M. A. El-Sayed, *Annual review of physical chemistry*, 2003, **54**, 331-366.
4. P. Zijlstra and M. Orrit, *Reports on Progress in Physics*, 2011, **74**, 106401.
5. V. Giannini, A. I. Fernández-Domínguez, S. C. Heck and S. A. Maier, *Chemical reviews*, 2011, **111**, 3888-3912.
6. K. A. Willets and R. P. Van Duyne, *Annu. Rev. Phys. Chem.*, 2007, **58**, 267-297.
7. S. Eustis and M. A. El-Sayed, *Chem. Soc. Rev.*, 2006, **35**, 209-217.
8. R. Bardhan, N. K. Grady, J. R. Cole, A. Joshi and N. J. Halas, *ACS nano*, 2009, **3**, 744-752.
9. R. G. Freeman, K. C. Grabar, K. J. Allison and R. M. Bright, *Science*, 1995, **267**, 1629.
10. S. Kühn, U. Håkanson, L. Rogobete and V. Sandoghdar, *Physical Review Letters*, 2006, **97**, 017402.
11. J. F. Li, Y. F. Huang, Y. Ding, Z. L. Yang, S. B. Li, X. S. Zhou, F. R. Fan, W. Zhang, Z. Y. Zhou and B. Ren, *Nature*, 2010, **464**, 392-395.
12. D. Nepal, L. F. Drummy, S. Biswas, K. Park and R. A. Vaia, *ACS nano*, 2013, **7**, 9064-9074.
13. K. Sugawa, T. Tamura, H. Tahara, D. Yamaguchi, T. Akiyama, J. Otsuki, Y. Kusaka, N. Fukuda and H. Ushijima, *ACS Nano*, 2013, **7**, 9997-10010.

14. J. Zhao, X. Zhang, C. R. Yonzon, A. J. Haes and R. P. Van Duyne, *Nanomedicine*, 2006, **1**, 219-228.
15. M. Gellner, D. Steinigeweg, S. Ichilmann, M. Salehi, M. Schütz, K. Kömpe, M. Haase and S. Schlücker, *Small*, 2011, **7**, 3445-3451.
16. S. Grésillon, L. Aigouy, A. Boccara, J. Rivoal, X. Quelin, C. Desmarest, P. Gadenne, V. Shubin, A. Sarychev and V. M. Shalaev, *Physical Review Letters*, 1999, **82**, 4520.
17. W. Li, P. H. Camargo, X. Lu and Y. Xia, *Nano Letters*, 2008, **9**, 485-490.
18. S. Prokes, O. Glembocki, R. Rendell and M. Ancona, *Enhanced plasmon coupling in crossed dielectric/metal nanowire composite geometries and applications to surface-enhanced Raman spectroscopy*, DTIC Document, 2007.
19. L. Polavarapu and Q.-H. Xu, *Langmuir*, 2008, **24**, 10608-10611.
20. S. Borsley, S. Flook and E. R. Kay, *Chemical Communications*, 2015, **51**, 7812-7815.
21. M. P. Busson, B. Rolly, B. Stout, N. Bonod, E. Larquet, A. Polman and S. Bidault, *Nano letters*, 2011, **11**, 5060-5065.
22. J. A. Fan, C. Wu, K. Bao, J. Bao, R. Bardhan, N. J. Halas, V. N. Manoharan, P. Nordlander, G. Shvets and F. Capasso, *science*, 2010, **328**, 1135-1138.
23. V. V. Thacker, L. O. Herrmann, D. O. Sigle, T. Zhang, T. Liedl, J. J. Baumberg and U. F. Keyser, *Nature Communications*, 2014, **5**.
24. J. H. Yoon, J. Lim and S. Yoon, *ACS nano*, 2012, **6**, 7199-7208.
25. V. Suresh, S. Madapusi and S. Krishnamoorthy, *ACS Nano*, 2013, **7**, 7513-7523.
26. S. J. Barrow, X. Wei, J. S. Baldauf, A. M. Funston and P. Mulvaney, *Nature communications*, 2012, **3**, 1275.
27. L. V. Brown, H. Sobhani, J. B. Lassiter, P. Nordlander and N. J. Halas, *ACS nano*, 2010, **4**, 819-832.
28. J. A. Jenkins, Y. Zhou, S. Thota, X. Tian, X. Zhao, S. Zou and J. Zhao, *J. Phys. Chem. C*, 2014, **118**, 26276-26283.
29. P. Nordlander, C. Oubre, E. Prodan, K. Li and M. Stockman, *Nano letters*, 2004, **4**, 899-903.
30. X. Tian, Y. Zhou, S. Thota, S. Zou and J. Zhao, *J. Phys. Chem. C*, 2014, **118**, 13801-13808.
31. A. S. Urban, X. Shen, Y. Wang, N. Large, H. Wang, M. W. Knight, P. Nordlander, H. Chen and N. J. Halas, *Nano Letters*, 2013, **13**, 4399-4403.
32. G. Frens, *Nature*, 1973, **241**, 20-22.
33. X. D. Tian, B. J. Liu, J. F. Li, Z. L. Yang, B. Ren and Z. Q. Tian, *J. Raman Spectrosc.*, 2013, **44**, 994-998.
34. Y. Wang, G. Chen, M. Yang, G. Silber, S. Xing, L. H. Tan, F. Wang, Y. Feng, X. Liu and S. Li, *Nature communications*, 2010, **1**, 87.
35. B. T. Draine, *The Astrophysical Journal*, 1988, **333**, 848-872.
36. E. D. Palik, *Handbook of optical constants of solids*, Academic press, 1998.
37. J. C. Love, L. A. Estroff, J. K. Kriebel, R. G. Nuzzo and G. M. Whitesides, *Chemical reviews*, 2005, **105**, 1103-1170.
38. A. M. E. Badawy, T. P. Luxton, R. G. Silva, K. G. Scheckel, M. T. Suidan and T. M. Tolaymat, *Environmental science & technology*, 2010, **44**, 1260-1266.
39. S. Behrens, M. Borkovec and P. Schurtenberger, *Langmuir*, 1998, **14**, 1951-1954.
40. R. A. French, A. R. Jacobson, B. Kim, S. L. Isley, R. L. Penn and P. C. Baveye, *Environmental Science & Technology*, 2009, **43**, 1354-1359.
41. G. Mie, *Annalen der physik*, 1908, **330**, 377-445.

Chapter Three : Tuning the Valency of Heterogeneous Au-Silica Nanostructure via Controlled Ostwald Ripening Process

3.1 Abstract

Morphology control of interfaced heterogeneous nanostructure composed of two different materials is critical for achieving desired properties of the nanostructures. With heterogeneous Au-silica system as a case study, we explored the reaction mechanism that controlled the number of overgrown silica domains on Au nanoparticle seeds. We discovered in our system that three factors dominated the overgrowth of silica on gold surface: a) gold core size, b) wettability of the surface of the Au core (controlled by the amount of ligands), and c) reaction kinetics of hydrolysis of the silica precursor. In particular, the latter two played distinct roles in triggering different extent of Ostwald ripening and contributed to the symmetry breaking of the morphology of the final product from core-shell to core-satellite. Specifically, polyacrylic acid ligand decreased the local wettability of the Au nanoparticle surface and resulted in discrete domain growth. Adequate wetting introduced by 3-mercaptopropionic acid/cetyltrimethylammonium ligands lowered the Au-silica interface energy and stabilized the silica domain in the later growth stage. After the initial nucleation process, depending on the surface wettability and reaction kinetics, Ostwald ripening of silica was triggered by the depletion field and certain number of domains survived after the ripening process. By tuning the core size, surface wettability and reaction kinetics, Au-silica heterogeneous structure with desired number of silica domains can be achieved. Since Ostwald

ripening happens in many systems including metal, metal oxide and semiconductors, our findings can provide guidance to the synthesis of a wide span of heterogeneous structures.

3.2 Introduction

Development of wet-chemical strategies to synthesize interfaced heterogeneous nanoparticles with various morphologies has been highly challenging but also rewarding because of the unique properties offered by the heterogeneous nanoparticles.[1-3] Interfaced heterogeneous nanostructures composed of two different materials preserve the chemical and physical properties of the individual substances and meanwhile allow new properties to emerge from the interaction of the interfaced components.[4, 5] With the recent progress in the fabrication of hetero-structures composed of metal, semiconductor and metal oxides, great advancements have been achieved in catalysis, energy conversion, imaging, drug delivery etc. [6-19]

A common method to fabricate heterogeneous structure is to employ pre-synthesized single-component nanoparticles as seeds, and to overgrow the second component of different composition on the seeds. The morphology of the heterogeneous structures resulted from this method significantly affect the property of the structures. Therefore, it is critical to control the number of the overgrown domains on the seeds. If the seed nanoparticles are considered as artificial atoms,[20, 21] interfaced heterogeneous structure can be considered as artificial molecules.[22] The number of the overgrown domains is then analogous to the valency of atoms. Unlike atoms however, the valency of nanoparticles is not an intrinsic property of the nanoparticle. Instead, it is often determined by the crystalline/amorphous nature of the two components as well as various synthetic parameters.[23] The sophistication of growing heterogeneous structure with controlled valency derives from the difficulty in manipulating the following factors: affinity between the core and overgrown materials (wettability), growth kinetics and thermodynamics of the overgrowth of

the second material. [6, 24-26] So far, a number of methods have been developed to synthesize interfaced heterogeneous structures, including: soft template, hard template, facet-specific growth and controlled wettability. [11, 23, 27-34] Among all these methods, controlled wettability offers the flexibility of tuning the valency of nanoparticles simply by tuning the type/amount of surface ligands. It has been demonstrated that different degree of surface wetting determines the overgrowth of one material on another.[23] By tailoring the surface wettability from greatly wetted to adequately wetted, one can control the synthesized heterogeneous structure from core-shell to core satellite. However, controlling the valency of the core-satellite hetero-structure still remains a challenge and the mechanism that determines the valency still needs to be explored.

Here we use Au-silica heterogeneous structure to demonstrate how to achieve synthetic control of the valency. We selected Au nanospheres as seeds because we are interested in exploring how to induce and control anisotropic growth on isotropic particles. It has been demonstrated with anisotropic Au nanorods that the uneven distribution of cetyltrimethylammonium bromide at the ends/sides caused by the difference in curvature could induce site-selective silica growth.[28, 32] However, with a homogeneous surface of the Au nanosphere,, we found that Ostwald ripening played a critical role in tuning the valency of Au-silica nanostructures. Ostwald ripening is a well-studied mechanism to explain coarsening effect in colloidal synthesis of various materials including metal, polymer and inorganic oxides.[35-37] In this thermodynamically driven process, smaller particles with higher surface energy are sacrificed and contribute to the growth of bigger particles.[38, 39] Ostwald ripening is important in defocusing the size distribution when the nanoparticles experience a monomer depleted zone.[17, 40, 41] In this case, the particles below the critical size would dissolve and contribute to the growth of particles that are above the critical size. Specifically in the ripening process of silica particles, the particles or surfaces with higher surface

energy would dissolve via cleavage of siloxane bridges and the released silicic acid that would contribute to the growth of bigger particles or more passivated surfaces.[42-46] We observed similar phenomenon in the early stage of Au-silica heterogeneous structure where some of the silica domains would dissolve and the others continued to grow, suggesting that Ostwald ripening was a key process that determined the valency of Au-silica hetero-structure.

In this work, using Au-silica heterogeneous structure as a case study, we investigate how to fine tune the Ostwald ripening process to control the valency of the Au-silica hetero-structure. Specifically, Au nanopsheres (NS) were used as seeds and silica domains of varying number and size were overgrown on the Au NS. The growth process was monitored by measuring transmission electron microscopy (TEM) images of samples acquired at different reaction times. When changing the surface ligands of the Au NS, we found that the 3-mercaptopropionic acid (MPA)/cetyltrimethylammonium cation (CTA+) offers adequate wetting and resulted in a continuous silica shell around Au NS surface, while polyacrylic acid (PAA) lowers the local surface wettability and resulted in growth of discrete silica domains in the nucleation stage. Then the system entered a diffusion controlled growth process with the silane monomers being depleted during the nucleation stage. The silica shell and the silica domains would dissolve in the monomer scarce field and only certain number of silica domains would survive after the depletion process (Ostwald ripening). By tuning the Au NS size, surface wettability of Au NS and reaction kinetics of hydrolysis, the Ostwald ripening process could be controlled and desired valency was achieved in the Au NS-silica hetero-structures.

3.3 Experimental Methods

3.3.1 Chemicals and Materials

Gold (III) chloride trihydrate (≥99.9% trace metals basis), sodium boronhydride, L-ascorbic acid, hydroxylamine hydrochloride, hexadecyltrimethylammonium bromide (CTAB), cetyltrimethylammonium chloride solution (CTAC) (25% in water), 2-propanol (ACS reagent, ≥99%), poly (acrylic acid) (PAA) (average M_w=1800), 3-mercaptopropionic acid (MPA) (≥99%,), tetraethyl orthosilicate(TEOS) (≥99.0%) and tert-butanol were purchased from Sigma Aldrich. Sodium citrate dehydrate was purchased from Fisher Scientific. Ammonium hydroxide (28.0-30.0%) was purchased from J. T. Baker. All chemicals were used as received.

3.3.2 Preparation of CTAC capped Au NS

Au NS stabilized by CTAC ligand was synthesized by a seed mediated method developed by Xia's group.[47] First, Au clusters were synthesized by reducing $HAuCl_4$ with $NaBH_4$. An aqueous solution of CTAB (100 mM, 7.5 mL) was mixed with 2.5 mL of $HAuCl_4$ solution (0.0254 M). 0.6 mL of $NaBH_4$ solution (10 mM) was then immediately added to the mixture. After 2 minutes of mixing on an orbital shaker, the reaction was left undisturbed for 3 hours.

The Au clusters were further used to synthesize 14 nm Au NS. 2 mL $HAuCl_4$ solution (0.0254 M) was injected to a mixture of previously synthesized Au clusters with 2 mL of CTAC solution (0.02 M) and 1.5 mL of ascorbic acid (1 mM). After the reaction continued for 15 minutes, the solution was centrifuged and the precipitate of 14 nm Au NS was redispered in 1 mL of CTAC solution (0.02 M).

40 nm Au NS was synthesized with the as-prepared 14 nm Au seed. 2 mL of $HAuCl_4$ solution (0.5 mM) was slowly injected into the solution that contains 1.74 mL of DI water, 0.265

mL of CTAC solution (25% in water), 130 μL of ascorbic acid (10 mM) and 20 μL of the 14 nm seed with an injection rate of 2 mL/hr. 15 minutes after the injection was completed, the mixture was centrifuged and re-dispersed in 1 mL of CTAC solution (0.02 M). 65 nm Au NS was synthesized with 10 μL of the 14 nm Au seed while all the other conditions remained the same. To grow bigger Au NS, 40 nm Au NS were used as seeds. 81 nm, 117 nm and 146 nm Au NS were prepared with 100 μL, 50 μL and 20 μL of the 40 nm Au seeds, respectively. All the other experimental conditions were maintained the same as that for the 40 nm Au NS synthesis.

3.3.3 Preparation of citrate capped Au NS

We adopted Frens' method to synthesize the citrate capped Au NS as a comparison to the CTAC capped Au NS.[48] To synthesize 40 nm citrate capped Au NSs, 99 mL of DI water was added into a 250 mL flask, followed by addition of 1.06 mL of $HAuCl_4$ solution (0.0254 M). The mixture was stirred and heated on a hot plate with the temperature set at 160 ℃. 1.0 mL of the sodium citrate solution (0.0388 M in DI water) was immediately added to the flask after the solution boiled. The solution was heated for another 15 minutes and then cooled to room temperature.

120 nm citrate capped Au NSs was prepared with a seed mediated method at room temperature reported by Tian et.al. [49] 4 mL of the citrate capped 40 nm Au NS was added to 52 mL of distilled water, followed by addition of 900 μL of sodium citrate solution (0.0388 M) and 0.88 mL of HAuCl4 (0.0254 M). Finally, 1.4 mL of hydroxylamine hydrochloride solution (0.0101 M) was added drop by drop in 5 minutes and the reaction solution was stirred for 2 hours.

Preparation of Au-silica heterostructures

We adopted and modified the method developed by Chen et.al to synthesize Au-silica heterogeneous structures.[50] 3 mL of the as prepared Au NS (40-146 nm) solution were concentrated to 0.5 mL by centrifugation. The concentrated Au NS solution was added to 2.5 mL

of 2-proponal or tert-butanol. 20 μL of 3-mercaptopopionic acid (5 mM，50 mM or 250 mM in ethanol) and 20 μL of polyacrylic acid (0.645 mM in water) were then added to the solution. The mixture was allowed to stir for 30 minutes. 600 μL of tetraethyl orthosilicate (8.9 mM, 20.7 mM or 62.3 mM in ethanol) and 90 μL of ammonium hydroxide were added afterwards. The reaction was kept under room temperature for 2 hours.

3.3.4 Transmission Electron Microscopy(TEM) Imaging

Au and Au-SiO_2 nanoparticles (NPs) were transferred to a carbon-coated TEM grid (Electron Microscopy Sciences) for TEM imaging. FEI Tecnai G2 Spirit BioTWIN was used to acquire the TEM images under the acceleration voltage of 80 kV.

3.3.5 Scanning Electron Microscopy (SEM) Imaging.

To prepare the SEM sample, 10 μl of the sample was drop casted to a glass slide and left in air to dry. The glass slide was then coated with gold with a sputter coater to induce conductivity. FEI Nova NanoSEM 450 was used to acquire the SEM images. The SEM images provided a better 3D view with the top silica domains clearly visible. However, part of the silica domains that sit at the bottom was still unrevealed. As a result, determination of the valency based on the SEM images became very difficult and unworthy. (Figure 3.1)

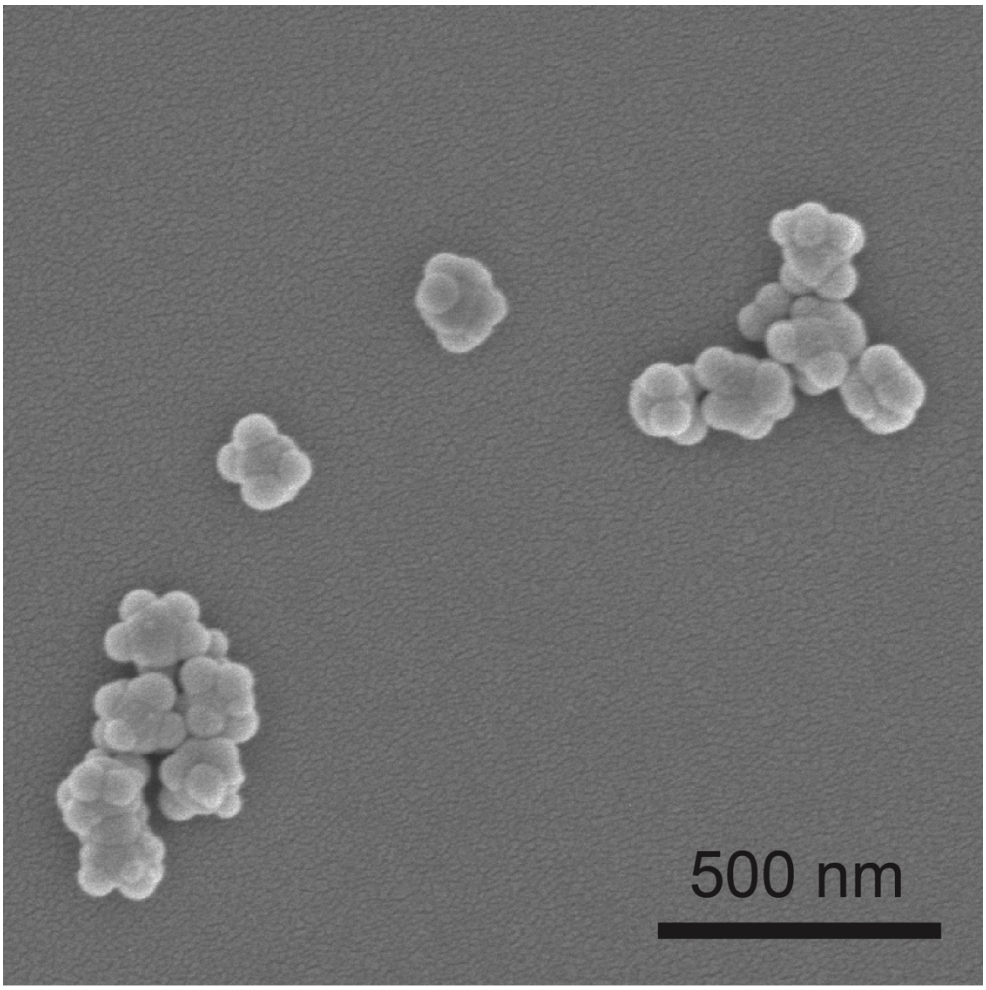
500 nm

Figure 3.1. SEM image of 117 nm Au-silica heterogeneous structure with 20.7 mM TEOS.

3.4 Results and Discussion

3.4.1 Core-size Dependent Valency

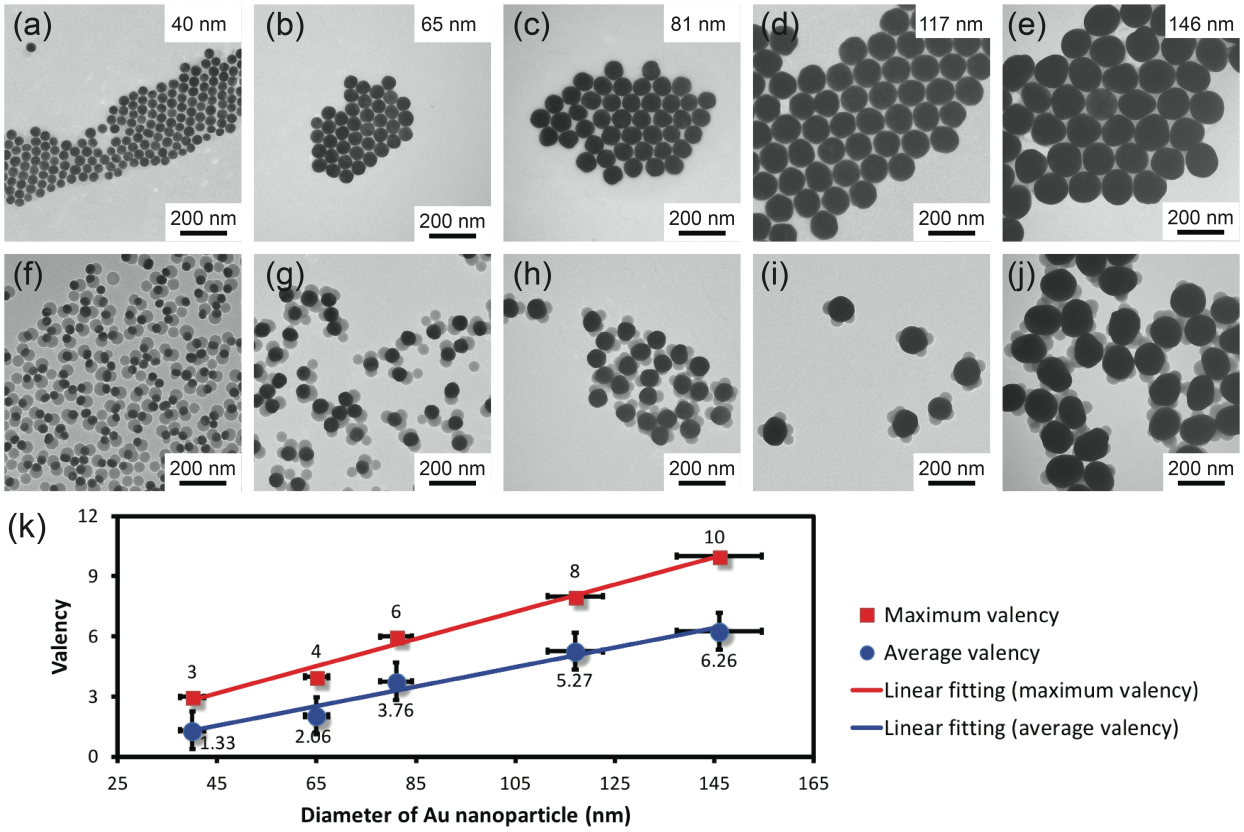

Figure 3.2. TEM images of Au NSs with diameters of a) 40 nm, b) 65 nm, c) 81 nm, d) 117 nm, e) 146 nm; f-j), the corresponding heterogeneous Au-silica structures synthesized using the Au seeds under the same conditions; k), plot of the valency versus the diameter of Au NS.

Heterogeneous Au-silica structures with various Au seed sizes were synthesized under the same reaction conditions. First, the CTAC capped Au NS was washed twice and transferred to 2-propanol solution, followed by addition of PAA and MPA. The solution was stirred for 30 minutes

to ensure sufficient ligand exchange. The PAA and MPA co-functionalized Au NS showed more negative zeta potential of -31.2 mV compared of that of MPA functionalized Au nanosphere, which was at -27.0 mV. Then, TEOS and ammonia were added to start growth of silica. After 2 hours of reaction, the synthesized heterogeneous Au-silica structures were centrifuged two times with distilled water and examined with TEM (Figure 3.2). Since TEM is only able to view the silica domains on the side due to the darker contrast of Au covering the silica domains that were located either on the top or at the bottom, we attempted to image the Au-silica with scanning electron microscopy (Figure 3.1), which could allow us to get a better 3D view of the Au-silica structures. However, we were still unable to determine the number of silica domains underneath the Au NS. For the consistency of the analysis, we chose to examine the silica domains on the cross section of the Au NS based on the TEM images. The "valency" in the following discussion refers to the number of silica domains determined from TEM. Although the valency of the Au NS considering the entire surface may be different, the findings and conclusions on the factors that control the valency of the Au NS still hold. Note the valency is different with surface coverage. When increasing the reaction time, the valency remained the same, but the surface coverage increased. So, the valency here only refers to the number of domains but is irrelevant with the size of the domains. Figure 3.2f shows that the 40 nm Au NS was able to preserve 1 to 3 silica domains on the side. The average valency was determined to be 1.33 by averaging the valency of ~100 nanostructures, with the valency of 1 as the dominant population. As the diameter of the Au NS increased, both the average and maximum valency of the Au NS increased. Figure 3.2k shows both the average and maximum valency of the Au NS increased linearly with its diameter. When the size of Au NS increases, an immediate consequence is that the surface area of the NS increases. If we make an analogy between the valency of the Au NS and the number of available atomic

orbitals in atoms for bonding, it is evident that higher surface area of the Au NSs increases their valency. In another word, with a bigger surface area, the Au NS sustains a greater capability of combining with silica domains. Similar phenomenon was observed by Lal et.al in heterogeneous polystyrene-silica nanostructure, i.e. when the size of the polystyrene nanoparticle increased, the number of silica domains also increased.[26] However, unlike atoms, the valency of Au NS varied from one particle to another, even though the sizes of the particles were similar. This variation in the valency implies that the size of the Au NS is not the only factor that determines the valency of the Au NS.

3.4.2 Proposed Au-silica Growth Mechanism

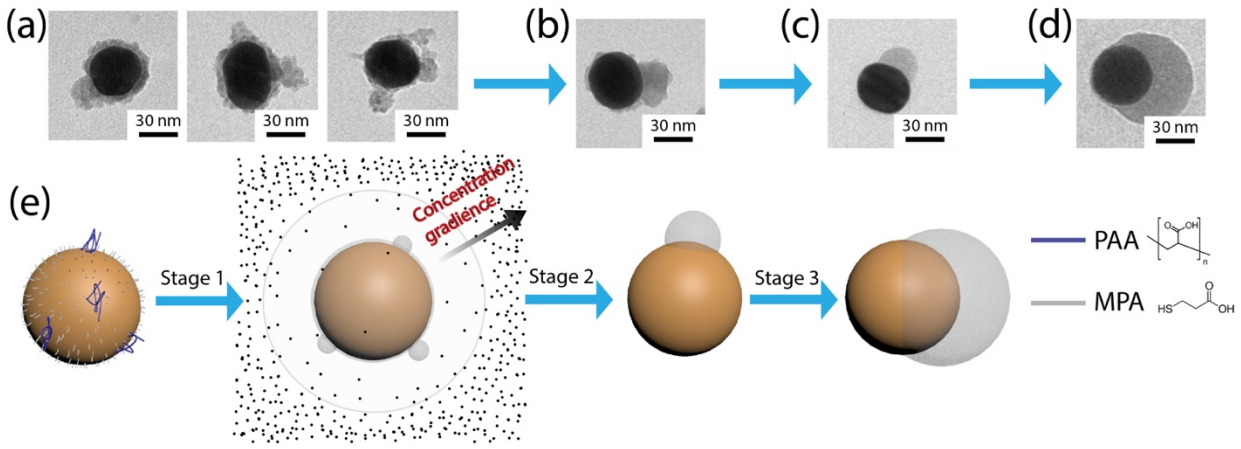

Figure 3.3. TEM images of intermediate states during the synthesis of Janus Au-silica using 40 nm citrate stabilized Au NS and with 8.9 mM TEOS solution. a) 10 minutes, b) 30 minutes, c) 1 hour, d) 4 hours, e) schematic illustration of the growth mechanism.

From the previous section, the variation of valency between particles that share similar diameter indicates there are other factors that influence the valency among particles during growth. Therefore, we investigated the morphology transformation of the Au-silica structures during

growth to understand the growth mechanism. We used the citrate stabilized 40 nm Au NS as the seeds for heterogeneous nucleation of silica since it had the highest yield of heterogeneous Au-silica structure with a valency of 1 (97%) (Figure 3.4). After the addition of the two ligands (MPA and PAA), TEOS and ammonia were added and initiated St*ö*ber synthesis[51]. As the reaction continued for 10 minutes, a continuous layer and a few silica domains formed on the Au NS surface (Figure 3.3a). After 30 minutes, only one silica domain survived but a coarse layer of silica was clearly visible, indicating that dissolution of silica layer was taking place (Figure 3.3b). After one hour of reaction, the silica layer completely dissolved and only one silica domain was preserved on the gold surface. As the reaction continued for 4 hours, an Au-silica hetero-dimer was formed. The TEM observations revealed several processes that occurred during the growth, including condensation of silane monomers to form silica shell and domains, followed by dissolution of silica shell and domains and finally growth of a single domain. Based on these observations, we proposed the growth mechanism in Figure 3.3e. In the synthesis of heterogeneous Au-silica structure, two ligands, MPA and PAA, played critical roles in the growth of silica on gold nanoparticle surface. The mechanism of heterogeneous growth of silica is difficult to ascertain unless one decodes how the two ligands distribute on the nanoparticle surface. However, the relative distribution of the two ligands over a sub 100 nm region is very challenging to resolve with the existing technologies. Even through direct evidence is still lacking, based on the TEM images of the Au-silica hetero-structure (average valency: 1.02, Figure 3.4) taken out at different reaction times imply the distribution of the two ligands (Figure 3.3a-d). Firstly, at the beginning of the reaction, mixed ligands of MPA and PAA were introduced to the citrate capped Au NSs. Since the thiol group on the MPA has high binding affinity to Au NSs due to strong thiol-gold interaction, MPA would ligand exchange with the citrate ligands, at least in part. The second ligand

PAA has much weaker interaction with gold through electrostatic force compared with thiol-gold interaction. With a much lower concentration of PAA in the solution compared to that of MPA (0.1 μM of 4-MPAA and 0.0129 μM of PAA), much fewer number of PAA would bind to the Au NS surface. We proposed a model of ligand distribution as shown in Figure 3.3i, i.e. MPA covered most of the surface of the Au NS with a few PAA randomly distributed around the NS. After TEOS and ammonia were added to the solution, the carboxylic groups of MPA could react with the silane monomer and initiate the silica growth. Figure 3.3a shows that a complete silica layer formed on the Au NS after the reaction continued for 10 minutes. Besides the continuous silica layer, a few silica domains were clearly visible on the surface as well. The origin of these discrete silica domains was attributed to the nucleation of silica around the sparse PAA ligands on the Au NS surface. MPA can provide adequate wetting to initiate heterogeneous nucleation of a silica shell on Au NS surface. In a control experiment when MPA alone was added to the Au NS solution while other reaction conditions remained the same, a uniform silica shell formed on the Au NS surface (Figure 3.5). However, when PAA was also added, under a basic condition (pH≈8), the carboxylic groups on PAA deprotonated and created electrostatic repulsion that hindered the condensation of silane monomers. As a result, PAA decreased the local wettability and resulted in heterogeneous nucleation of discrete silica domains. Upon the addition of TEOS and NH_3, TEOS was hydrolyzed and produced silane monomers. Once the concentration of silane monomers exceeded the minimum concentration required for heterogeneous nucleation, silica started to nucleate on both MPA and PAA without preference. This is denoted as stage one: nucleation of silica on MPA and PAA without preference due to the concentration buildup of the silane monomers (Figure 3.3i). After 30 minutes, the silica layer and some of the silica domains dissolved and only one silica domain survived (Figure 3.3b). This dissolution process and preferred growth

of a single silica domain is attributed as Ostwald ripening process, where the bigger particles consume the smaller particles to reduce surface energy. We believe this strongly indicates the existence of a monomer scarce field that triggered Ostwald ripening process, as suggested by other synthetic or theoretical works.[52-55] During the nucleation process, the formation of silica consumed the silane monomers and created a monomer scarce field around the Au NS. This scarce field is also considered as a depletion zone.

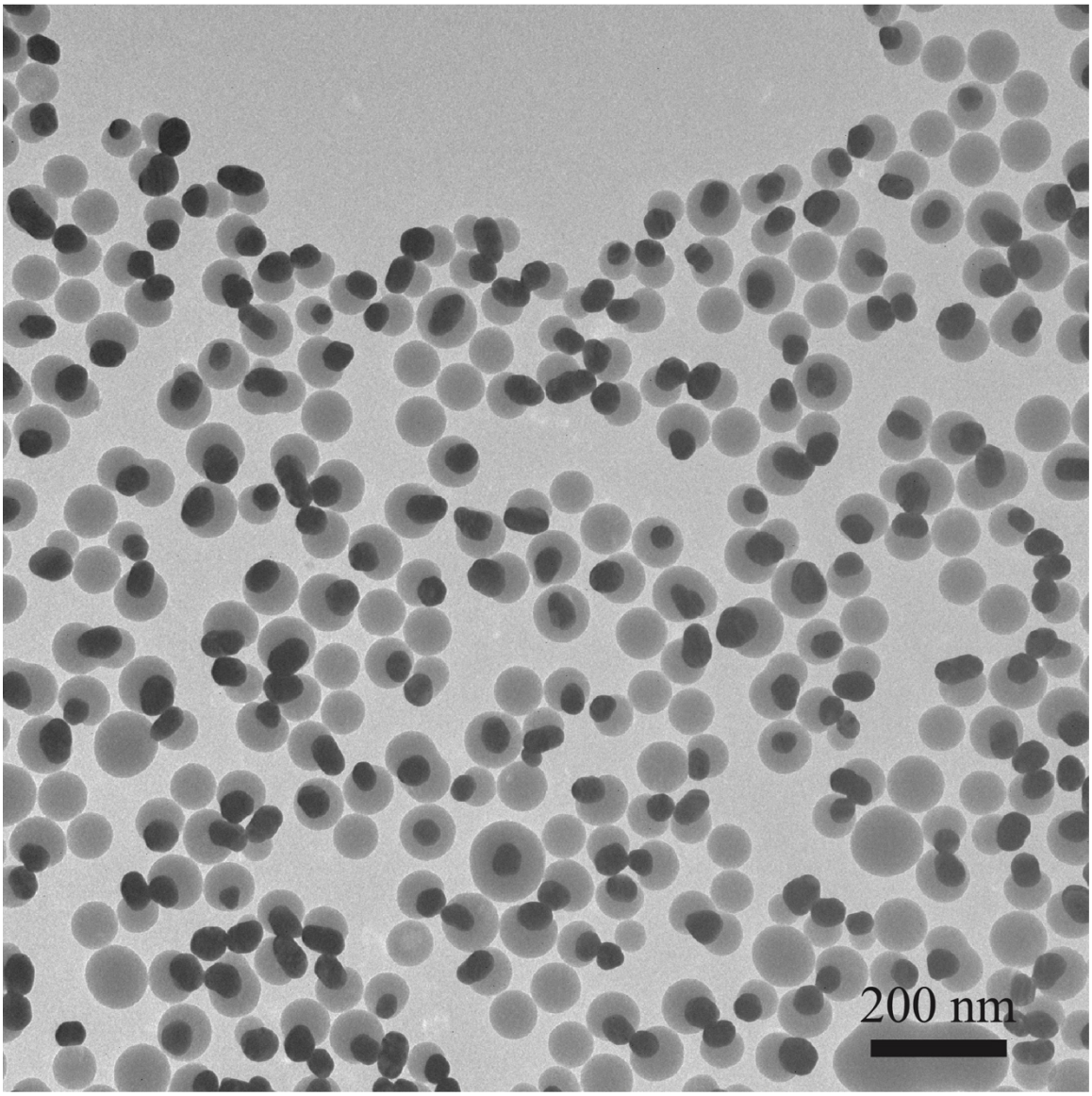

Figure 3.4. Large-area TEM image of 40 nm citrate stabilized Au-silica Janus structure showing 97% of the particles have a valency of 1.

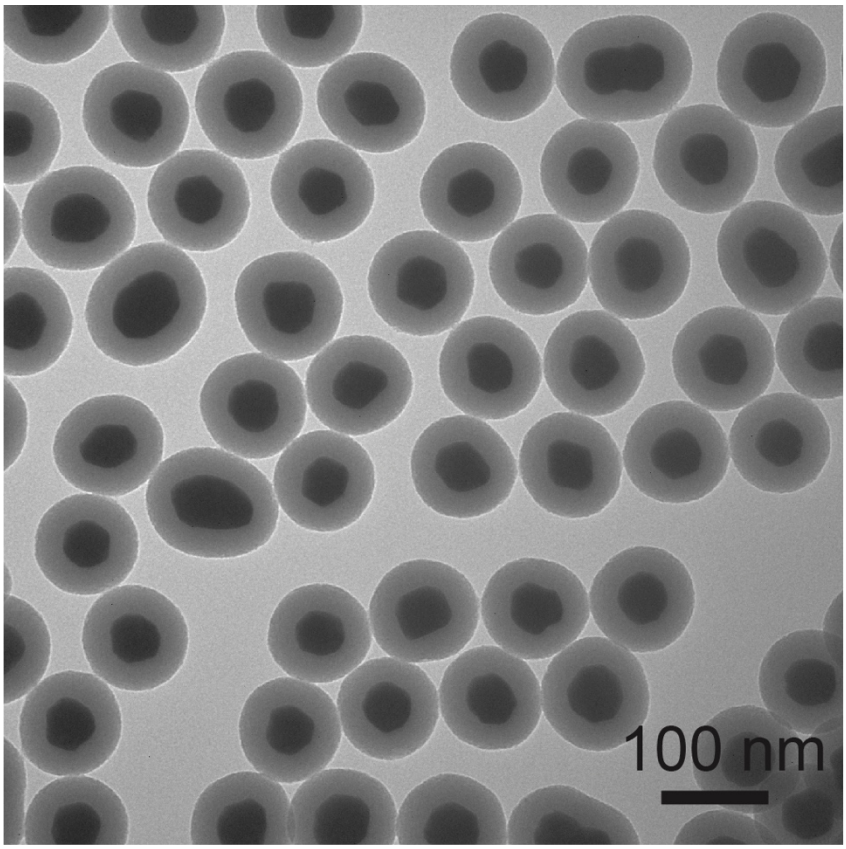

Figure 3.5. TEM image of 40 nm citrate stabilized Au@silica core@shell structure synthesized with MPA only as the ligand.

In nucleation the particle has to be bigger than a certain size to be stable.[56, 57] This size is recognized as the critical size[58], which is expressed by the equation below:

$R_c = \frac{2\gamma v}{k_B T \ln S}$ Equation 3.1

In equation 1, γ is the surface energy, T is the temperature, k_B is Boltzmann's constant, S is the supersaturation of the solution S and v is the molar volume. In the depleted field, due to the decreased concentration of silane monomers, the critical size increased and led to redistribution of the silica through cleavage of siloxane bridges and re-condensation of the silane monomers to decrease the free energy of the system. The surface tension on the interface between the thin layer and the gold surface made the silica layer less thermodynamically favorable compared with the discrete silica domains. Therefore, the silica layer dissolved completely overtime and contributed to the growth of the survived silica domain. After the ripening process, the system entered the last stage: growth of silica domain. In this stage, the survived silica domain continued to grow in size and the valency of the Au NS remained constant. It can be concluded that the domain growth was due to the decreased local wettability, but the ripening process determined the number of survived domains (valency).

3.4.3 Effect of Wettability on Valency

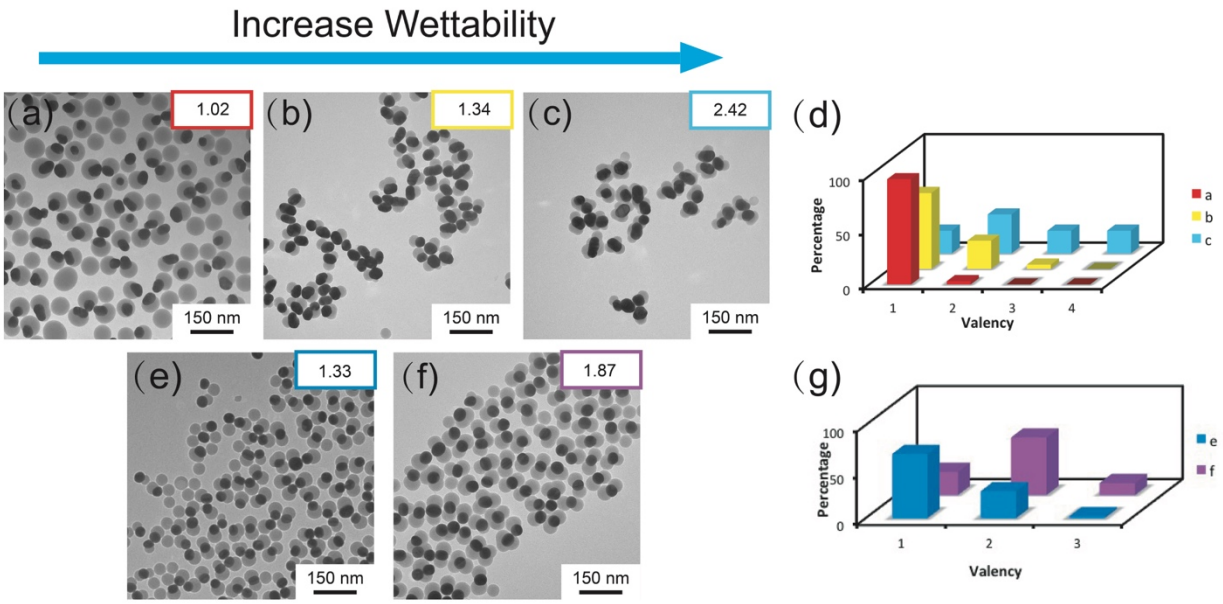

Figure 3.6. TEM images of 40 nm citrate stabilized Au-silica heterogeneous structure synthesized with different concentrations of MPA added, a) 0.005 M, b) 0.05 M, c) 0.25 M, d) distribution of valency of the above three samples, TEM images of 40 nm CTAC stabilized Au-silica heterogeneous structure synthesized with Au NS that were e) purified by centrifugation for 2 times, f) 1 time, g) distribution of valency of the above two samples.

In the section above, we proposed that the domain growth was due to the decreased local wettability caused by PAA, however, why certain number of silica domains survived after the Ostwald ripening process remains unknown. Interestingly, we found that the number of silica domains that could survive after ripening is closely related to the degree of surface wettability. When we use Au NS of similar sizes (~40 nm) but capped with different ligands (citrate or CTAC) to synthesize the Au-silica heterogeneous structure, the CTAC capped Au NS would always lead to a greater valency (Table 1). Moreover, when CTAC capped Au NS was used as seeds to grow the Au-silica heterogeneous structure, we discovered that the purification process of Au NSs

Table 1. Valency of Au-silica heterogeneous structures synthesized with 40 nm or 120 nm Au that are stabilized with citrate/CTAC.

Citrate	Average Valency	CTAC	Average Valency
40 nm	1.02	40 nm	1.33
120 nm	2.41	117 nm	5.20

affected the valency. When the 2 mL of Au NS solution was centrifuged once and redispersed in 0.5 mL of distilled water (further Au-silica heterogeneous synthesis were carried out under the same conditions as the citrate stabilized Au-silica heterogeneous structure), the resulting valency is 1.33, while centrifuging twice would result in a valency of 1.87 (Figure 3.6e-g). The maximum valence also shoed increase from Further washing would cause aggregation of Au NS (Figure 3.7). We believe this varied valency is due to the incomplete removal of excess CTAC ligands in the solution that could interfere with the ligand exchange process. In addition, the surface wettability of the Au NS would be altered resulting from the incomplete removal of CTAC ligands. CTA^+ is a good template for silica growth due to its positive charge.[28] Typically, CTAC forms a double layer around the Au NSs.[59] The centrifugation process would possibly remove part of the second layer of CTAC on the Au NS surface and also affect the amount of CTAC in the solution. One time of centrifugation would preserve more CTAC ligands and help increase the wettability of the Au NS surface. The increased wettability would lower the surface energy of the silica domains and affect the Ostwald ripening process. Therefore, higher valency was observed for the Au-silica structures synthesized with CTAC capped Au NS with one-time purification.

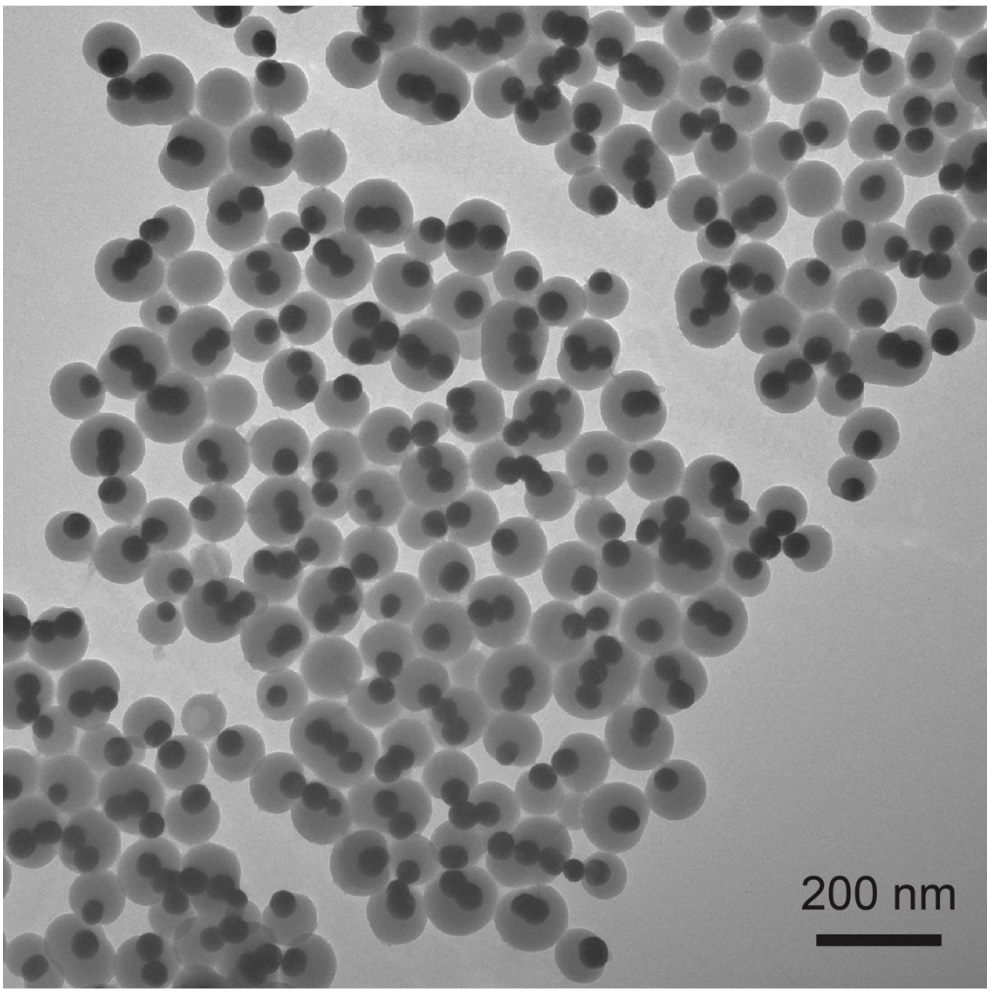

Figure 3.7. TEM image of 40 nm CTAC stabilized Au NS-silica heterogeneous structure synthesized with Au NS that was centrifuged for 3 times. A lot of the Au NS clearly aggregated before the silica growth.

In heterogeneous nucleation, wetting on the surface greatly lowers the energy barrier; therefore, the heterogeneous nucleation occurs at a much lower concentration of atoms or monomers with a higher degree of wetting. The free energy required for heterogeneous nucleation[60] can be expressed as:

$$\Delta G^*_{het} = \frac{1}{4}(2 + cos\theta)(1 - cos\theta)^2 \Delta G^*_{hom} \quad \text{Equation 3.2}$$

Here θ represents the extent of wettability. With greater wettability, the ΔG^*_{het} decreased and promoted the stability of the nucleated silica domains, which also means that at stage 2, the Au-silica heterogeneous structure could sustain a monomer scarce field with sacrificing fewer silica domains to reach equilibrium. Greater wettability helped lower the surface energy of silica domains. Thus, Ostwald ripening would be hindered and a greater number of silica domains can be preserved. This is also in agreement with Berg et.al's findings about silica-Cu core-satellite structure.[61] They discovered that the modification of silica surface with amine group would hinder the Ostwald ripening of Cu domains.

Varying the amount of MPA for the citrate capped Au NSs can also control surface wettability of the Au NSs. Since citrate interacts with Au through electrostatic interaction, they can easily be exchanged with MPA during ligand exchange process. In addition, because citrate provides no surface wettability for silica growth, the wettability of the citrate capped Au NS can be controlled by changing the amount of MPA added in the citrate-stabilized Au-silica heterogeneous structure synthesis. To do that, citrate capped Au NSs were mixed with MPA and PAA, where the concentration of MPA was varied to 0.005 M, 0.05 M and 0.25 M while the concentration of PAA was maintained at 0.645 mM. As we increased the concentration of MPA from 0.005 M to 0.05 M (Figure 3.6a-b), the average valency increased from 1.02 to 1.34, while the maximum valency increased from 2 to 3 (Figure 3.6d). As we further increased the concentration of MPA to 0.25 M, the average valency increased to 2.42 while the maximum valency increased to 4 (Figure 3.6c, d). From these results, we concluded that valency of Au NS could be easily tuned by tuning surface wettability as valency increased with increased wettability.

3.4.4 Effect of Reaction Kinetics on Valency

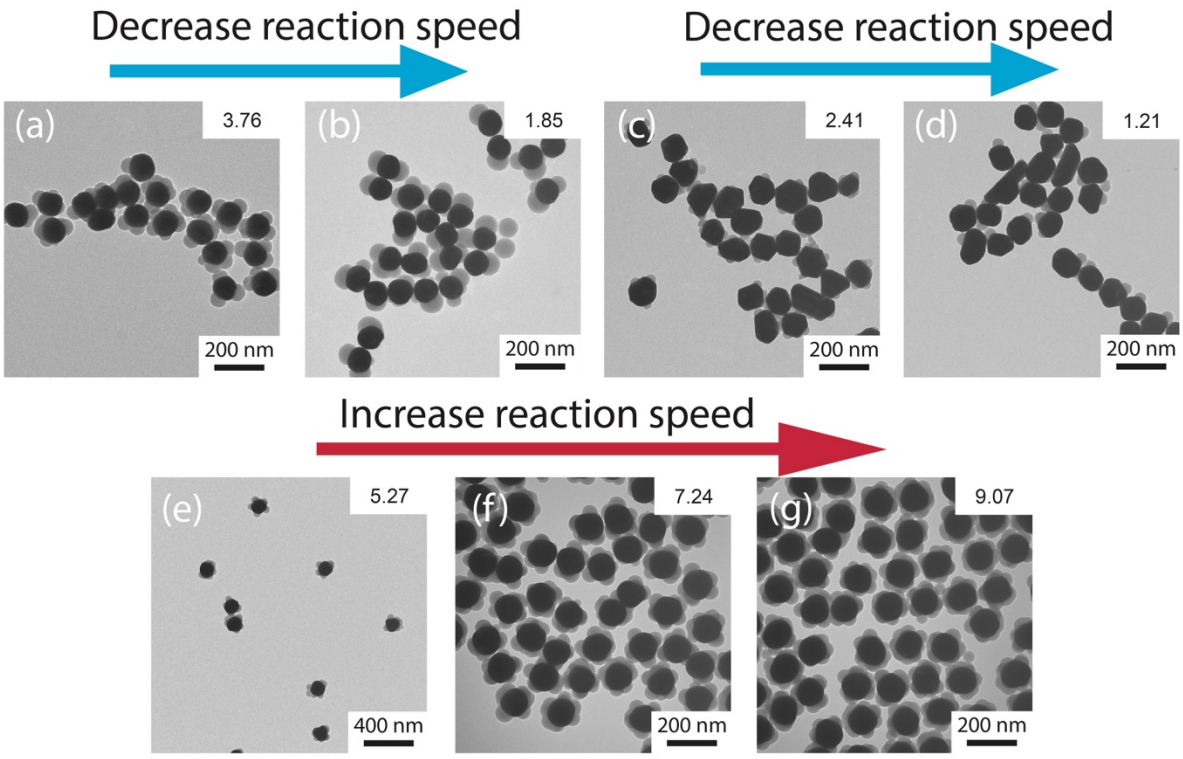

Figure 3.8. TEM images of 81 nm CTAC stabilized Au-silica heterogeneous structure synthesized in a) 2-propanol, b) tert-butanol, 120 nm citrate stabilized Au-silica heterogeneous structure synthesized in c) 2-propanol, d) tert-butanol. 117 nm CTAC stabilized Au-silica heterogeneous structure synthesized with e) 8.9 mM TEOS, f) 20.7 mM TEOS, g) 62.3 mM TEOS.

Since the monomer depletion zone triggers the Ostwald ripening that lead to redistribution of monomers to reduce surface energy, kinetic control can also influence the mass migration to change the depletion zone and therefore affect Ostwald ripening. Lim et.al demonstrated that reaction kinetics could be tuned by changing the solvent in the silica growth.[62] Therefore we switched the solvent from 2-propanol to tert-butanol. The formation of silica nanoparticles can be divided into two parts: hydrolysis and condensation. At the same time, with 2-propanol or tert-

butanol being the solvent, the isopropyl or tert-butyl exchange can compete with hydrolysis process, as illustrated in Equation 3.3 and Equation 3.4 below:

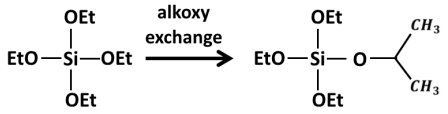

Equation 3.3

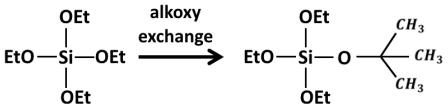

Equation 3.4

The alkoxy exchanged TEOS would have a different hydrolysis rate depending on the type of alkoxy group. Here the hydrolysis rate of isopropyl exchanged TEOS (equation 3) is faster than the tert-butyl exchanged TEOS (equation 4). Malay et.al discovered that due to the steric effect, the hydrolysis rate of tert-butyl exchanged TEOS is much slower than isopropyl exchanged TEOS.[63] Therefore the overall hydrolysis rate of TEOS was slowed down and less silane monomers were produced when tert-butanol was used as the solvent instead of 2-proponal. According to the mass transport law in equation (5),

$$\frac{\partial C}{\partial t} = D\left(\frac{\partial^2 C}{\partial x^2} + \frac{\partial^2 C}{\partial y^2} + \frac{\partial^2 C}{\partial z^2}\right) = D\nabla^2 C \qquad (5)$$

With a lower concentration of silane in the solution, the mass transport from the bulk solution to the center of the depletion zone slowed down and would result in an enlarged depletion zone. Which means more silica domains would be ripened to compensate for the silane monomer to reach equilibrium. As a result, the valency of 81 nm CTAC capped Au-silica heterogeneous

structure decreased from 3.76 to 1.85 (Figure 3.8a-b). Similarly, the valency of 120 nm citrate capped Au-silica heterogeneous structure also decreased from 2.41 to 1.21 (Figure 3.8c-d).

The reaction kinetics can also be controlled through controlling TEOS concentration while keeping the solvent as 2-proponal. As we increased the concentration of TEOS from 8.9 mM to 20.7 mM and finally 62.3 mM, we saw a gradual increase of valency from 5.27 to 7.24 and finally 9.07 (Figure 3.8e-g) using 117 nm CTAC capped Au NSs as seeds. The reaction was accelerated by increasing TEOS concentration, resulting in a faster diffusion rate and a less monomer scarce field. This less monomer scarce field would be able to support a greater number of silica domains. These results clearly indicate that the Ostwald ripening process could be kinetically controlled. With increased reaction speed Ostwald ripening was inhibited and vice versa. Similar conclusions were drew in Peng et.al's work, where they found that additional injection of the precursor would compensate for the depletion zone and hinder Ostwald ripening in the grow of CdSe crystals. [40]

3.5 Conclusions

In conclusion, we proposed that Ostwald ripening played a critical role in tuning the valency of the Au-silica heterogeneous structure. The ripening process can be either thermodynamically controlled (by tuning the surface wettability to tune the surface energy) or kinetically controlled (by tuning the reaction kinetics). Since Ostwald ripening is a common phenomenon that happens in particle growth of many different materials, the findings that the valency increased with increased Au core size, greater wettability and faster reaction speed could also be applicable in other heterogeneous growth systems.

3.6 Acknowledgements

This work is supported by NSF CAREER Grant (CHE 1554800). The electron microscopy imaging work was performed at the Biosciences Electron Microscopy Facility of the University of Connecticut.

3.7 [i]References

1. J. Du and R. K. O'Reilly, *Chem. Soc. Rev.*, 2011, **40**, 2402-2416.
2. M. Lattuada and T. A. Hatton, *Nano Today*, 2011, **6**, 286-308.
3. J. Hu, S. Zhou, Y. Sun, X. Fang and L. Wu, *Chem. Soc. Rev.*, 2012, **41**, 4356-4378.
4. R. Costi, A. E. Saunders and U. Banin, *Angew. Chem. Inter. Edi*, 2010, **49**, 4878-4897.
5. R. Jiang, B. Li, C. Fang and J. Wang, *Adv. Mater.*, 2014, **26**, 5274-5309.
6. K. Cai, Y. Liao, H. Zhang, J. Liu, Z. Lu, Z. Huang, S. Chen and H. Han, *ACS applied materials & interfaces*, 2016, **8**, 12792-12797.
7. W. Cao, R. Huang, W. Qi, R. Su and Z. He, *ACS applied materials & interfaces*, 2014, **7**, 465-473.
8. R. Costi, G. Cohen, A. Salant, E. Rabani and U. Banin, *Nano Lett.*, 2009, **9**, 2031-2039.
9. S.-H. Hu and X. Gao, *J. Am. Chem. Soc*, 2010, **132**, 7234-7237.
10. K. D. Rasamani, Z. Li and Y. Sun, *Nanoscale*, 2016, **8**, 18621-18625.
11. L. Chen, L. Li, L. Zhang, S. Xing, T. Wang, Y. A. Wang, C. Wang and Z. Su, *ACS applied materials & interfaces*, 2013, **5**, 7282-7290.
12. M. Gong, W. Zhou, M.-C. Tsai, J. Zhou, M. Guan, M.-C. Lin, B. Zhang, Y. Hu, D.-Y. Wang and J. Yang, *Nature communications*, 2014, **5**, 4695.
13. A. Walther and A. H. Müller, *Chem. Rev.*, 2013, **113**, 5194-5261.
14. X. Liu, J. Iocozzia, Y. Wang, X. Cui, Y. Chen, S. Zhao, Z. Li and Z. Lin, *Energy & Environmental Science*, 2017, **10**, 402-434.
15. S. Chen, S. Thota, G. Reggiano and J. Zhao, *J. Mater. Chem. C*, 2015, **3**, 11842-11849.
16. Y. Luo, L. Dube, Y. Zhou, S. Zou and J. Zhao, *Prog. Nat. Sci. Mat. Int.*, 2016, **26**, 449-454.
17. C. Zhang, Y. Xia, Z. Zhang, Z. Huang, L. Lian, X. Miao, D. Zhang, M. C. Beard and J. Zhang, *Chem. Mater.*, 2017, **29**, 3615-3622.
18. J. Ge, Q. Zhang, T. Zhang and Y. Yin, *Angew. Chem.*, 2008, **120**, 9056-9060.
19. F. X. Xiao, J. Miao, H. B. Tao, S. F. Hung, H. Y. Wang, H. B. Yang, J. Chen, R. Chen and B. Liu, *Small*, 2015, **11**, 2115-2131.
20. A. P. Alivisatos, K. P. Johnsson, X. Peng, T. E. Wilson, C. J. Loweth, M. P. Bruchez Jr and P. G. Schultz, *Nature*, 1996, **382**, 609.
21. T. Wang, D. LaMontagne, J. Lynch, J. Zhuang and Y. C. Cao, *Chem. Soc. Rev.*, 2013, **42**, 2804-2823.
22. M. R. Buck, J. F. Bondi and R. E. Schaak, *Nat. Chem.*, 2012, **4**, 37-44.
23. Y. Sun, *National Science Review*, 2015, **2**, 329-348.
24. L. Carbone and P. D. Cozzoli, *Nano Today*, 2010, **5**, 449-493.

25. T. Mokari, C. G. Sztrum, A. Salant, E. Rabani and U. Banin, *Nature Materials*, 2005, **4**, 855-863.
26. P. B. Landon, A. H. Mo, A. D. Printz, C. Emerson, C. Zhang, W. Janetanakit, D. A. Colburn, S. Akkiraju, S. Dossou and B. Chong, *Langmuir*, 2015, **31**, 9148-9154.
27. R. Miyanohata, T. Matsushita, T. Tsuruoka, H. Nawafune and K. Akamatsu, *J. Colloid Interface Sci.*, 2014, **416**, 147-150.
28. F. Wang, S. Cheng, Z. Bao and J. Wang, *Angew. Chem. Int. Ed.*, 2013, **52**, 10344-10348.
29. T. Mokari, E. Rothenberg, I. Popov, R. Costi and U. Banin, *Science*, 2004, **304**, 1787-1790.
30. L. Hong, S. Jiang and S. Granick, *Langmuir*, 2006, **22**, 9495-9499.
31. H. Wang, L. Chen, Y. Feng and H. Chen, *Accounts of chemical research*, 2013, **46**, 1636-1646.
32. J. G. Hinman, J. R. Eller, W. Lin, J. Li, J. Li and C. J. Murphy, *J. Am. Chem. Soc.*, 2017, **139**, 9851-9854.
33. H. Sun, J. He, J. Wang, S.-Y. Zhang, C. Liu, T. Sritharan, S. Mhaisalkar, M.-Y. Han, D. Wang and H. Chen, *J. Am. Chem. Soc.*, 2013, **135**, 9099-9110.
34. Y. Feng, J. He, H. Wang, Y. Y. Tay, H. Sun, L. Zhu and H. Chen, *J. Am. Chem. Soc.*, 2012, **134**, 2004-2007.
35. W. Ostwald, *Zeitschrift für physikalische Chemie*, 1900, **34**, 495-503.
36. Q. Zhang, W. Wang, J. Goebl and Y. Yin, *Nano Today*, 2009, **4**, 494-507.
37. H. C. Zeng, *J. Mater. Chem.*, 2006, **16**, 649-662.
38. R. Ouyang, J.-X. Liu and W.-X. Li, *J. Am. Chem. Soc.*, 2013, **135**, 1760-1771.
39. C. C. Yec and H. C. Zeng, *J. Mater. Chem. A*, 2014, **2**, 4843-4851.
40. X. Peng, J. Wickham and A. Alivisatos, *J. Am. Chem. Soc.*, 1998, **120**, 5343-5344.
41. N. G. Bastús, J. Comenge and V. Puntes, *Langmuir*, 2011, **27**, 11098-11105.
42. P. W. Wijnen, T. P. Beelen, K. P. Rummens, H. C. Saeijs, J. W. De Haan, L. J. Van De Ven and R. A. Van Santen, *Journal of colloid and interface science*, 1991, **145**, 17-32.
43. E. Piletska, H. Yawer, F. Canfarotta, E. Moczko, K. Smolinska-Kempisty, S. S. Piletsky, A. Guerreiro, M. J. Whitcombe and S. A. Piletsky, *Scientific reports*, 2017, **7**, 11537.
44. M. Darbandi, R. Thomann and T. Nann, *Chem. Mater.*, 2007, **19**, 1700-1703.
45. J. D. Rimer, O. Trofymluk, A. Navrotsky, R. F. Lobo and D. G. Vlachos, *Chem. Mater.*, 2007, **19**, 4189-4197.
46. D. P. Wang and H. C. Zeng, *Chem. Mater.*, 2011, **23**, 4886-4899.
47. Y. Zheng, X. Zhong, Z. Li and Y. Xia, *Part. Part. Syst. Charact.*, 2014, **31**, 266-273.
48. G. Frens, *Nature*, 1973, **241**, 20-22.
49. X. D. Tian, B. J. Liu, J. F. Li, Z. L. Yang, B. Ren and Z. Q. Tian, *J. Raman Spectrosc.*, 2013, **44**, 994-998.
50. T. Chen, G. Chen, S. Xing, T. Wu and H. Chen, *Chem. Mater*, 2010, **22**, 3826-3828.
51. W. Stöber, A. Fink and E. Bohn, *J. Colloid Interface Sci.*, 1968, **26**, 62-69.
52. M. Zinke-Allmang, L. C. Feldman and S. Nakahara, *Applied physics letters*, 1987, **51**, 975-977.
53. M. Iwamatsu, *The Journal of chemical physics*, 2014, **140**, 064702.
54. B. Peters, *The Journal of chemical physics*, 2011, **135**, 044107.
55. A. Lo and R. T. Skodje, *The Journal of Chemical Physics*, 2000, **112**, 1966-1974.
56. Y. Wang, J. He, C. Liu, W. H. Chong and H. Chen, *Angew. Chem. Inter. Ed.*, 2015, **54**, 2022-2051.
57. N. T. Thanh, N. Maclean and S. Mahiddine, *Chem. Rev.*, 2014, **114**, 7610-7630.

58. S. G. Kwon and T. Hyeon, *Small*, 2011, **7**, 2685-2702.
59. C. Zhu, H.-C. Peng, J. Zeng, J. Liu, Z. Gu and Y. Xia, *J. Am. Chem. Soc.*, 2012, **134**, 20234-20237.
60. M. Volmer and A. Weber, *Zeitschrift für physikalische Chemie*, 1926, **119**, 277-301.
61. R. Van den Berg, T. E. Parmentier, C. F. Elkjær, C. J. Gommes, J. Sehested, S. Helveg, P. E. de Jongh and K. P. de Jong, *ACS Catalysis*, 2015, **5**, 4439-4448.
62. J.-H. Lim, S.-W. Ha and J.-K. Lee, *Bulletin of the Korean Chemical Society*, 2012, **33**, 1067-1070.
63. O. Malay, I. Yilgor and Y. Z. Menceloglu, *J. Sol-Gel Sci. Technol.*, 2013, **67**, 351-361.
Sci. Technol., 2013, **67**, 351-361.

1. J. Du and R. K. O'Reilly, *Chem. Soc. Rev.*, 2011, **40**, 2402-2416.
2. M. Lattuada and T. A. Hatton, *Nano Today*, 2011, **6**, 286-308.
3. J. Hu, S. Zhou, Y. Sun, X. Fang and L. Wu, *Chem. Soc. Rev.*, 2012, **41**, 4356-4378.
4. R. Costi, A. E. Saunders and U. Banin, *Angew. Chem. Inter. Edi*, 2010, **49**, 4878-4897.
5. R. Jiang, B. Li, C. Fang and J. Wang, *Adv. Mater.*, 2014, **26**, 5274-5309.
6. K. Cai, Y. Liao, H. Zhang, J. Liu, Z. Lu, Z. Huang, S. Chen and H. Han, *ACS applied materials & interfaces*, 2016, **8**, 12792-12797.
7. W. Cao, R. Huang, W. Qi, R. Su and Z. He, *ACS applied materials & interfaces*, 2014, **7**, 465-473.
8. R. Costi, G. Cohen, A. Salant, E. Rabani and U. Banin, *Nano Lett.*, 2009, **9**, 2031-2039.
9. S.-H. Hu and X. Gao, *J. Am. Chem. Soc*, 2010, **132**, 7234-7237.
10. K. D. Rasamani, Z. Li and Y. Sun, *Nanoscale*, 2016, **8**, 18621-18625.
11. L. Chen, L. Li, L. Zhang, S. Xing, T. Wang, Y. A. Wang, C. Wang and Z. Su, *ACS applied materials & interfaces*, 2013, **5**, 7282-7290.
12. M. Gong, W. Zhou, M.-C. Tsai, J. Zhou, M. Guan, M.-C. Lin, B. Zhang, Y. Hu, D.-Y. Wang and J. Yang, *Nature communications*, 2014, **5**, 4695.
13. A. Walther and A. H. Müller, *Chem. Rev.*, 2013, **113**, 5194-5261.
14. X. Liu, J. Iocozzia, Y. Wang, X. Cui, Y. Chen, S. Zhao, Z. Li and Z. Lin, *Energy & Environmental Science*, 2017, **10**, 402-434.
15. S. Chen, S. Thota, G. Reggiano and J. Zhao, *J. Mater. Chem. C*, 2015, **3**, 11842-11849.
16. Y. Luo, L. Dube, Y. Zhou, S. Zou and J. Zhao, *Prog. Nat. Sci. Mat. Int.*, 2016, **26**, 449-454.
17. C. Zhang, Y. Xia, Z. Zhang, Z. Huang, L. Lian, X. Miao, D. Zhang, M. C. Beard and J. Zhang, *Chem. Mater.*, 2017, **29**, 3615-3622.
18. J. Ge, Q. Zhang, T. Zhang and Y. Yin, *Angew. Chem.*, 2008, **120**, 9056-9060.
19. F. X. Xiao, J. Miao, H. B. Tao, S. F. Hung, H. Y. Wang, H. B. Yang, J. Chen, R. Chen and B. Liu, *Small*, 2015, **11**, 2115-2131.
20. A. P. Alivisatos, K. P. Johnsson, X. Peng, T. E. Wilson, C. J. Loweth, M. P. Bruchez Jr and P. G. Schultz, *Nature*, 1996, **382**, 609.
21. T. Wang, D. LaMontagne, J. Lynch, J. Zhuang and Y. C. Cao, *Chem. Soc. Rev.*, 2013, **42**, 2804-2823.
22. M. R. Buck, J. F. Bondi and R. E. Schaak, *Nat. Chem.*, 2012, **4**, 37-44.
23. Y. Sun, *National Science Review*, 2015, **2**, 329-348.
24. L. Carbone and P. D. Cozzoli, *Nano Today*, 2010, **5**, 449-493.

25. T. Mokari, C. G. Sztrum, A. Salant, E. Rabani and U. Banin, *Nature Materials*, 2005, **4**, 855-863.
26. P. B. Landon, A. H. Mo, A. D. Printz, C. Emerson, C. Zhang, W. Janetanakit, D. A. Colburn, S. Akkiraju, S. Dossou and B. Chong, *Langmuir*, 2015, **31**, 9148-9154.
27. R. Miyanohata, T. Matsushita, T. Tsuruoka, H. Nawafune and K. Akamatsu, *J. Colloid Interface Sci.*, 2014, **416**, 147-150.
28. F. Wang, S. Cheng, Z. Bao and J. Wang, *Angew. Chem. Int. Ed.*, 2013, **52**, 10344-10348.
29. T. Mokari, E. Rothenberg, I. Popov, R. Costi and U. Banin, *Science*, 2004, **304**, 1787-1790.
30. L. Hong, S. Jiang and S. Granick, *Langmuir*, 2006, **22**, 9495-9499.
31. H. Wang, L. Chen, Y. Feng and H. Chen, *Accounts of chemical research*, 2013, **46**, 1636-1646.
32. J. G. Hinman, J. R. Eller, W. Lin, J. Li, J. Li and C. J. Murphy, *J. Am. Chem. Soc.*, 2017, **139**, 9851-9854.
33. H. Sun, J. He, J. Wang, S.-Y. Zhang, C. Liu, T. Sritharan, S. Mhaisalkar, M.-Y. Han, D. Wang and H. Chen, *J. Am. Chem. Soc.*, 2013, **135**, 9099-9110.
34. Y. Feng, J. He, H. Wang, Y. Y. Tay, H. Sun, L. Zhu and H. Chen, *J. Am. Chem. Soc.*, 2012, **134**, 2004-2007.
35. W. Ostwald, *Zeitschrift für physikalische Chemie*, 1900, **34**, 495-503.
36. Q. Zhang, W. Wang, J. Goebl and Y. Yin, *Nano Today*, 2009, **4**, 494-507.
37. H. C. Zeng, *J. Mater. Chem.*, 2006, **16**, 649-662.
38. R. Ouyang, J.-X. Liu and W.-X. Li, *J. Am. Chem. Soc.*, 2013, **135**, 1760-1771.
39. C. C. Yec and H. C. Zeng, *J. Mater. Chem. A*, 2014, **2**, 4843-4851.
40. X. Peng, J. Wickham and A. Alivisatos, *J. Am. Chem. Soc.*, 1998, **120**, 5343-5344.
41. N. G. Bastús, J. Comenge and V. Puntes, *Langmuir*, 2011, **27**, 11098-11105.
42. P. W. Wijnen, T. P. Beelen, K. P. Rummens, H. C. Saeijs, J. W. De Haan, L. J. Van De Ven and R. A. Van Santen, *Journal of colloid and interface science*, 1991, **145**, 17-32.
43. E. Piletska, H. Yawer, F. Canfarotta, E. Moczko, K. Smolinska-Kempisty, S. S. Piletsky, A. Guerreiro, M. J. Whitcombe and S. A. Piletsky, *Scientific reports*, 2017, **7**, 11537.
44. M. Darbandi, R. Thomann and T. Nann, *Chem. Mater.*, 2007, **19**, 1700-1703.
45. J. D. Rimer, O. Trofymluk, A. Navrotsky, R. F. Lobo and D. G. Vlachos, *Chem. Mater.*, 2007, **19**, 4189-4197.
46. D. P. Wang and H. C. Zeng, *Chem. Mater.*, 2011, **23**, 4886-4899.
47. Y. Zheng, X. Zhong, Z. Li and Y. Xia, *Part. Part. Syst. Charact.*, 2014, **31**, 266-273.
48. G. Frens, *Nature*, 1973, **241**, 20-22.
49. X. D. Tian, B. J. Liu, J. F. Li, Z. L. Yang, B. Ren and Z. Q. Tian, *J. Raman Spectrosc.*, 2013, **44**, 994-998.
50. T. Chen, G. Chen, S. Xing, T. Wu and H. Chen, *Chem. Mater*, 2010, **22**, 3826-3828.
51. W. Stöber, A. Fink and E. Bohn, *J. Colloid Interface Sci.*, 1968, **26**, 62-69.
52. M. Zinke-Allmang, L. C. Feldman and S. Nakahara, *Applied physics letters*, 1987, **51**, 975-977.
53. M. Iwamatsu, *The Journal of chemical physics*, 2014, **140**, 064702.
54. B. Peters, *The Journal of chemical physics*, 2011, **135**, 044107.
55. A. Lo and R. T. Skodje, *The Journal of Chemical Physics*, 2000, **112**, 1966-1974.
56. Y. Wang, J. He, C. Liu, W. H. Chong and H. Chen, *Angew. Chem. Inter. Ed.*, 2015, **54**, 2022-2051.
57. N. T. Thanh, N. Maclean and S. Mahiddine, *Chem. Rev.*, 2014, **114**, 7610-7630.

58. S. G. Kwon and T. Hyeon, *Small*, 2011, **7**, 2685-2702.
59. C. Zhu, H.-C. Peng, J. Zeng, J. Liu, Z. Gu and Y. Xia, *J. Am. Chem. Soc.*, 2012, **134**, 20234-20237.
60. M. Volmer and A. Weber, *Zeitschrift für physikalische Chemie*, 1926, **119**, 277-301.
61. R. Van den Berg, T. E. Parmentier, C. F. Elkjær, C. J. Gommes, J. Sehested, S. Helveg, P. E. de Jongh and K. P. de Jong, *ACS Catalysis*, 2015, **5**, 4439-4448.
62. J.-H. Lim, S.-W. Ha and J.-K. Lee, *Bulletin of the Korean Chemical Society*, 2012, **33**, 1067-1070.
63. O. Malay, I. Yilgor and Y. Z. Menceloglu, *J. Sol-Gel Sci. Technol.*, 2013, **67**, 351-361.

Chapter Four : Dielectric Domain Distribution on Au Nanoparticles Revealed by Localized Surface Plasmon Resonance

Reprinted and modified with permission from: Y. Luo, Y. Zhou, S. Zou and J. Zhao, J. Phys. Mater. C 2018, 6, 12038−12044.

4.1 Abstract

Localized surface plasmon resonance (LSPR) of metal nanoparticles has been proven to be sensitive to their dielectric environment and molecular binding, but less is known about the capability of LSPR towards differentiating homogeneous versus segregated molecular distribution on the nanoparticle surface. Using silica on Au nanospheres to mimic the dielectric change caused by molecules on the nanosphere surface, we have discovered that the LSPR of Au nanospheres is sensitive to the distribution of dielectric domains. We grew discrete silica domains or a continuous shell on the Au nanosphere surface and observed that the discrete domains of silica induced very little shift in the LSPR while the uniform shell caused a drastic shift. Theoretical modeling further confirmed that even when the volume of the silica was kept the same, the discreate domains had much smaller impact on the LSPR of Au nanospheres than the continuous shell. Moreover, for an anisotropic Au nanorod, the simulation results show that the LSPR is more sensitive to the dielectric change at the ends (“hot spot”) than the sides. The study suggests that the LSPR of metal nanoparticles can be conveniently used as an indirect method to reveal the dielectric distribution on the nanoparticles.

4.2 Introduction

Localized surface plasmon resonance, which is generated when light strikes a metal nanoparticle and induces collective oscillation of the conduction electrons of a noble metal nanoparticle, has been extensively studied over the past two decades. [1-5] LSPR of metal nanoparticles is dependent on various factors including composition, size, morphology, higher-order assembled structure, and local dielectric environment.[6-16] Especially, the dielectric sensitivity of LSPR enables them to detect the binding of molecules on the surface of the metal nanoparticle, which causes spectral shift in both the extinction and scattering spectra.[17, 18] This feature of LSPR allows for the development of a great number of biosensors that detect molecular binding events.[19-22]

Previous studies of the LSPR response of metal nanoparticles have demonstrated quantitatively how the amount of molecules or thickness of the dielectric layer on the nanoparticle would alter its LSPR both theoretically and experimentally.[23-30] However, another factor that can impact LSPR but did not get too much attention is the location and distribution of the molecular/dielectric layer on the nanoparticle.. In the work by Chen et.al, it was discovered that that Pd domains on Au nanorods would cause a redshift in the LSPR while a continuous Pd shell would cause a blue shift due to the transition of the real part of the dielectric environment from positive to negative.[31] However, how the distribution of a simple positive dielectric layer is not fully understood but still worth to be studied since dielectric domain segregation caused by inhomogeneous packing of molecules naturally occur on anisotropic metal nanoparticle surface due to the existence of crystal facets and curvatures.[32, 33] Even for a spherical metal nanoparticle capped with dual ligands, the molecules pack in striped or Janus patterns to reduce free energy.[34] One more specific case of non-uniform packing is the segregation of polymer brush caused by the

change of solvent quality.[35-37] Inspired by all these possible packing behaviours of molecules, we examine how the LSPR would respond to different distributions of the dielectric layer for better interpretation of LSPR shift in bio-sensing/detection. In addition, the packing of capping agents can heavily impact the site selective overgrowth of the coating material.[32, 33] The distribution of the ligands can also be manipulated to create anisotropy on isotropic nanospheres, enabling them to be directable building blocks for controlled assemblies.[38, 39] Different packing of surface ligands would also affect the cellular uptake behaviour and therefore is of fundamental importance in biomedical applications.[40] Therefore, it would be beneficial to test the capability of LSRP toward revealing the distribution of molecules on the nanoparticle surface. This would possibly enable LSPR to be an alternative in addition to extensive instrumentation to study molecular distribution at sub ~100 nm regime such as Electron Spin Resonance Spectroscopy, Nuclear Magnetic Resonance Spectroscopy, Atomic Force Microscopy and Scanning Tunnelling Microscopy.[41-45]

Here we demonstrate how the segregation of dielectric material on Au nanoparticle surface would impact the LSPR using Au-silica structures as a case study. We also test the possibility of using the shift of LSPR to reveal the dielectric layer distribution on metal nanoparticles. Specifically, we change the reaction conditions in silica overgrowth to tune the Au-silica structure from core@shell to core-satellite to mimic uniform or segregated ligands. The surface coverage of silica domains in the core-satellite structure can also be controlled by changing the reaction time. Moreover, imaging of silica is also easily achievable with transmission electron microscopy (TEM), which provides direct evidence of the dielectric domain distribution on Au nanoparticles in addition to the LSPR measurement. The TEM imaging enables us to establish a direct correlation between the dielectric domain distribution and the LSPR response. Surprisingly, we discovered that with highly uniform Au nanospheres (Au NSs) as the core, the discrete silica domains caused

almost no spectral shift in the UV-Vis spectra compared with that of the bare Au NSs. In stark contrast, a continuous silica shell of similar volume on the Au NSs induced a significant red-shift in the UV-Vis spectrum. Electrodynamics simulations of Au-silica structures agree with the experimental observations and show that when the dielectric domains are on the "hot spots" of the nanoparticles, a more drastic LSPR shift will be induced. The finding demonstrates that LSPR of Au nanoparticles is sensitive to the ligand distribution on the surface and can potentially be used as a convenient indirect method to study ligand binding and segregation on nanoparticles.

4.3 Experimental Section

4.3.1 Chemicals and materials

Gold (III) chloride trihydrate (≥99.9% trace metals basis), sodium boronhydride, L-ascorbic acid, hydroxylamine hydrochloride, hexadecyltrimethylammonium bromide (CTAB), cetyltrimethylammonium chloride solution (CTAC) (25% in water), 2-proponal (ACS reagent, ≥99%), poly (acrylic acid) (PAA) (average Mw=1800), 3-Mercaptopropionic acid (MPA) (≥99%,) and tetraethyl orthosilicate (TEOS) (≥99.0%) were purchased from Sigma Aldrich. Ammonium hydroxide (28.0-30.0%) was purchased from J. T. Baker. All chemicals were used as received.

4.3.2 Synthesis of CTAC capped Au NSs

Synthesis of 117 nm CTAC capped Au NSs was adopted from Xia's group with slight modification.[46] The detailed procedure can be found in Luo, et al.[47] In general, the synthesis was divided into 4 parts: 1. Cluster growth, 2. Growth of 14 nm Au NS, 3. Growth of 40nm Au NS and 4. Growth of 117 nm Au NS.

4.3.3 Synthesis of Au-silica heterostructure/Au@silica core@shell structure

We adopted and modified the method developed by Chen et.al to synthesize Au-silica heterogeneous and Au@silica core @shell structures.[48] More detailed procedure can be found in Luo, et al.[47] Briefly, 3 mL of the as prepared Au NS solution (5×10^{-11} M)were concentrated to 0.5 mL by centrifugation. The concentrated Au NS solution was added to 2.5 mL of 2-proponal. 20 μL of MPA (5 mM in ethanol) and 20 μL of PAA (0.645 mM in water) were then added to the solution (the PAA was eliminated in the synthesis of core@shell structure). The mixture was allowed to stir for 30 minutes. 600 μL of TEOS (8.9 mM in ethanol for 42 nm Au-silica heterostructures, 20.7 mM in ethanol for 117 nm heterostructures) and 90 μL of ammonium hydroxide were added afterwards. The reaction was kept under room temperature for certain amount of time for desired thickness/size (50 min-3 hours).

4.3.4 Transmission Electron Microscopy (TEM) imaging

Au and Au-SiO2 nanoparticles were transferred to a carbon-coated TEM grid (Electron Microscopy Sciences) for TEM imaging. FEI Tecnai G2 Spirit BioTWIN was used to acquire the TEM images under the acceleration voltage of 80 kV.

4.3.5 Scanning Electron Microscopy (SEM) imaging

To prepare the SEM sample, 10 μl of the sample was drop casted to a glass slide and left in air to dry. The glass slide was then coated with gold with a sputter coater to induce conductivity. FEI Nova NanoSEM 450 was used to acquire the SEM images.

4.3.6 UV-Vis Spectra Measurement

A UV−vis spectrometer (Cary 60, Agilent Technologies) was used to measure the extinction spectra of the Au NS and Au-silica structures.

4.3.7 Simulation

We used the discrete dipole approximation (DDA) method in the theoretical calculations. The detailed description of the method can be found in the reference.[49] In the DDA method, the target particle is divided into an array of polarizable cubes and the optical properties of any shaped particles can be calculated. The length of the cube was taken as 0.5 nm in all the simulations. The dielectric constants of gold were taken from Palik's handbook.[50]

4.4 Results and Discussion

4.4.1 Effect of uniform vs segregated distribution of silica on LSPR

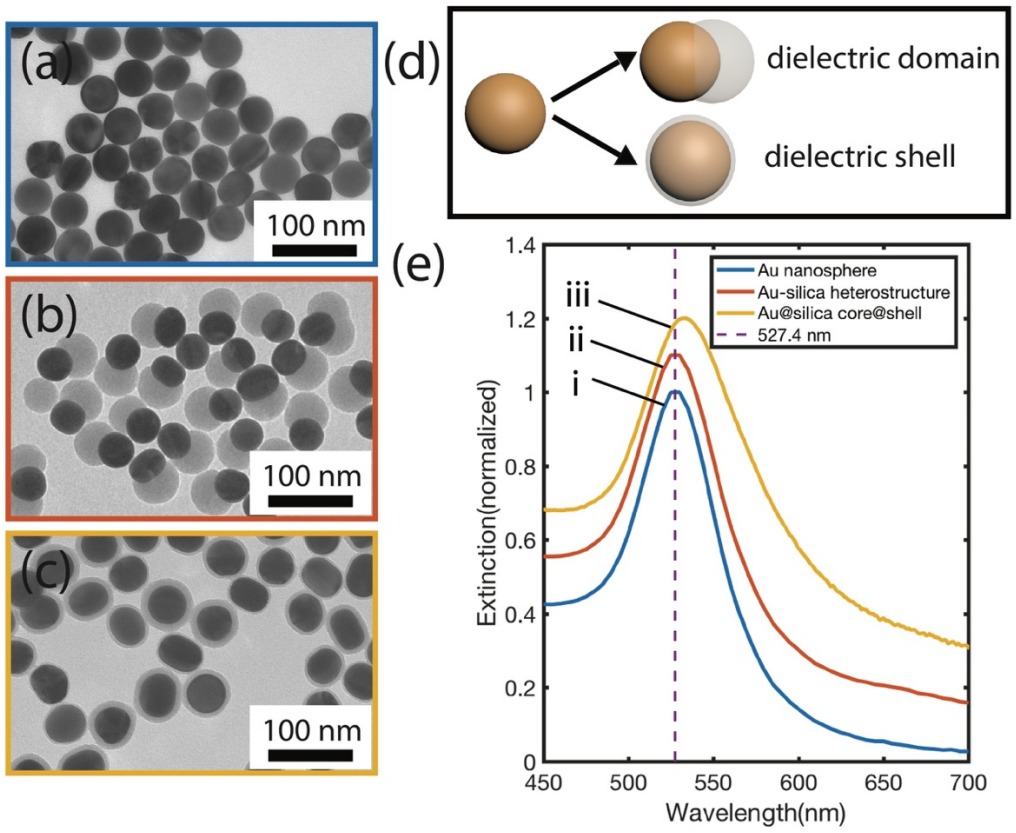

Figure 4.1. TEM images of a) 42 nm Au NS, b) 42 nm Au-silica heterostructure, c) 42 nm Au@silica core@shell, d) Schematic illustration of Au NS, Au-silica heterostructure and Au@silica core@shell structure, e)UV-Vis spectra of the corresponding structures.

Since the LSPR of a metal nanoparticle has been shown to be sensitive to its dielectric environment and ligand binding, we decided to test the capability of LSPR towards resolving the dielectric domain distribution around a nanoparticle. To do that, we synthesized two types of Au-silica structures: i.e. Au-silica heterostructure and Au@silica core@shell structure. Specifically,

the Au@silica core@shell structure simulated a uniform layer of capping agents on Au NSs and the Au-silica heterostructure simulated the Janus or segregated distribution of capping agents (Figure 4.1d). The morphology of the bare Au NSs and Au-silica structures were characterized with TEM and the extinction spectra of the samples were measured in water (Figure 4.1). The TEM images in Figure 1a showed that the bare Au NSs have a diameter of 42 nm. The extinction spectrum of the Au NSs in water has a peak at 527.4 nm (Figure 4.1e(i)). The Au NSs were used as seeds and a silica domain of 52 nm in diameter was grown on the Au NSs, as illustrated in the TEM image in Figure 1b. Surprisingly, the extinction spectrum of Au-silica heterostructure showed almost no shift in the peak wavelength (527.6 nm, Figure 4.1e(ii)) compared to that of bare Au NPs. This is contradictory with the generally accepted theory that LSPR is affected by the local dielectric environment. In contrast, when the distribution of silica domain changed from a segregated single domain to a shell that has an average thickness of 4.8 nm, there is a red shift of the extinction peak to 534.3 nm (Figure 4.1e(iii)). We would like to emphasize that the volume of the silica domains are similar for the samples shown in Figure 1b and 1c. These observations demonstrate that a uniform dielectric layer close to the Au NP surface has a more significant impact on the LSPR than a segregated dielectric domain of similar or even larger volume.

4.4.2 Effect of multiple discrete silica domains on LSPR

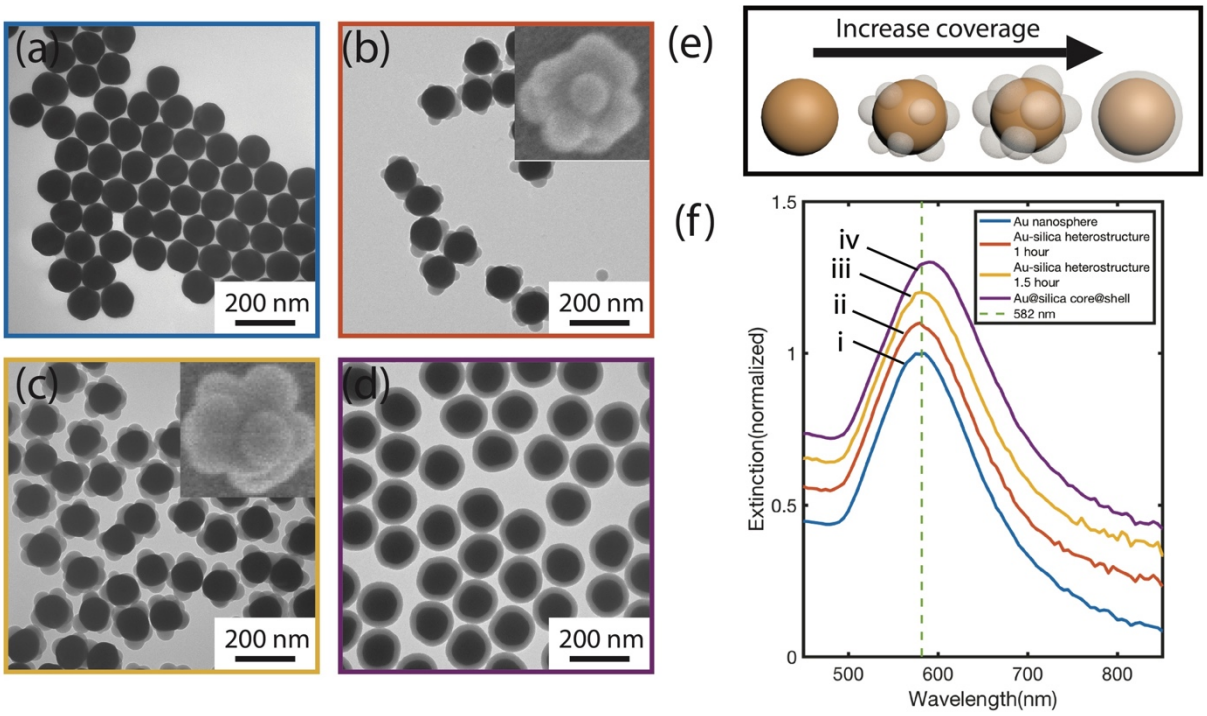

Figure 4.2. TEM images of a) 117 nm CTAC capped Au nanoparticle, 117 nm Au-silica heterostructure centrifuged after b) 1 hour of reaction, c) 1.5 hour of reaction, d)117 nm Au@silica core@shell structure ,e)Schematic illustration of corresponding structures, f) UV-Vis spectra of the corresponding structures.

In the cases when dual ligands are employed in nanoparticles simultaneously, the ligands don't necessarily segregate in a Janus pattern; instead, multiple domains may form. If the two ligands are distinctly different in molecular weight, the segregated pattern is analogous to having multiple discrete silica domains on the Au NS surface. In contrast, the random distribution of the two ligands is similar to a uniform silica shell covering the whole surface of the NS. To examine whether the LSPRs of metal nanoparticles can be used to distinguish the two cases, Au-silica structures of multiple discrete silica domains or a uniform shell were synthesized and compared.

Specifically, 117 nm Au NSs (TEM image in Figure 4.2a) were employed as the seeds because it could support multiple discrete silica domain growth according to our previous study.[47] The silica domain size was controlled by the reaction time. The Au-silica heterogeneous structure that were synthesized in 1 hour of reaction had an average of 7 silica domains with a diameter of 50 nm based on the TEM image in Figure 4.2b. When the reaction proceeded for 1.5 hrs, silica size increased to a diameter of 63 nm (shown in the TEM image in Figure 4.2c). The synthesized Au-silica heterostructures with different domains sizes and Au@silica core@shell structures simulate different ligand patterns as illustrated in Figure 4.2e. UV-Vis spectra of the samples were acquired in water (Figure 4.2f) as a comparison. Similar to what was observed in the above case, the Au-silica heterostructure with 1 hr growth showed almost no shift in the LSPR peak compared with that of the bare Au NS (Figure 4.2f (i, ii), both peaked at 581.6 nm). The Au-silica heterostructure obtained from 1.5 hr of reaction had same number of silica domains as the 1 hr sample but bigger domain size. In this case we observed a small red-shift in the LSPR peak from 581.6 nm to 584.9 nm compared with the bare Au NSs (Figure 4.2(iii)). As the silica grew in size, the height and contacting area with Au both increased. Since the plasmon decay length of Au nanoparticle is 5~15 nm,[51] LSPR is the most sensitive to the dielectric environment change on the nanoparticle's surface. Therefore, we focus the following discussion on the surface coverage of silica in the different samples. There were 6 silica domains visible in the SEM image (Figure 4.3) on the Au NSs on average. We assumed there were two more domains hidden below the Au NS, making the total of 8 domains. The assumption is based on the Au core size and the silica domain diameter. We estimated that the contacting area of the 1 hr sample was 17665 nm2 while the contacting area of the 1.5 hr sample was 28985 nm2. As the surface area of a 117 nm Au in diameter can be easily calculated to be 42983 nm2, the coverage of the 1 hr sample is calculated as 41% while the 1.5 hr

sample is 67.4%. For the 40-60% surface coverage, the LSPR shift is observable but quite small. In contrast, Au@silica core@shell structure with a thin silica shell of 22 nm thickness (Figure 2d) showed a pronounced LSPR shift from 581.6 nm to 591.9 nm with 100% uniform coverage (Figure 4.2f(iv)). From our observations, we conclude that coating the Au NSs with discrete domains induced a small shift in the LSPR of Au NSs in comparison with a uniform coating on the entire surface. Although the experiments were performed on Au-silica system, the same conclusion will hold for other metal nanospheres with ligands or biomolecules.

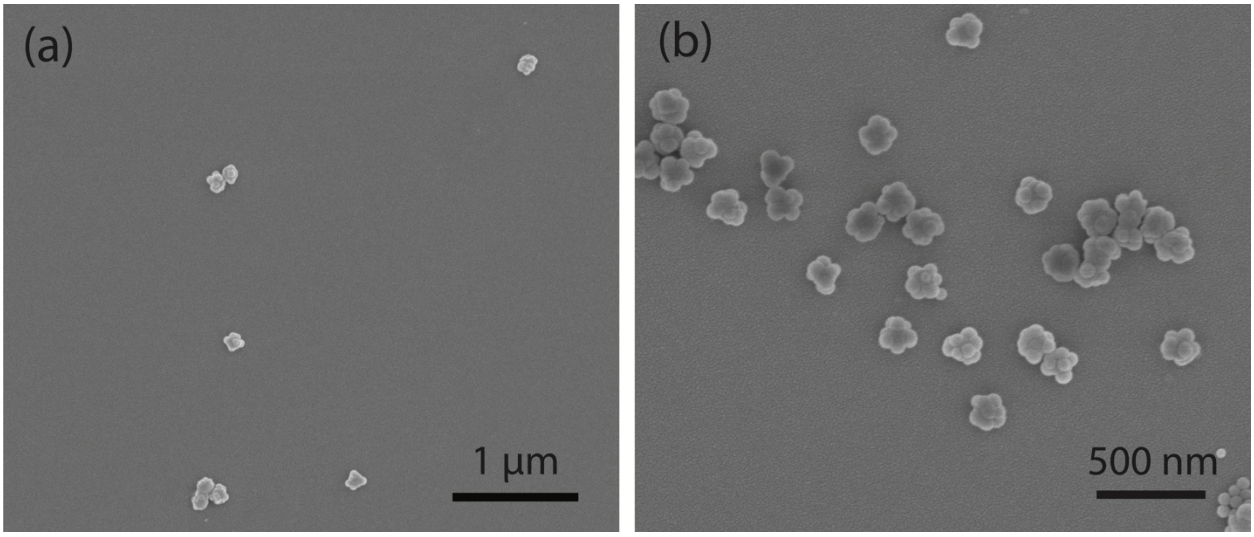

Figure 4.3. SEM images of 117 nm Au-silica heterostructure centrifuged after a) 1 hour of reaction, b) 1.5 hour of reaction

4.4.3 Simulations of the LSPR of Au NS coated with silica domains

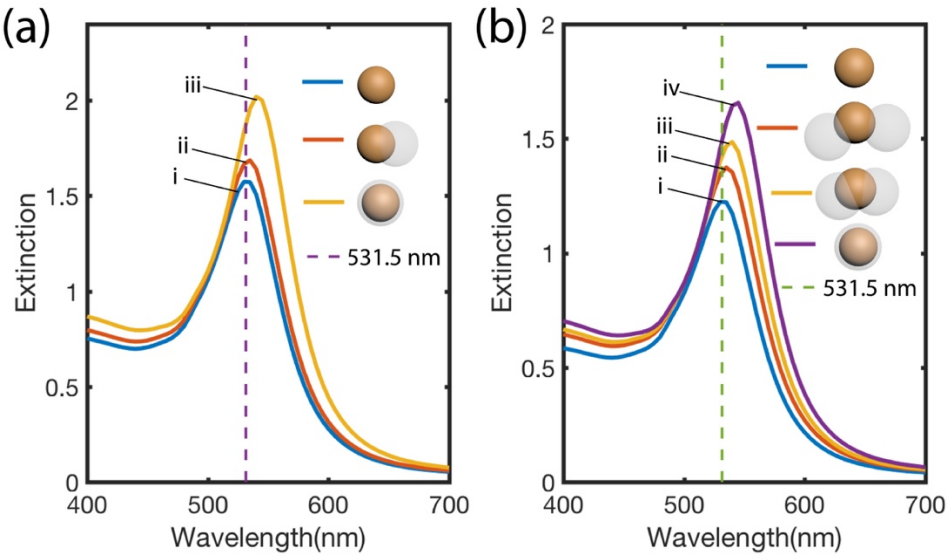

Figure 4.4. a) simulated extinction spectra of bare Au sphere (i, blue spectrum), Au with one silica domain (ii, red spectrum) and Au with a silica shell (iii, yellow spectrum). b) simulated extinction spectra of bare Au sphere (i, blue spectrum), Au and two silica domain with a small overlap (ii, red spectrum), Au and two silica domain with a large overlap (iii, yellow spectrum) and Au with a silica shell (iv, purple spectrum).

The phenomenon we observed where coating Au NSs with silica domains induced very small LSPR shift was contradictory with many previous studies. It has been demonstrated LSPR of Au nanoparticles is sensitive to molecular binding. To understand this unusual LSPR behaviour of the Au NSs, theoretical modeling was performed to simulate the experimental results and to provide information about the LSPR shift mechanism. Using the discrete dipole approximation (DDA) method,[49] we calculated the extinction spectra of Au spheres under different coating conditions in water. The details of the method can be found in the experimental section. To match

the experimental results, the diameter of the Au sphere was set to 42 nm. In Figure 4.4a, we showed the extinction spectrum of an Au NS with a diameter of 42 nm in water. The extinction peak is at 531.5 nm, in good agreement with the experimental results in Figure 4.1e. In another simulation, we modeled the case where a silica domain with a 52 nm diameter was coated onto the Au sphere with a center to center distance of 42 nm, as illustrated in Figure 4.4a. To account for the random orientation of the Au-silica nanoparticles in solution, in the simulations, we randomly placed a silica particle near the Au sphere and carried out five simulations. The averaged extinction spectrum of the five simulations is presented in Figure 4.4a (ii). The resonance wavelength is only changed very slightly from 531.5 nm to 533.4 nm compared to that of the bare Au sphere. In stark contrast, when the Au NS is coated with a layer of silica with the same volume as that of a 52 nm diameter silica "sphere" (the "sphere" is incomplete in this case because the overlap between the silica and Au as illustrated in Figure 4.4a), the resonance wavelength red shifted more pronouncedly from 531.5 to 541.2 nm. Notice that in the simulated results, when a silica domain was added to the side of the Au sphere, it induced a small red shift in the LSPR. But in the experimental results in Figure 4.1e, we did not observe any LSPR shift caused by the silica domain. This discrepancy mainly comes from the variations in the size of the Au NS and the silica domains. The measured extinction spectrum was essentially an averaged spectrum over a large number of Au-silica structures of slightly different morphologies. The small LSPR shift caused by silica domain was averaged out in the experimental measurement. Nevertheless, the simulated results agree with the experimental observations that a uniform silica coating caused much bigger LSPR shift than a silica domain of similar volume.

To further investigate the effect of dielectric domain distribution on LSPR, we compared the extinction spectra of Au NSs when they are coated with two silica spheres with different

amount of overlap between silica and Au NS. In the simulations, the sizes of the Au sphere and silica sphere remain the same as in the previous simulations. For the structure in Figure 4.4b that corresponds to the spectrum ii in Figure 4.4b, the center to center distance between the silica domain and the Au NS was set at 42 nm. Again, the two silica domains were randomly arranged near the Au NS. Five simulations were carried out to obtain the averaged results. In comparison to that of the bare Au sphere, the resonance wavelength of the Au NS coated with two silica domains is only shifted from 531.5 to 534.9 nm. However, when a layer of silica with the same volume of the two incomplete silica spheres was coated on the Au NS surface, the resonance wavelength is further red shifted to 543.3 nm (Figure 4.4b (iv)). Quite interestingly, when we randomly placed two silica spheres with a center to center distance between the Au and silica spheres of 21 nm (the scheme corresponding to spectrum iii in Figure 4.4b), the volume of the coated silica spheres is less than the case when the center to center distance was at 42 nm, due to the larger overlap between the Au NS and silica domains. However, the resonance wavelength showed a bigger redshift to 538.2 nm. The simulated results demonstrate that the total volume of silica is not the critical factor in determining the LSPR shift. Instead, how much silica is in direct contact or in close proximity to the surface has a more significant role in inducing LSPR shift.

From both the experimental and theoretical results, the LSPR of Au NSs is more sensitive to the immediate dielectric domains to the surface of the Au. The volume or thickness of the dielectric layer has less impact on the LSPR compared to the surface coverage. It is still surprising that there was almost no shift in the LSPR when the silica domains were coated on Au nanoparticles in some cases. We attribute it to the following reason. The Au nanoparticles we used are spherical in shape. Previous works have demonstrated the spheres have the least LSPR sensitivity compared to particles with high aspect ratios or sharp tips and edges.[52] We expect that if the nanoparticles are

more rod-like, the LSPR will be more sensitive to segregated dielectric domains. To demonstrate this effect experimentally, we synthesized Au nanoparticles using citrate acid instead of CTAC as the ligand. The nanoparticles have an average diameter of 120 nm, similar to that of the nanoparticles in Figure 4.2. The citrate capped nanoparticles are quasi-spherical or rod-like in shape and have a faceted surface instead of being spherical (Figure 4.5). When one or two small silica domains were grown onto the nanoparticles, a LSPR shift from 590.0 nm to 592.8 nm was observed. In comparison, the CTAC capped Au NSs showed almost no shift in the LSPR when small silica domains were coated onto them. The LSPR was then further shifted to 594.0 nm as we increased the number of silica domains. To demonstrate how the dielectric domains would influence the LSPR of an quasi-spherical Au nanoparticle, we synthesized the citrate capped Au nanoparticle with discrete silica domains. The TEM image shows that the 120 nm citrate capped Au nanoparticles are quasi-sphereical and a few of the particles exhibit rod-like shape (Figure 4.5a). We also controlled the number of silica domains by controlling the reaction kinetics to tune the coverage. The mechanism of reaction kinetics influencing the number of silica domains can be found in Luo et. al's work.[53] The Au-silica heterostructure synthesized in tert-butanol has 1.21 hemispherical silica domains on average as revealed by the TEM image (Figure 4.5b). The silica domains have an average diameter of 49.4 nm. UV-vis spectra show a red shift from 590 nm to 592.6 nm compared with the bare Au nanoparticle. The Au-silica heterostructure synthesized in 2-propanol has an average number of 2.41 silica domains with an average diameter of 43.3 nm (Figure 4.5c). Even though the size of silica was slightly smaller compared with Au-silica synthesized in tert-butanol, the LSPR of the Au-silica synthesized in 2-propanol still red shifted to 594 nm due to the increased number of domains (Figure 4.5d). This observation proves that the LSPR of quasi-spherical or rod-like Au nanoparticles is more sensitive to the change of the

dielectric environment.This control experiment showed that the irregular shaped Au nanoparticles are more sensitive to the dielectric domains.

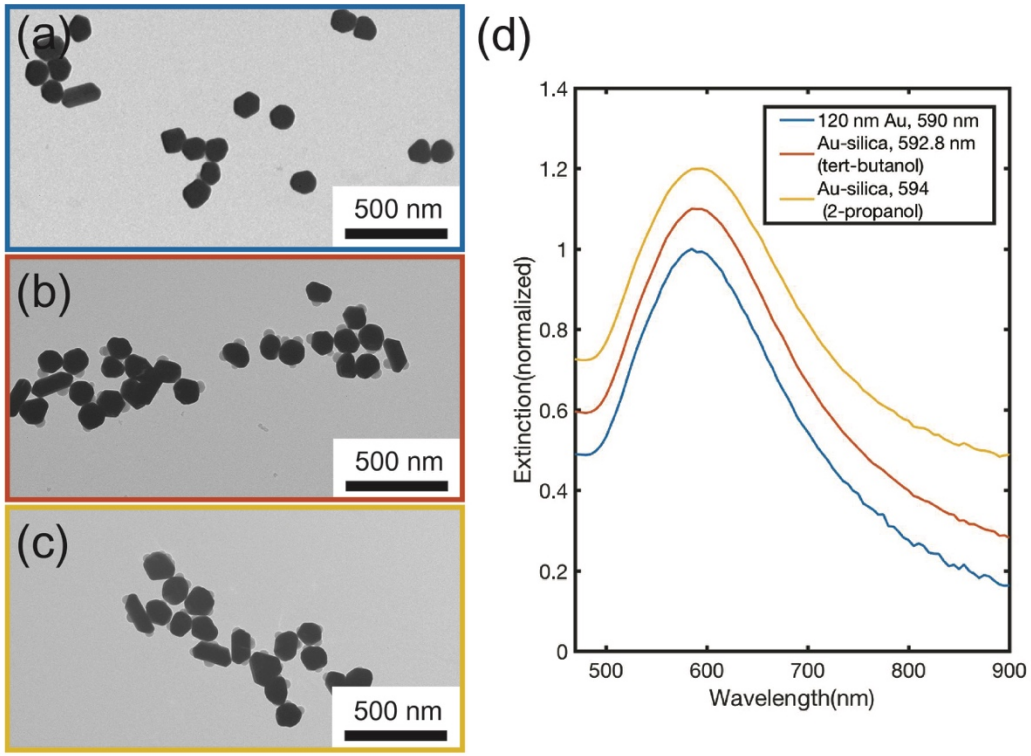

Figure 4.5. TEM images of a) 120 nm citrate capped Au nanoparticle, 120 nm Au-silica heterostructure synthesized in b) tert-butanol, c) 2-propanol, d) UV-vis spectra of the corresponding structures.

4.4.4 Simulations of the LSPR of Au nanorod coated by silica domains

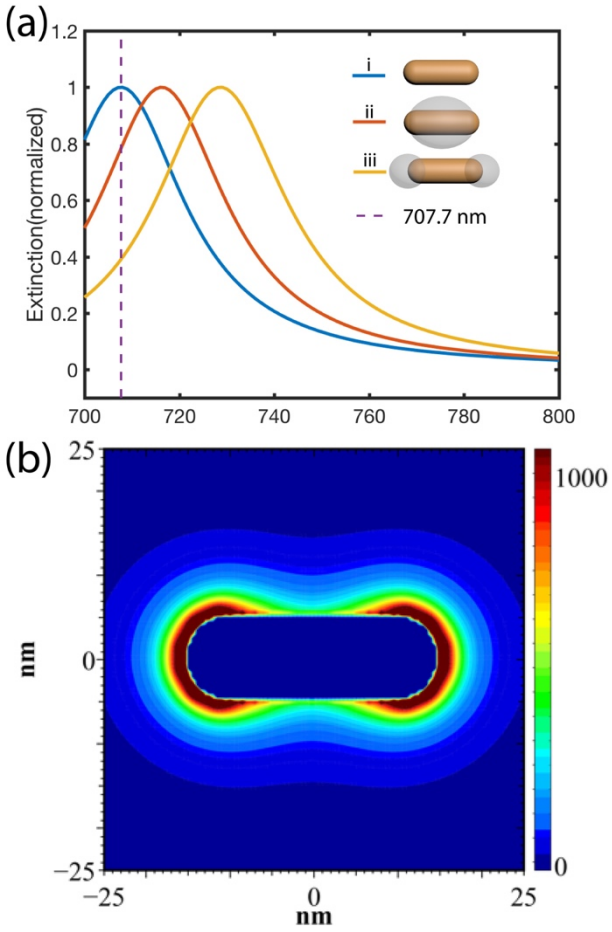

Figure 4.6. (a) simulated extinction spectra of a Au nanorod (i), Au rod with silica coated on the side (ii) and Au rod with silica coated at the ends (iii). (b) electric field contour plot for the bare rod at the resonance wavelength of 708 nm.

The Au NSs we used in the experiments have an aspect ratio of 1. To determine the LSPR sensitivity to the ligands of nanostructures with higher aspect ratio, we also calculated the resonance wavelength of an Au rod when it was coated with silica at different positions, i.e. sides vs. ends. Such structures have been first reported by Wang's and Murphy's groups.[32, 33] The rod

length was selected as 30 nm and the diameter was 10 nm. Two silica spheres were coated at the two ends of the rod with a diameter of 15 nm which represent a 2.5 nm thick silica at the two ends of the rod. The structure is illustrated in Figure 4.6a scheme (ii). In another calculation, a spheroidal silica particle with diameters of 18.5, 18.5, and 19 nm was coated at the center of the rod (scheme (iii) in Figure 4.6a). The volume of the coated silica was the same in two simulations. The calculated extinction spectra of the longitudinal mode are shown in Figure 4.6a and the complete spectra are available in Figure 4.7. The resonance wavelength is shifted from 708 nm for the bare rod to 716 nm when the silica was coated on the sides of the rod and further to 729 nm when the silica domains were coated at the two ends. We also calculated the electric field distribution of the bare rod at the resonance wavelength of 708 nm which is shown in Figure 4.6b. The electric field contour plot indicates that the enhanced local electric fields are much higher at the two ends. The high electric field makes the impact of silica coating at the ends of the rods on LSPR more significant than the case when silica was coated to the sides with lower electric field. Therefore, LSPR is more sensitive to ligand binding to the "hot spots" compared to elsewhere. This finding is in agreement with the experimental results reported by Wang's gourp.[32] Szekreńyes et.al discovered that after small molecules (cysteamine) replaced the bulky polyethylene glycol (PEG) at the tips of a PEGylated gold nanorod, the LSPR showed a pronounced blue shift from 640 nm to 628 nm.[44] Zhu et.al's work showed similar results as well. The coating of silica at the ends of Au nanobipyramids caused greater spectral red-shift compared with silica coating on the side.[54] Whitney et.al also showed that the sharp feature (an "apron" of Ag at the bottom) of the a Ag hemispheroid created a stronger near field and induced greater LSPR sensitivity toward the local dielectric change.[24] All the experimental and theoretical studies demonstrate that LSPR can

be used as an indirect tool to study ligand distribution and molecular binding on metal nanoparticles.

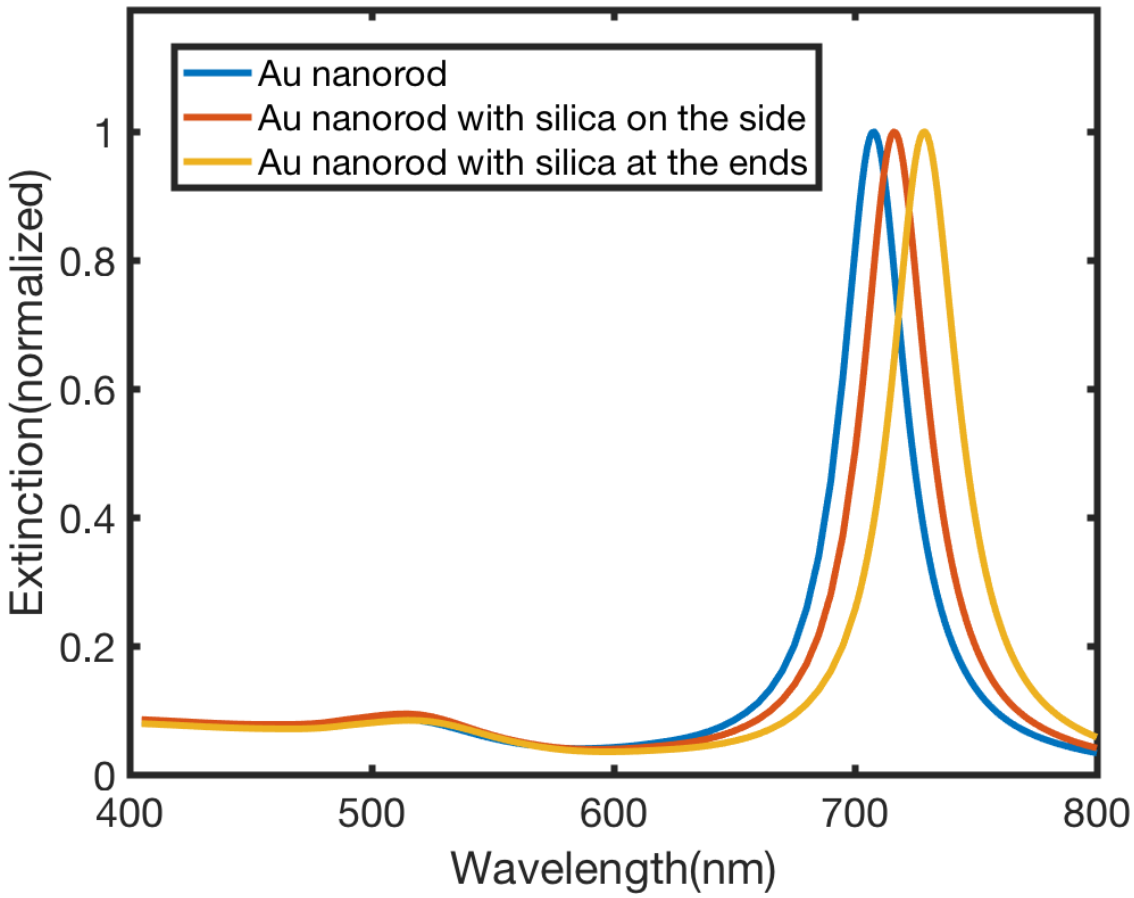

Figure 4.7. Simulated extinction spectra of a Au nanorod (blue), Au rod with silica coated on the side (red) and Au rod with silica coated at the ends (yellow).

4.5 Conclusions

In this work, experimental and theoretical studies were performed on Au-silica nanostructures where the silica domain distribution was controlled. The system was used to mimic

segregated/uniform ligand distribution on metal nanoparticles. We found that the LSPR of the Au nanoparticles depends on the distribution of the silica domain instead of volume of the silica domains. Specifically, segregated domains at one side of the Au nanoparticle induced much less (or almost no) LPSR shift compared to the uniformly distributed domain of the same or even smaller volume. Dielectric domains at the "hot spots" induce much greater LSPR shift than elsewhere. The conclusions from this work can be broadly applied to many plasmonically-active metal nanoparticles to reveal the ligand and dielectric layer distribution on these nanoparticles.

4.6 Acknowledgements

We acknowledge the financial supported by NSF CAREER Grant (CHE 1554800). The electron microscopy imaging work was performed at the Biosciences Electron Microscopy Facility of the University of Connecticut.

4.7 References

1. M. Faraday, *Philosophical Transactions of the Royal Society of London*, 1857, **147**, 145-181.
2. U. Kreibig and M. Vollmer, *Optical properties of metal clusters*, Springer Science & Business Media, 2013.
3. K. L. Kelly, E. Coronado, L. L. Zhao and G. C. Schatz, *Journal*, 2003.
4. S. Link and M. A. El-Sayed, *Annual review of physical chemistry*, 2003, **54**, 331-366.
5. S. Eustis and M. A. El-Sayed, *Chem. Soc. Rev.*, 2006, **35**, 209-217.
6. U. Kreibig and L. Genzel, *Sur. Sci.*, 1985, **156**, 678-700.
7. J. Mock, M. Barbic, D. Smith, D. Schultz and S. Schultz, *J. Chem. Phys.*, 2002, **116**, 6755-6759.
8. C. L. Haynes and R. P. Van Duyne, *Journal*, 2001.
9. E. Hutter and J. H. Fendler, *Adv. Mater.*, 2004, **16**, 1685-1706.
10. W. A. Murray and W. L. Barnes, *Adv. Mater.*, 2007, **19**, 3771-3782.
11. V. Myroshnychenko, J. Rodríguez-Fernández, I. Pastoriza-Santos, A. M. Funston, C. Novo, P. Mulvaney, L. M. Liz-Marzan and F. J. G. de Abajo, *Chem. Soc. Rev.*, 2008, **37**, 1792-1805.
12. C. Novo, A. M. Funston, I. Pastoriza-Santos, L. M. Liz-Marzan and P. Mulvaney, *J. Phys. Chem. C*, 2008, **112**, 3-7.

13. Y. Luo, L. Dube, Y. Zhou, S. Zou and J. Zhao, *Prog. Nat. Sci. Mat. Int.*, 2016, **26**, 449-454.
14. S. Thota, S. Chen, Y. Zhou, Y. Zhang, S. Zou and J. Zhao, *Nanoscale*, 2015, **7**, 14652-14658.
15. J. A. Jenkins, Y. Zhou, S. Thota, X. Tian, X. Zhao, S. Zou and J. Zhao, *J. Phys. Chem. C*, 2014, **118**, 26276-26283.
16. X. Tian, Y. Zhou, S. Thota, S. Zou and J. Zhao, *J. Phys. Chem. C*, 2014, **118**, 13801-13808.
17. J. Piella, N. G. Bastús and V. Puntes, *Chem. Mater.*, 2016, **28**, 1066-1075.
18. K. M. Mayer and J. H. Hafner, *Chem. Rev.*, 2011, **111**, 3828-3857.
19. K. A. Willets and R. P. Van Duyne, *Annu. Rev. Phys. Chem.*, 2007, **58**, 267-297.
20. S. Szunerits and R. Boukherroub, *Chem. Commun.*, 2012, **48**, 8999-9010.
21. B. Sepúlveda, P. C. Angelomé, L. M. Lechuga and L. M. Liz-Marzán, *nano today*, 2009, **4**, 244-251.
22. M. Shen, A. A. Joshi, R. Vannam, C. K. Dixit, R. G. Hamilton, C. V. Kumar, J. F. Rusling and M. W. Peczuh, *ChemBioChem*, 2018.
23. J. J. Mock, D. R. Smith and S. Schultz, *Nano Lett.*, 2003, **3**, 485-491.
24. A. V. Whitney, J. W. Elam, S. Zou, A. V. Zinovev, P. C. Stair, G. C. Schatz and R. P. Van Duyne, *J. Phys. Chem. B*, 2005, **109**, 20522-20528.
25. T. Rindzevicius, Y. Alaverdyan, M. Käll, W. A. Murray and W. L. Barnes, *J. Phys. Chem. C*, 2007, **111**, 11806-11810.
26. M. Duval Malinsky, K. L. Kelly, G. C. Schatz and R. P. Van Duyne, *J. Phys. Chem. B*, 2001, **105**, 2343-2350.
27. E. Galopin, J. Niedziółka-Jönsson, A. Akjouj, Y. Pennec, B. Djafari-Rouhani, A. Noual, R. Boukherroub and S. Szunerits, *J. Phys. Chem. C*, 2010, **114**, 11769-11775.
28. S. K. Ghosh, S. Nath, S. Kundu, K. Esumi and T. Pal, *J. Phys. Chem. B*, 2004, **108**, 13963-13971.
29. S. Link, M. Mohamed and M. El-Sayed, *J. Phys. Chem. B*, 1999, **103**, 3073-3077.
30. L. J. Sherry, R. Jin, C. A. Mirkin, G. C. Schatz and R. P. Van Duyne, *Nano Lett.*, 2006, **6**, 2060-2065.
31. H. Chen, F. Wang, K. Li, K. C. Woo, J. Wang, Q. Li, L.-D. Sun, X. Zhang, H.-Q. Lin and C.-H. Yan, *ACS nano*, 2012, **6**, 7162-7171.
32. F. Wang, S. Cheng, Z. Bao and J. Wang, *Angew. Chem. Int. Ed.*, 2013, **52**, 10344-10348.
33. J. G. Hinman, J. R. Eller, W. Lin, J. Li, J. Li and C. J. Murphy, *J. Am. Chem. Soc.*, 2017, **139**, 9851-9854.
34. P. K. Ghorai and S. C. Glotzer, *J. Phys. Chem. C*, 2010, **114**, 19182-19187.
35. R. B. Grubbs, *Polym. Rev.*, 2007, **47**, 197-215.
36. Y. Wang, J. He, C. Liu, W. H. Chong and H. Chen, *Angew. Chem. Int. Ed*, 2015, **54**, 2022-2051.
37. S. Zhang, G. Leem, L.-o. Srisombat and T. R. Lee, *J. Am. Chem. Soc.*, 2008, **130**, 113-120.
38. T. Chen, M. Yang, X. Wang, L. H. Tan and H. Chen, *J. Am. Chem. Soc.*, 2008, **130**, 11858-11859.
39. C. P. Shaw, D. G. Fernig and R. Lévy, *J. Mater. Chem*, 2011, **21**, 12181-12187.
40. V. Schubertová, F. J. Martinez-Veracoechea and R. Vácha, *Soft Matt.*, 2015, **11**, 2726-2730.
41. C. Gentilini and L. Pasquato, *J. Mater. Chem*, 2010, **20**, 1403-1412.
42. X. Liu, M. Yu, H. Kim, M. Mameli and F. Stellacci, *Nature Commun.*, 2012, **3**, 1182.

43. C. Gentilini, P. Franchi, E. Mileo, S. Polizzi, M. Lucarini and L. Pasquato, *Angew. Chem. Int. Ed*, 2009, **48**, 3060-3064.
44. D. P. Szekrenyes, S. Pothorszky, D. Zámbó, Z. Osváth and A. Deák, *The Journal of Physical Chemistry C*, 2018.
45. A. M. Jackson, Y. Hu, P. J. Silva and F. Stellacci, *J. Am. Chem. Soc.*, 2006, **128**, 11135-11149.
46. Y. Zheng, X. Zhong, Z. Li and Y. Xia, *Particle & Particle Systems Characterization*, 2014, **31**, 266-273.
47. Y. G. Luo, Shenghao; Dube, Lacie; Zhao, Jing, unpublished work.
48. Y. Wang, G. Chen, M. Yang, G. Silber, S. Xing, L. H. Tan, F. Wang, Y. Feng, X. Liu and S. Li, *Nature communications*, 2010, **1**, 87.
49. B. T. Draine and P. J. Flatau, *JOSA A*, 1994, **11**, 1491-1499.
50. A. D. Rakić, A. B. Djurišić, J. M. Elazar and M. L. Majewski, *Appl. Opt.*, 1998, **37**, 5271-5283.
51. A. J. Haes, S. Zou, G. C. Schatz and R. P. Van Duyne, *J. Phys. Chem. B*, 2004, **108**, 109-116.
52. A. U. Khan, S. Zhao and G. Liu, *The Journal of Physical Chemistry C*, 2016, **120**, 19353-19364.
53. Y. G. Luo, Shenghao; Dube, Lacie; Zhao, Jing, unpublished work.
54. X. Zhu, H. Jia, X. M. Zhu, S. Cheng, X. Zhuo, F. Qin, Z. Yang and J. Wang, *Adv. Funct. Mater.*, 2017, **27**, 1700016.

Chapter Five : Strong Coupling of Quantum Dots with a Plasmonic Nanocavity Created by a Gold Dimer

5.1 Abstract

Plasmon-exciton interaction enters strong coupling regime when the energy exchange rate between these two exceeds any other decay rates in the hybrid system. As a result, a hybrid plexcitonic state is generated yielding two new modes, which is recognized as Rabi-splitting. If the energy difference of the two modes exceeds the sum of the plasmon and exciton decay rate, the two peaks can be the spectrally resolved in both dark-field scattering and fluorescence spectra. However, with a plasmonic cavity it is challenging to achieve strong coupling because of the lossy nature of metal. With the large decay rate of plasmon, Fano resonance can easily occur, giving rise to an asymmetrical line shape or creating a dip. This spectral feature can be easily confused with Rabi-splitting. Here we aim to demonstrate how to effectively increase the coupling strength to enter strong-coupling regime. Moreover, we hope to illustrate how to tune from Fano resonance to Rabi-splitting. The coupling strength of the hybrid system highly depends on the intrinsic property of the exciton and plasmonic cavity, as well as the structural arrangement of the plasmon-exciton hybrid structure. Here we used colloidal methods to fabricate Au-Quantum Dot (QD)-Au hybrid structure to demonstrate the impact of mode volume of the plasmonic cavity on the coupling strength to realize strong coupling. With decreased gap size of the gold dimer, we observed the splitting effect of both dark-filed scattering and fluorescence spectra. Transmission Electron Microscopy (TEM)and Scanning Electron Microscopy (SEM) correlation further confirmed the origin of the splitting was due to the strong plasmon-exciton coupling.

5.2 Introduction

The weak side of plasmon-exciton interaction, which involves using a plasmonic cavity to modulate the absorption and emission of quantum emitters has proven itself as a powerful strategy to develop bio-sensing, imaging and solar cells [1-3] While weak coupling may easily occur when the quantum emitters are placed near the plasmonic nanostructures, strong coupling requires more strict conditions.[4] To reach strong coupling ,the coupling strength (energy exchange rate) between the plasmon and quantum emitter should be maximized so it can exceed the decay rate of plasmon or exciton. As a result, the energy coherently oscillates between the plasmon and exciton giving rise to a new plexcitonic state, featured as two new generated modes. Plasmon-exciton strong coupling opens a new and exciting area of light matter interaction, serving as a promising candidate for realizing thresholdless polariton lasing, solar cells and single photon non-linear optics.[5-10]

The right criteria to identify strong coupling should not be limited to observing peak splitting in dark-field scattering because Fano interference (intermediate plasmon-exciton coupling) might induce very similar spectral line shapes.[11, 12] Fano resonance is an effect of constructive and destructive interference in the far field, which is observable in dark-field scattering but not fluorescence spectrum. The condition for Rabi-splitting and Fano Resonance to happen is also quite different as former favors a plasmonic cavity possessing a slow damping rate, while latter requires a fast damping rate. Faucheaux et.al demonstrated that with a slow plasmon damping rate, the expression of the scattering cross section yields two Lorentzian peaks, while a fast damping rate would induce a dip or asymmetrical line shape on top of a Lorenzian peak.[13] However there's not a clear boundary between the two effects so they may co-exist in the same system. Since the coupling strength $g \propto \sqrt{\frac{n}{V}}$, where n is the number of the excitons and V is the

mode volume, successful demonstration of the strong coupling regime has been realized with either incorporating multiple excitons into the hybrid system or/and reducing the mode volume through gap mode or extra sharp features.[14] However, there is not a systematic study of demonstrating delicate tuning from weak to intermediate to strong coupling with precise control of the experimental parameters to reveal the impact of specific factor on the coupling strength. Colloidal methods, offers great flexibility of assembling hybrid structures with nano-meter precision and well-defined structures. [15, 16] In theory, colloidal assembled dimer structure with quantum dots (QDs) trapped in the gap is a very interesting structure to study the coupling effect between the exciton and the two distinct plasmonic modes. Moreover, the colloidal method are able to achieve small gap size and induce strong coupling. However, there is not yet a successful method of assembling Au-QD structure to exhibit strong coupling effect. Here we used colloidal methods to assemble Au-QD-Au sandwich structure with well-defined gap size to show how the coupling strength is controlled by the mode volume.

5.3 Experimental Section

5.3.1 Chemicals

Gold (III) chloride trihydrate (≥99.9% trace metals basis), hydroxylamine hydrochloride, 2-propanol (ACS reagent, ≥99%), 3-mercaptopropionic acid (MPA) (≥99%,), tetraethyl orthosilicate(TEOS) (≥99.0%) were purchased from Sigma Aldrich. Poly(ethylene glycol) methyl ether thiol (PEG-SH) (average M_n=5000 g/mol) was purchased from Polymer Source. Sodium citrate dehydrate was purchased from Fisher Scientific. Ammonium hydroxide (28.0-30.0%) was purchased from J. T. Baker. All chemicals were used as received.

5.3.2 Au nanoparticle synthesis

We followed a published procedure to synthesis the 100 nm Au nanoparticle with slight modification[17]. We first synthesized 40 nm Au nanoparticle as the seed following Frens' method.[18] Then, 53 mL of distilled water was added to around bottom flask under vigorous stirring followed by addition of 6 mL of the previously prepared 40 nm seed. After 2 minutes, 900 μL of sodium citrate solution (0.0388 M) was added to the flask dropwise. Again after 2 minutes, 0.8 mL of HAuCl4 (0.0254 M) was added to the flask. Finally, after another 2 minutes, 1.3 mL of hydroxylamine hydrochloride solution (0.0101 M) was added dropwise and the round bottom flask was removed from the stir plate after 2 hours.

5.3.3 QD synthesis and phase transfer

We adopted the method reported by Chen et.al to synthesized and functionalize the CdSe/CdS QD with PEG-SH.[19] First, we dissolved 10 mg of PEG-SH in 5 ml of chloroform. Then 2 ml of QDs dispersed in chloroform (3 mg/ml) was added to the PEG-SH solution dropwise. The solution was left under stir for overnight. After 12 hours, hexane was added to the solution to precipitate the QDs and the mixture was centrifuged under 5000rpm for 15 minutes. The supernatant was discarded, and menthol was added to dissolve the QDs. Finally, the methanol was dried under N_2 gas blowing. The dried QD was finally dispersed in 8 ml of water.

5.3.4 Au@silica Synthesis

We adopted and modified the method developed by Chen et.al to synthesize Au@silica core@shell structure.[20] 6 mL of the 100 nm Au nanoparticle was concentrated to 3 ml of solution by centrifugation and then transferred to 15 mL of 2-proponal. 120 μL of 3-mercaptopopionic acid

(5 mM in ethanol) were then added to the solution. The mixture was allowed to stir for 30 minutes. 4 μL of tetraethyl orthosilicate, 3 μL of (3-Aminopropyl) triethoxysilan and 540 μL of ammonium hydroxide were added afterwards. The reaction was kept under room temperature for 1 hour and centrifuged for 3 times and was finally dispersed in 3 ml of DI water.

5.3.5 Au-QD-Au Assembly

50ul of the QD-PEH solution was added to the 3 ml of Au@silica solution. The mixture was allowed to stir for 12 hours to ensure sufficient dissolution of silica. As a result, Au-QD-Au structure was formed.

5.3.6 Sample Preparation

TEM correlation: The Au-QD-Au solution was diluted by 10 times with DI water and 4 μL of the diluted sample was drop-casted on a TEM grid. The grid was left in open air to dry. This sample was then used for single particle optical measurement as well as TEM imaging.

SEM correlation: The Au-QD-Au solution was diluted by 10 times with ethanol and 4 μL of the diluted sample was drop-casted on a glass slide. The glass slide was left in open air to dry. A copper reference grid was glued on the glass slide to help locate the particles under SEM imaging. This sample was then used for single particle optical measurement as well as SEM imaging.

5.3.7 Single Particle optical study and TEM/SEM correlation

The sample was examined under Nikon Ti-u microscope with an unpolarized/polarized halogen lamp. The dark field condenser (NA 0.85) was adjusted to focus the incident light at the specimen plane. The scattered light was focused by a 100× NA 0.8 oil immersed objective

(variable NA 0.8–1.3) and then passed thought a manually controlled slit to the spectrograph (Isoplane SCT 320, Princeton Instruments) equipped with a CCD camera (PIXIS 1024 BR, Princeton Instruments). Single particle spectra were collected by narrowing the slit and selecting proper area of interest. The spectrum correction was carried out by subtracting the background and then dividing the lamp signal collected from nearby area with no particles. The TEM grid was then examined with FEI Tecnai G2 Spirit BioTWIN to locate the particles and acquire the TEM images.

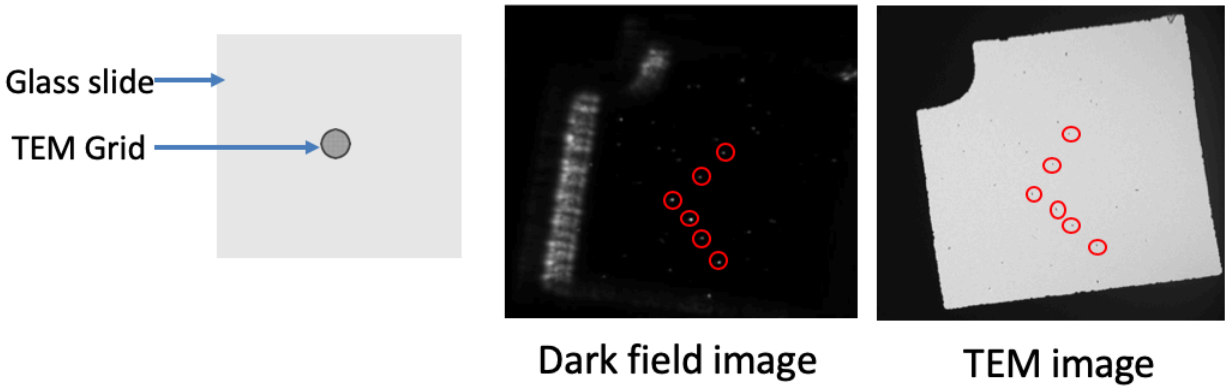

Figure 5.1 Demonstration of the TEM correlation technique

To measure the single structure fluorescence, the prepared glass slide was placed under the microscope with a 405 nm pulsed laser (Picoquant) sent through the objective to excite the sample. The emitted photon was focused by the same objective and sent to the CCD camera. The glass slide was thereafter examined with FEI Nova NanoSEM 450 to acquire SEM images.

5.4 Results and Discussion

5.4.1 Structural design

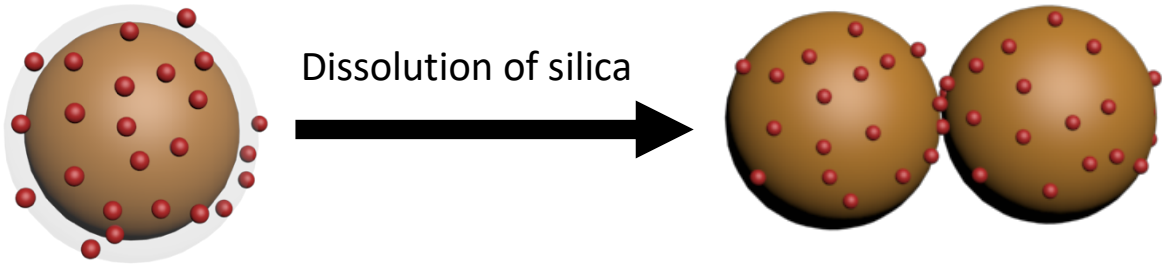

Scheme 5.1. Assembly strategy of forming Au-QD-Au sandwich strucre by utilizing silica-NH_2 as the adhesion layer.

The strategy of achieving the Au-QD-Au sandwich structure to utilizing the silica-amine layer as the adhesion layer. The QDs are modified with PEG-SH, which interacts with the silica layer through hydrogen-bonding. Since the silica layer is doped with APTES, the amine on the surface interacts with the negative charge of the $Si\text{-}O^-$ and force the Au-silica -QD hybrid structure to aggregate and form dimers. APTES doped silica is highly porous so the layer dissolves over time and shorten the distance between the dimers.[21] The product was incubated in water to dissolve the silica layer and over 12 hours the silica layer would almost completely disappear, so that Au-Au distance is limited by the size of the QD in the gap.(Figure 5.2) Here we used two different sizes CdSe/CdSs core/shell QDs. The size of the QDs are 8 and 5 nm respectively. After the coating of PEG-SH, the diameter of the overall structure increased to 11 and 8 nm, which determines the maximum size of the gap in the gold dimer.

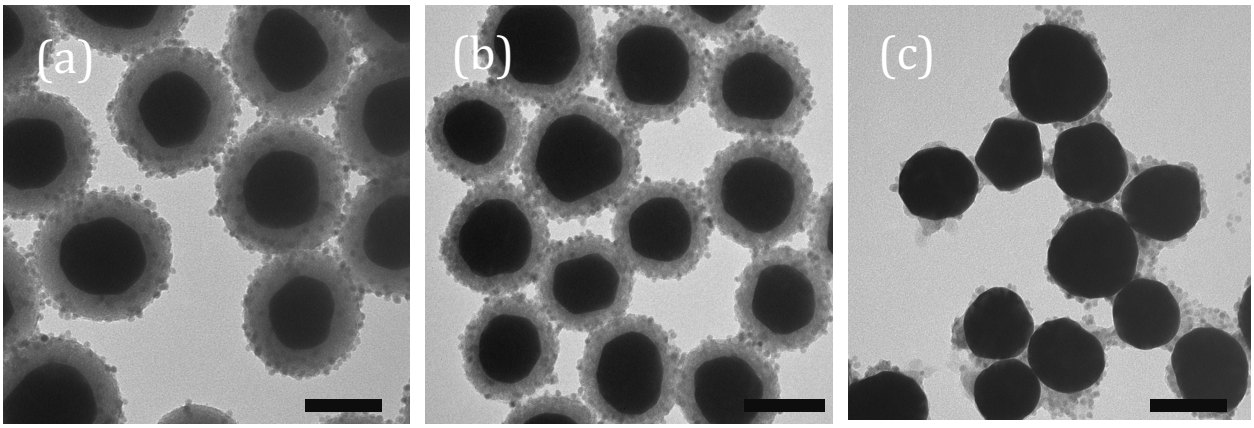

Figure 5.2 (a) TEM image of the Au-silica-QD structure prepared after incubation of 2 minutes (b) 4 hours; (c) 12 hours. Scale bar: 100 nm.

5.4.2 Single particle optical characterization

5.4.2.1 Plasmonic coupling effect with 8 nm QD

Figure 5.3 shows TEM images of two representative Au-QD-Au structures with corresponding single particle dark-field scattering spectra. The TEM images clearly shows that the QDs are attaching to the surface of the Au nanoparticles with the silica layer almost completely dissolved. With the aggregation of the Au-silica-QD, the QDs were incorporated into the gap of the Au dimer. The corresponding dark-field scattering spectra shows two distinct peaks of the Au dimer, indicating the plasmonic coupling effect of these two Au nanoparticles. However, there is no additional peak splitting observed. To further examine the origin of the two peaks, a polarizer was inserted into the light path, so the nanostructures were illuminated under polarized light. As the polarization of the light changed, a clear decay of the shorter peak was observed in respect to the rise of the longer wavelength with almost no change of the peak position, indicating the origin of the two peaks are from plasmonic coupling instead of plasmon-exciton strong coupling. The

shorter wavelength feature originated from the transverse mode and the longer wavelength originated from the longitudinal mode. Based on the single particle spectra it obvious that there is no strong coupling effect.

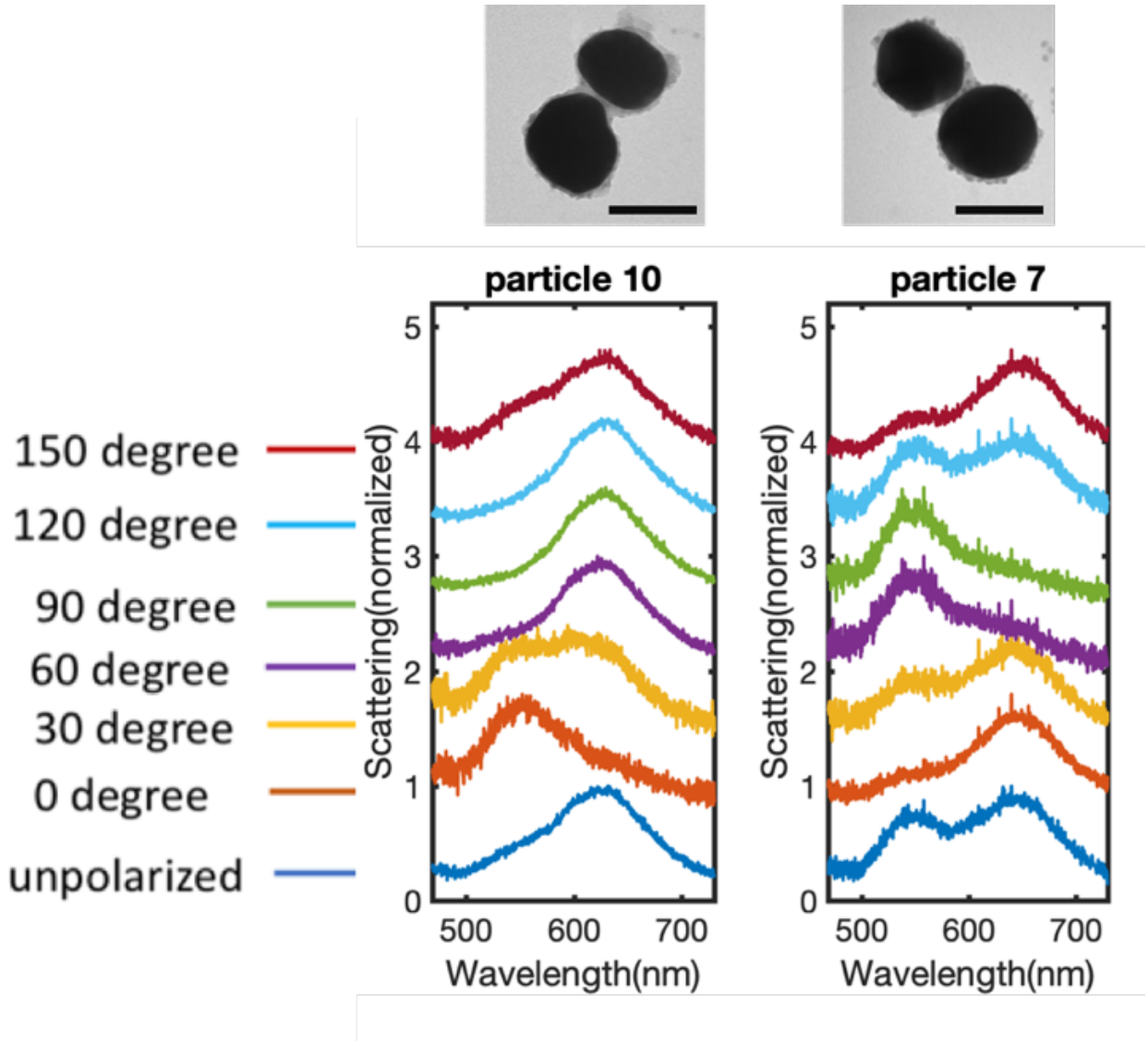

Figure 5.3. TEM images of individual Au-QD-Au structures and corresponding single particle dark-field scattering spectra

5.4.2.2 Plasmonic Coupling effect with 5 nm QD

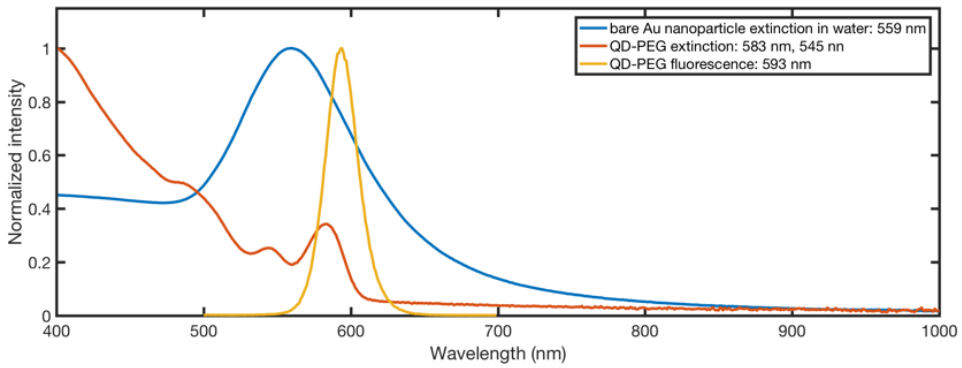

Figure 5.4. Extinction spectra of Au nanoparticle. Extinction and fluorescence spectra of QD-PEG.

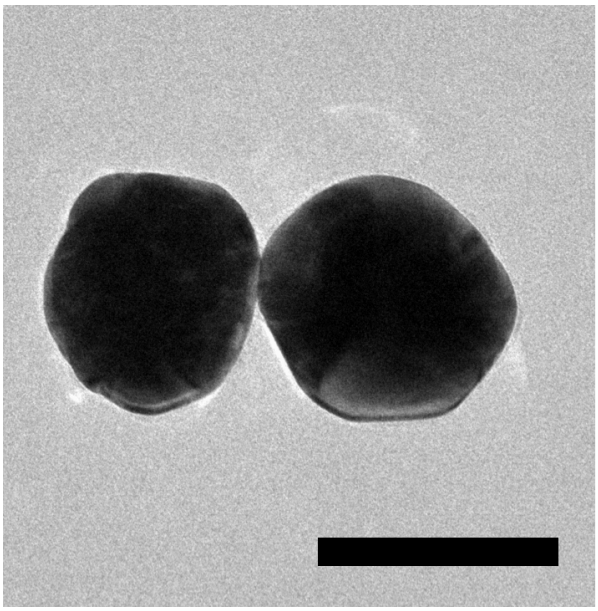

Figure 5.5 TEM image of Au-5nm QD-Au structure. Scale bar: 100 nm.

To explore the impact of the mode volume to the coupling strength, a smaller QD with diameter of 5 nm was selected. Due to the size effect on the QD band gap, the fluorescence peak was much blue shifted to 590 nm compared to that of the 8 nm QDs. The TEM images showed several representative dimer structures. However, the QDs are hardly visible in the gap. This is due to the much smaller size of the QDs compared to Au nanoparticles. Since the two Au spheres are not identical in size, the size mismatch makes the gap to be hidden underneath the bigger particle. With the 8 nm QDs the gap can still be partially visible. However, with 5 nm QD the gap almost disappeared under TEM image. (Figure 5.5) Neverthelss, we believed that there were indeed QDs in the structure because of the strong fluorescence we observed from it, as discussed below. Different from the spectra observed with the Au-8 nm QD-Au, the Au-5 nm QD-Au clearly showed three distinct peaks in dark field scattering spectrum and two peaks in fluorescence spectrum. (Figure 5.6(c)) The peak splitting clearly demonstrated the impact of mode volume toward plasmon-exciton coupling strength. We further used polarized light to excite the structure to examine how the transverse/longitudinal plasmon mode interact with exciton. With 0-degree polarization, the transverse mode was excited. We observe a major peak at 580 nm and a small shoulder at 674 nm. We believe the small shoulder was due to the non-spherical shape of the left particle, which appeared to be more rod-like. With 90-degree polarization, the longitudinal mode was excited, and we observed two major peaks at 625 and 745 nm with a shoulder at 551 nm. The 551 should was attributed to the non-symmetrical shape of the dimer and the 90 degree is not perfectly aligned to the direction of longitudinal mode. The 625 and 745 nm peaks are believed to originate from plasmon-exciton interaction. However, the peak splitting in very small as one peak

is at 586 nm while the other is at 597 nm. The splitting energy in fluorescence is much smaller than that in scattering. This phenomenon suggests that the line shape in dark-field scattering is largely due to Fano resonance while that in fluorescence is solely due to Rabi-splitting.

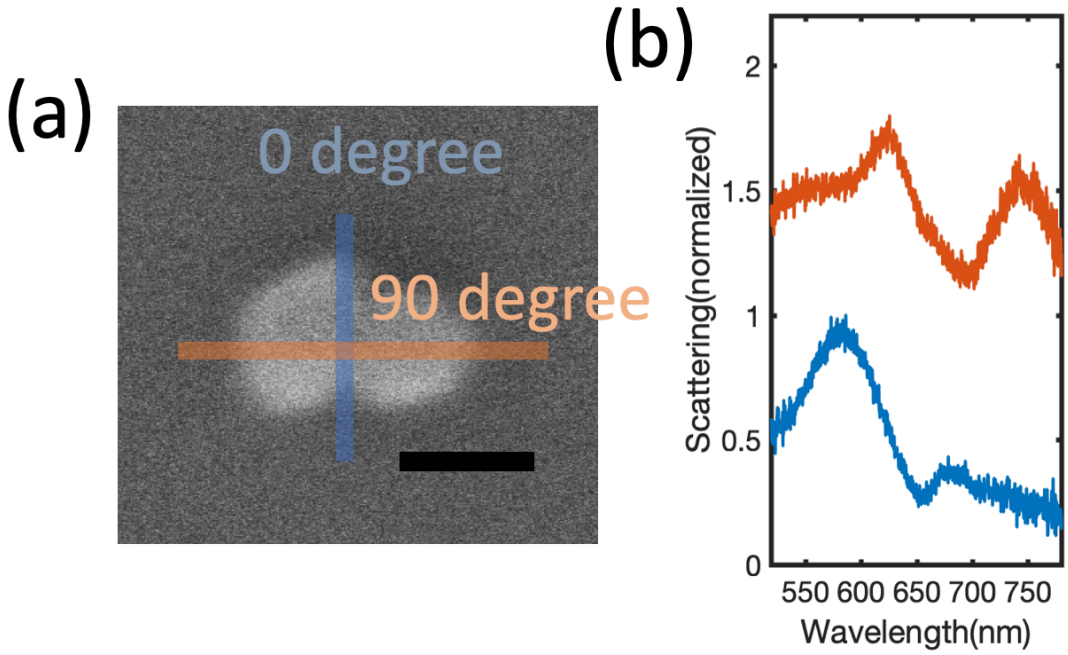

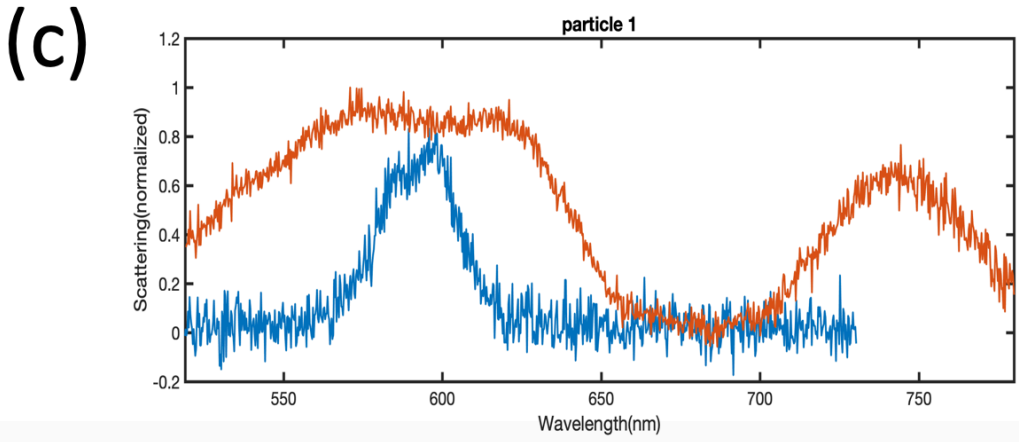

Figure 5.6. (a) SEM image of a Au-QD-Au structure. Scale bar: 100 nm. (b) corresponding single particle dark-field scattering spectra under excitation of 0/90 degree polarized light. (c) corresponding single particle dark-field scattering under unpolarized light (red) and fluorescence spectra (blue).

5.5 Conclusions

In this work we designed the Au-QD-Au structure and demonstrated the impact of mode volume toward plasmon-exciton coupling strength. The mode volume was simply controlled by the size of QD. This is to our knowledge the first time using colloidal methods to fabricate the Au-QD-Au structure that exhibits Rabi-splitting effect. TEM and SEM correlation technique was used here to visualize the structure of the single particle examined under optical microscope, providing direct evidence of the origin of the peak splitting was originated form plasmon-exciton coupling instead of plasmon-plasmon coupling. In our system we observed the co-existed Fano and Rabi effect while Fano effect dominating in the scattering spectrum and Rabi is the only effect that appeared in the fluorescence spectrum.

5.6 Acknowledgements

We acknowledge the financial supported by NSF CAREER Grant (CHE 1554800). The electron microscopy imaging work was performed at the Biosciences Electron Microscopy Facility of the University of Connecticut.

5.7 Reference

1. M. Li, S. K. Cushing and N. Wu, *Analyst*, 2015, **140**, 386-406.
2. F. Enrichi, A. Quandt and G. C. Righini, *Renewable and Sustainable Energy Reviews*, 2018, **82**, 2433-2439.
3. H. Yu, Y. Peng, Y. Yang and Z.-Y. Li, *npj Computational Materials*, 2019, **5**, 45.
4. Y. Luo and J. Zhao, *Nano Research*, 1-8.
5. S. Rodriguez, J. Feist, M. Verschuuren, F. G. Vidal and J. G. Rivas, *Physical review letters*, 2013, **111**, 166802.
6. F. Nan, S.-J. Ding, L. Ma, Z.-Q. Cheng, Y.-T. Zhong, Y.-F. Zhang, Y.-H. Qiu, X. Li, L. Zhou and Q.-Q. Wang, *Nanoscale*, 2016, **8**, 15071-15078.
7. S. E. Harris, J. Field and A. Imamoğlu, *Physical Review Letters*, 1990, **64**, 1107.
8. G. Khitrova, H. Gibbs, M. Kira, S. W. Koch and A. Scherer, *Nature Physics*, 2006, **2**, 81.
9. S. Christopoulos, G. B. H. Von Högersthal, A. Grundy, P. Lagoudakis, A. Kavokin, J. Baumberg, G. Christmann, R. Butté, E. Feltin and J.-F. Carlin, *Physical review letters*, 2007, **98**, 126405.
10. B. Kolaric, B. Maes, K. Clays, T. Durt and Y. Caudano, *arXiv preprint arXiv:1802.06029*, 2018.
11. H. Leng, B. Szychowski, M.-C. Daniel and M. Pelton, *Nature communications*, 2018, **9**, 4012.
12. M. Wersäll, J. Cuadra, T. J. Antosiewicz, S. Balci and T. Shegai, *Nano letters*, 2016, **17**, 551-558.
13. J. A. Faucheaux, J. Fu and P. K. Jain, *The Journal of Physical Chemistry C*, 2014, **118**, 2710-2717.
14. G. Zengin, M. Wersäll, S. Nilsson, T. J. Antosiewicz, M. Käll and T. Shegai, *Physical review letters*, 2015, **114**, 157401.
15. S. Sheikholeslami, Y.-w. Jun, P. K. Jain and A. P. Alivisatos, *Nano letters*, 2010, **10**, 2655-2660.
16. Y. Wang, G. Chen, M. Yang, G. Silber, S. Xing, L. H. Tan, F. Wang, Y. Feng, X. Liu and S. Li, *Nature communications*, 2010, **1**, 87.
17. X. D. Tian, B. J. Liu, J. F. Li, Z. L. Yang, B. Ren and Z. Q. Tian, *Journal of Raman Spectroscopy*, 2013, **44**, 994-998.
18. G. Frens, *Nature*, 1973, **241**, 20-22.
19. O. Chen, J. Zhao, V. P. Chauhan, J. Cui, C. Wong, D. K. Harris, H. Wei, H.-S. Han, D. Fukumura and R. K. Jain, *Nature materials*, 2013, **12**, 445.
20. T. Chen, G. Chen, S. Xing, T. Wu and H. Chen, *Chem. Mater*, 2010, **22**, 3826-3828.
21. J. L. Montaño-Priede, J. o. P. Coelho, A. s. Guerrero-Martínez, O. Peña-Rodríguez and U. Pal, *The Journal of Physical Chemistry C*, 2017, **121**, 9543-9551.